Designing Polymeric Materials with Enhanced Thermal Transport and Tailored Thermo-Responsive Properties

by

Apoorv Shanker

A dissertation submitted in partial fulfillment
of the requirements for the degree of
Doctor of Philosophy
(Macromolecular Science and Engineering)
in The University of Michigan
2017

Doctoral Committee:
        Professor Jinsang Kim, Chair
        Professor Anne J. McNeil
        Professor Shuichi Takayama
        Associate Professor Anish Tuteja

Apoorv Shanker

apoorvsh@umich.edu

ORCID iD: 0000-0001-9914-9515

To my parents, the greatest strengths of my life

ACKNOWLEDGEMENTS

I sincerely believe that this work would not have been possible without the support and guidance of so many people. First and foremost, my heartfelt appreciation and thanks goes to my advisor, Prof. Jinsang Kim. He has been a great mentor and teacher during my PhD study. His patient approach and guidance has tremendously shaped my scientific outlook. He encouraged me to be an independent thinker and gave freedom to explore different research ideas. Besides research, he has always been available to discuss various aspects of graduate life and career opportunities. I will always be thankful for his time and willingness to listen to my concerns. I am sure his advice will always stand me in good stead. I am also thankful to my committee members, Prof. Shuichi Takayama, Prof. Anne McNeil and Prof. Anish Tuteja for their constructive feedbacks and guidance on various aspects of my doctoral research. I am honored to have had the opportunity to conduct research under the guidance of such brilliant people. I should also acknowledge Nonna and Adam for taking care of various student matters. It made life so much easy.

This dissertation owes its existence to the excellent collaborators from the laboratories of Prof. Kevin P. Pipe and Prof. Sunitha Nagrath. I am thankful to Prof. Pipe and Prof. Nagrath to provide me with the opportunity to explore various applications of

fiancée, Kirti, for making my life beautiful. I cannot thank you enough for your love and the joy you bring. Thank you for being patient with me. It would have been impossibly difficult to maintain sanity without my friends back in India, and in Ann Arbor and East Lansing over the years. Thank you for sharing many beautiful memories with me. Lastly, this dissertation would not have been possible without the support of my family. To my parents, your endless support, unconditional love and prayers gave me the strength to overcome the difficulties I have faced over the years. I can never thank you enough. To my sister, Varuni, you have always been a source of immense joy and love. Thank you for repeatedly reminding me who I am beyond my studies and research. Nothing beats that.

Everything is provided by Him. Thank you, God.

TABLE OF CONTENTS

LIST OF FIGURES

ABSTRACT

Polymers afford modular molecular designing thereby allowing development of polymeric materials with precisely tailored intrinsic properties as well as response to neighboring environment. This dissertation discusses molecular design strategies to develop amorphous polymers with enhanced thermal transport properties, and a bi-functional polymer-based nanocomposite with thermally tunable behavior.

In the first part, strategies to modulate polymer chain morphology, inter-chain interactions, and chain packing are explored to develop amorphous polymers with high thermal conductivities. The first system consists of a polymer blend of two mutually hydrogen-bonding polymers: one, a H-bond donor polymer with long flexible chains mixed with the second H-bond acceptor polymer with short and rigid chains. A high concentration of strong and homogeneously distributed H-bonds results in a locally extended morphology of the long flexible polymer and creates a percolating network of efficient thermal connections. In this system, thermal conductivity reaching up to 1.72 $Wm^{-1}K^{-1}$ was achieved for nanoscale films, which is nearly an order of magnitude higher than that of typical amorphous polymers. In the second system of a weak polyelectrolyte, controlled ionization results in electrostatically-induced extended chain morphology, more compact chain packing, and chain stiffening which together promote enhanced thermal

xx

transport. In a system with predominantly ionized (~90%) chains, thermal conductivity reached up to 1.17 $Wm^{-1}K^{-1}$ for nanoscale films, which was nearly 3.5 times higher than that in a completely unionized polyelectrolyte film (0.34 $Wm^{-1}K^{-1}$). Furthermore, thermal conductivities up to 0.62 $Wm^{-1}K^{-1}$ was achieved in micrometer-thick films. Overall, the two strategies discussed in this dissertation present a significant breakthrough in molecular engineering of polymers to realize high thermal conductivities in amorphous systems.

In the second part, a unique polymer-graphene oxide (GO) nanocomposite film-based planar microfluidic device is presented. The fabricated devices were used for sorting circulating tumor cells (CTCs) by their on-demand capture within the device and their subsequent release. The polymer provides a thermally tunable capture or release functionality and acts as the matrix to hold the functionalized GO sheets, which in turn are the scaffolds for the cell-capturing anti-EpCAM antibodies. Combining the temperature-sensitive modality of the polymer with the sensitive GO-mediated cell capture functionality yields a device that enables the study of CTCs without many of the shortcomings of the past technologies. At room temperature, the device captured more than 80% of the CTCs at flow rates of 1-3 mLh^{-1}, and released more than 90% of the captured cells on cooling below the polymer's lower critical solution temperature. Easy operationability of the devices affords their deployment for processing of clinical samples. Viable and structurally intact CTCs were successfully isolated from 10 out of the 13 metastatic breast and pancreatic cancer patient blood samples processed. The CTCs isolated from the blood samples of metastatic breast cancer patients were further analyzed by fluorescence in situ hybridization (FISH), a standard cytogenetic technique.

Successful isolation of viable CTCs from clinical samples thus highlights the utility of the fabricated device in research and clinical settings.

Chapter 1
Introduction

1.1 High Performance Functional Polymers

Polymers have found widespread use in modern times ranging from the mundane such as packaging, fabrics, containers, non-stick cookware etc. to specialty applications such as automobiles, aircrafts, artificial hip joints etc. While in many applications such as rubber tires, foam cushions and insulation and high-performance sports equipment, polymers are the main ingredients whose properties are essential to the success of the particular technology, they are also used as additives to modify the properties of the host material, examples being motor oil, automobile windshields, cosmetics etc.[1]

Polymers also play a central role in many emerging engineering technologies such as plastic electronics, optical data storage, electric cars and fuel cells.[1] Given their tunable optoelectronic properties and advantages such as light-weight, flexibility and solution processability, conjugated polymers find use in fields like organic light-emitting diodes (OLEDs)[2] and thin film transistors (OTFTs),[3] photovoltaics,[4] thermoelectrics[5] and biosensors.[6] Polymers are being increasingly investigated as biomaterials and their

properties range from the soft and delicate water-absorbing hydrogels used to make contact lenses, tough elastomers used in short- and long-term cardiovascular devices or the high-strength acrylics used in orthopedics and dentistry.[7]

Since polymers are made by linking together a large number of small molecules (monomers), their properties can be finely controlled through rational molecular design of monomers, ratio of different monomers in the polymer chain, and architecture of the polymer chain. The modularity afforded by polymers allows to rationally design and develop polymeric materials with physical, optical, electrical, chemical or mechanical properties tailored for specific applications.

1.1.1 Stimuli-responsive Polymers

Stimuli-responsive or smart polymers are the class of polymers which have the ability to respond to external physical (temperature,[8] light,[9] electrical[10] and magnetic[11] fields etc.), chemical (pH,[12] redox,[13] solvent[14]) and biological (enzyme,[15] etc.) stimuli. Furthermore, the smart polymers can also be prepared to respond to multiple stimuli. The range of responses includes changes in shape, size, color, light transmittance, conductivity, wettability etc., and the degree of response can be controlled by the intensity of applied stimulus. Analogous to their biological counterparts such as proteins and nucleic acids, smart polymers show highly non-linear response. The weak interactions between the stimulus and monomers when summed up over thousands of catenated units provides a significant driving force for the process in the whole system.[16] Applications of smart polymers include sensors, actuators, biochemomechanical systems, self-healing materials, anti-fouling surfaces, controlled drug delivery, biointerfaces etc.[16-18]

Among the multitude of stimuli, temperature is the most widely studied and applied stimulus to drive smart material systems.[17] Thermo-responsive polymers can exhibit a variety of co-existence behavior such as upper critical solution temperature (UCST), lower critical solution temperature (LCST) or both. While the UCST behavior is enthalpically driven and is intuitive, like in the case of small molecules, that the solubility can be enhanced by increasing the temperature. The existence of LCST, i.e. critical temperature below which the polymer-solvent system is miscible in all proportions and above which phase separation occurs, is unique as it is entropically driven.[19] At the LCST, the polymer starts to phase separate from solution due to the molecular transition from a coiled enthalpically favored structure to globular entropically favored one. The LCST is often observed in highly polar solvents like water and ethanol driven by H-bonding interactions between the solvent and the polymer chains. Occurrence of LCST behavior in aqueous polymer solutions coupled with the fact that the critical temperatures in many such cases are near ambient temperature makes it an exciting area of research.

Poly(N-isopropylacrylamide) (PNIPAM) is the most widely studied polymer with an LCST of 32°C close to physiological temperature which makes it very apt for many biomedical applications.[18] Apart from polyacrylamides several other classes of polymers such as poly(*N*-vinylalkylamides) and poly(oligoethyleneoxide)methacrylates also exhibit LCST phase behavior in aqueous solutions.[17,18] The common feature of these polymers is that both the hydrophilic and hydrophobic chemical moieties are present on the same polymer chain. Thus, the LCST of the polymer can be modulated by changing the molecular structure of the monomer through incorporation of more hydrophilic/hydrophobic groups,[20] and co-polymerization.[21] The general rule is that

increasing the hydrophilic moieties in the polymer chain increases the LCST and vice-versa.

1.1.2 Inter-polymer Complex

When polyacids are mixed with non-ionic polymers in solution, a phase separation can be observed resulting in the formation of what is termed as "inter-polymer complex" (IPC). IPC was first reported by Smith and co-workers in 1959 for poly(acrylic acid) and poly(ethylene oxide) in aqueous solution.[22] Smith et. al.[22] and Bailey et. al.[23] demonstrated that the interaction between these polymers is driven by H-bonding and the IPC stoichiometry approaches 1:1. H-bond is a special type of dipole-dipole interaction between two molecules resulting from the attractive force between a hydrogen atom bound to an electronegative atom such as O, N, F and another electronegative atom. The energy of a single H-bond is
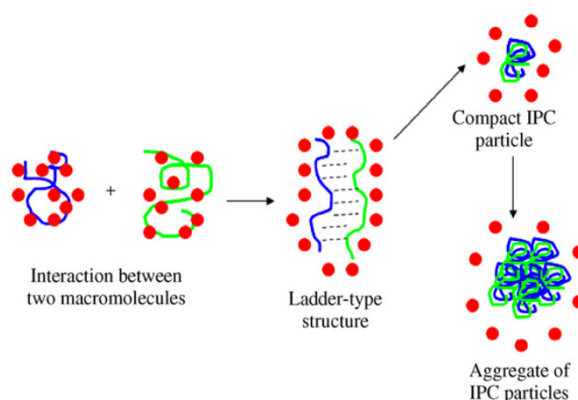
Figure 1.1| Schematic of inter-polymer complex formations. Red circles depict solvent molecules.[25] (Reprinted from Ref. 25, Copyright 2007, with permission from Elsevier.)

comparatively low (2-167 kJ/mole) and bond length is in the range 1.2-3 Å.[24] However, in the case when simultaneous co-operative H- bonding between H-bond donor and acceptor moieties on two macromolecules occurs, the strength of the bonding is substantial. In case of polymers, co-operative H-bonding results in ladder-like structure of IPC. In most cases, aggregation induced precipitation occurs (Figure 1.1).

The most commonly used polyacids for preparing IPC are poly(acrylic acid) (PAA) and poly(methacrylic acid) (PMAA). These polymers form IPC with a various classes of non-ionic polymers such as polyacrylamides, poly alcohols, polysaccharides and polymers with lactam groups and ether groups in backbone.[26] Since H-bonding occurs between the proton accepting groups of the non-ionic polymers and carboxylic hydrogen of the polyacids, the formation of IPC is dependent on the degree of ionization of the polyacids and, hence, the pH of the medium. IPC is formed in weakly or strongly acidic medium and starts disassociating as the pH of the medium is increased. In fact, the stability of IPC can be gauged from its critical pH (pH_{crit}), i.e. the pH at which the IPC starts disassociating.[27] Higher the value for pH_{crit}, more stable is the IPC formed. pH_{crit} is a specific value for a given polymer-polymer system and depends on the nature of the polymers, molecular weight, concentration and presence of small molecules or ions in the solution.[28-31]

In addition to H-bonding, formation of IPC in aqueous solutions is also stabilized by hydrophobic interactions which force the particles to coil up into globules to minimize the polymer-solvent interface.[32] As such, the stability of IPC is affected by the hydrophobic/hydrophilic nature of the polymer. For example, PMAA which is more hydrophobic than PAA forms stronger complexes with higher pH_{crit}. Staikos and co-workers demonstrated that polymers with LCST form more stable IPC due to more effective stabilization via hydrophobic interactions.[33] The stability of IPC involving a LCST polymer is also influenced by temperature as there exists a fine balance between H-bonding which is weakened at higher temperatures and hydrophobic effect which gets

stronger with increase in temperature.[34] Thus, temperature and solution pH can effectively be used to modulate the stability of IPC.

Many technical applications of H-bond stabilized IPC have been suggested. These include ion conducting materials, metal chelating materials, emulsifiers and polymeric membranes.[35] H-bonded layer-by-layer (LbL) assembly has been investigated for pH and temperature-responsive drug delivery systems, materials with tunable mechanical properties, release films dissolvable at physiological conditions, humidity sensors and for controlling protein and cellular adhesion.[25]

1.2 Polymers in Thermal Management Applications

Effective thermal management is critically important for any application because the conversion of the primary forms of energy such as electrical, mechanical, and electromagnetic energy etc. into useful work necessarily results in generation of waste heat. For example, the wall-plug efficiency of high-power light emitting diodes (LEDs) lies in the range of 5-40% implying that 60-95% of the input electrical energy is dissipated as heat.[36] The waste heat generated through power dissipation during
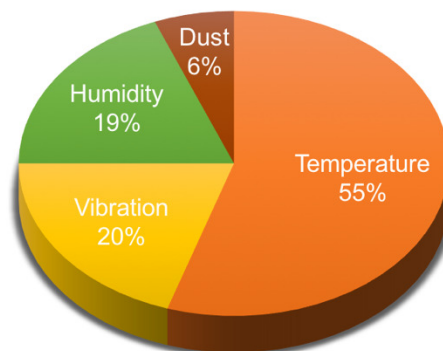
Figure 1.2 | Causes of failure in electronic devices[37]

device operation often leads to overheating in critical components resulting in performance degradation and catastrophic failure over time. In fact, this heat build-up is the primary cause of premature failure of electronic components (Figure 1.2),[37] and has prompted design and development of several thermal management techniques. While

mechanically-assisted active cooling techniques like air/liquid jet impingement, forced liquid convection, spray cooling, thermo-electric coolers, and refrigeration systems etc. are most commonly used for thermal management in large-scale units like power generators, automobile and aerospace technologies, telecommunication, server and data centers etc., small or portable consumer electronics like laptops generally rely on passive cooling via convective (either natural or forced) heat transfer from heat sinks and pipes, fins etc.[37] Although the heat flux for such portable devices is much lower than that in high power density applications, these are usually housed in sealed enclosures with constrained space which adds further complexity to devising effective thermal management solutions.

The ever increasing power densities of electronic, photonic, optoelectronic, and energy storage devices coupled with the current focus on miniaturization requires comprehensive efforts on materials, processes and design methodologies to develop effective thermal management solutions. Here, we focus on the materials aspect of thermal management, particularly on the applicability of polymeric materials in such applications.

1.2.1 Importance of Thermal Conductivity in Polymers

Compared to high thermal conductivities in metals (15-400 $Wm^{-1}K^{-1}$) and ceramics (1-40 $Wm^{-1}K^{-1}$), bulk polymers have low thermal conductivities in the range of 0.1-0.4 $Wm^{-1}K^{-1}$ which renders them inadequate for thermal management applications. While metals and ceramics are the preferred materials for thermal management, their high price, high density, and limited machinability motivate the continued study of alternative materials

with good thermal performance. In fact, despite their poor κ, polymers are the material of choice in applications such as electronic encapsulants, cellphone casings, LED housings etc. due to their low cost and easy machinability. Similarly, elastomers such as epoxies and silicones find use as thermal interface materials to link Si die with the heat sink or as underfill materials in interstitial spaces between the solder bumps in 3D-stacked Si dies to prevent air gap.[38,39]

Polymer-matrix composites (PMCs)[40] present one class of materials that is increasingly becoming a viable alternative to metals and ceramics. In convection-limited cooling, metals usually present an over-engineered solution to thermal management. The fact that the same effective cooling rates can be achieved with materials with much lower thermal conductivities has given impetus to PMCs as an alternative to metals in several thermal management applications. Moreover, PMCs offer several advantages like easy manufacturability into intricate shapes and sizes, low density, excellent mechanical properties such as high flexural strength, high low-impact strength and tensile stiffness, and corrosion resistance.[41] Compared to traditional material like aluminum, lower coefficient of thermal expansion (CTE) of PMCs matches better with that of the silicon and ceramic parts it contacts thereby reducing thermomechanical stresses at the interface.[41] They further provide mold-in functionality and consolidation of parts thereby helping to avoid post-machining operations. For example, car radiators made from PMCs can be shaped fitting the contours of the bumper rather than the traditional square box shape. Applications of PMCs include motor or motor bobbin encapsulation, tubing of heat exchangers used in industrial equipment in corrosive environment, custom-molded heat sink on circuit boards, thermistor housing, diesel fuel pumps etc.[41] They are also used in

the forms of heat spreaders like thermal pads and thermal interface materials like thermal grease or gels in electronic chips and consumer electronics such as laptops.[42]

While efforts to increase the thermal conductivity of polymeric materials generally focuses on compounding with high-κ fillers,[43] developing a method to increase thermal conductivity of pure unmixed polymers without significantly impacting their other properties (e.g., cost, weight, electrical conductivity) would enable them to displace more expensive materials in many more thermal management applications and further improve the functionality of existing polymer products. For example, device performance and reliability can benefit from high thermal conductivities of plastic encapsulants used for LEDs, electronic chips and cellphones. Furthermore, thermal conductivity of PMCs is also impacted by that of the polymer matrix, especially at lower filler loadings as the polymer acts as thermal barrier and is the limiting factor in heat conduction. Developing high-κ polymers will, thus, help to realize high thermal conductivity in polymer composites at lower filler loading thereby preserving the positive attributes like machinability and light-weight afforded by polymers as well as reducing cost.

The rapidly rising field of flexible electronics presents yet another severe challenge for thermal management as the circuit elements are generally built on flexible polymer substrates such polyetheretherketone (PEEK), polyimide (PI), polyethylene terephthalate (PET), polydimethylsiloxane (PDMS) etc. Although such devices will likely have very low power densities, low thermal conductivity of the substrate can aggravate heat build-up. Pure polymers with better heat dissipation properties can tremendously help to achieve higher performance in such devices.[44]

In addition to thermal management applications, industrial production of plastic parts and components is also expected to benefit from the high thermal conductivities in polymers. The price of finished plastic products is much higher than the cost of raw materials due to the high cost incurred during the production process. Since most plastic products are thermally machined, the intrinsic low thermal conductivity of polymers results in increased heating and cooling times during the molding processes like injection molding and extrusion which results in increased manufacturing time and cost.[45]

1.2.2 Previous Efforts to Improve Thermal Conductivity of Polymers

Thermal transport in polymers has been a subject of intense academic as well as industrial research. Primarily, two approaches have been adopted to fabricate high thermal conductivity polymeric materials: first, blending with high-κ filler particles, and second, inducing chain orientation and crystallization.

1.2.2.1 Polymer Composites with High-κ Fillers

The most commonly used method to enhance polymers' thermal conductivity is to blend them with thermally conductive fillers such as metal[46] or ceramic[47-49] particles, and carbon-based fillers such as carbon fibers[50], graphite[51] or graphene flakes,[52] carbon nanotubes (CNTs)[53] etc. Since the thermal conductivity of such composites is dominated by thermal transport in fillers, research mostly focuses on the loading level, size, shape, orientation and distribution of fillers in the polymer matrix.[43] The choice of fillers is dictated by the application of the composites, for example, electrically non-conducting ceramic fillers such as aluminum nitride and boron nitride are used if electrical insulation is

necessary. Carbon-based fillers such as graphite and CNTs or metal particles can be used if electrical insulation is not required. Achieving high κ in composites usually requires high filler loading to create a continuous conducting or percolating network through which heat can transfer efficiently.[54] This results in unwanted properties such as loss of processability and machinability, increased weight, color and cost (CNTs: \$1000/kg, PMMA: \$2/kg). Moreover, thermal transport in composites is limited by poor filler dispersion in the polymer matrix, and interfacial thermal resistance[55] between fillers and the matrix resulting in the achieved thermal conductivity that is far lower than the weighted average of those of the fillers and the polymer matrix. For example, thermal conductivity achieved in composites with spherical metal particles above the percolation threshold is on the order of 1 $Wm^{-1}K^{-1}$ (Ref. 46). Similarly, CNTs and graphite flake fillers also yield low thermal conductivities in absence of any orientation.[56,57]

1.2.2.2 Polymer Chain Orientation and Crystallization

Since heat is transferred more efficiently along the chain (intra-chain) than in the transverse direction (inter-chain), significantly higher thermal conductivity can be achieved in the direction of chain orientations.[43] Directional orientations of crystalline or semi-crystalline polymers also result in enhanced polymer crystallization. Several techniques such as simple shearing,[58] mechanical stretching,[59] gel-spinning,[60] superdrawing,[61-63] nano-porous template wetting[64] and electro-spinning[65] have been developed to realize high thermal conductivities in polymer fibers. While the thermal conductivity ($\kappa_{parallel}$) parallel to the direction of stretching rapidly increases with draw ratio, it drops slightly in the perpendicular direction ($\kappa_{perpendicular}$).[43] Thermal conductivity in

11

oriented PE has been widely studied. $\kappa_{parallel}$ up to 42 Wm^{-1}K^{-1} has been achieved in oriented PE microfibers super-drawn from single crystal mats to a draw ratio of ~350 (ref. 63). Recently, a more advanced 2-step mechanical stretching method has been demonstrated to achieve $\kappa_{parallel}$ as high as 104 Wm^{-1}K^{-1} in PE nanofibers with diameter of 50-500 nm and an estimated overall draw ratio of 60-800 (ref. 66; Figure 1.3a). These PE nanofibers were found to have single crystal structure which supports the notion that stretching results in re-structuring of polymer chains into ordered crystals. Nanoscale size of these fibers further eliminated defects such as voids, impurities and chain entanglements which explains
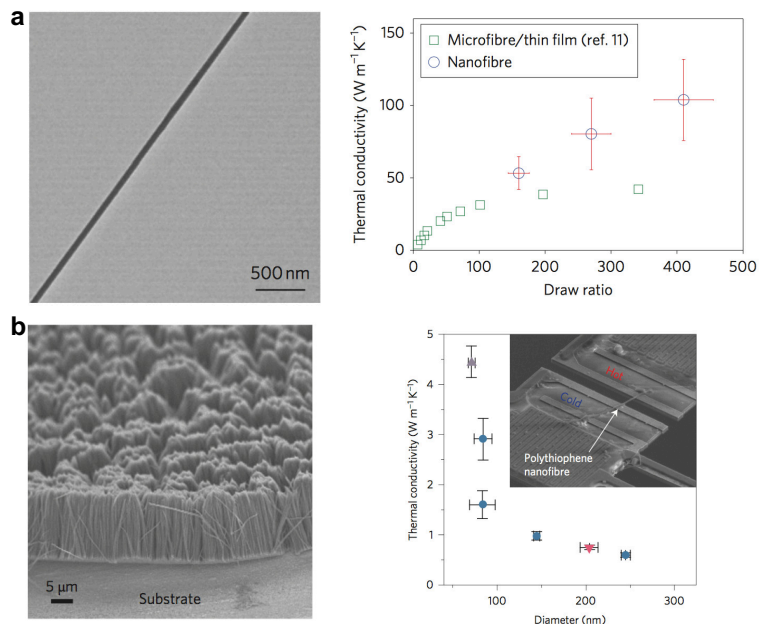
Figure 1.3 | Chain oriented polymer systems with high κ. a, SEM image of a PE nanofiber fabricated by two-step mechanical stretching method (*left*), and κ as a function of draw ratio is shown (*right*).[66] (Reprinted by permission from Macmillan Publishers Ltd: Nature Nanotechnology (Ref. 66), copyright 2010) **b,** SEM image of polythiophene nanofiber brush made by nano-template assisted electropolymerization (*left*) and κ as a function of fiber diameter (*right*).[71] (Reprinted by permission from Macmillan Publishers Ltd: Nature Nanotechnology (Ref. 71), copyright 2014)

~2.5 times higher thermal conductivity achieved compared to microfibers. Similar to crystalline/semi-crystalline polymers, stretching of amorphous polymers such as PMMA and PS also results in enhanced thermal conductivity in the direction of orientation. However, the enhancement was found to be a rather modest two-fold in most cases.[67-70]

Thermal conductivity up to 4.4 Wm^{-1}K^{-1} has been demonstrated in amorphous polythiophene nanofibers fabricated via nano-template assisted electropolymerization of thiophene monomers (Figure 1.3b).[71]

Although, chain orientation and crystallization strategies can achieve high κ in pure polymer systems, the anisotropic nature of thermal conductivity greatly limits the application of such oriented fibers. Such strategies are also difficult to be applied at large scale at a reasonable cost.

1.2.3 Models for Thermal Conductivity in Polymers

A material's ability to transfer heat energy through conduction is characterized and quantified by thermal conductivity (κ) which is related to heat flux density and temperature gradient by Fourier's law of thermal conduction:

$$\vec{q} = -\kappa \nabla T$$

where,

$\vec{q}$ is the amount of heat energy flowing through a unit area per unit time or local heat flux density (Wm^{-2}),

κ is the material's thermal conductivity (Wm^{-1}K^{-1}), and

∇T is the temperature gradient (Km^{-1}).

In all materials, thermal energy is carried essentially by atomic motions. In case of metals, the mobile electrons are the majority heat carriers and contributions from lattice vibrations can be neglected.[72] For dielectric crystals, heat is transported primarily by phonons which are energy quanta of lattice vibrations. Thermal conduction in bulk dielectric crystals is generally explained by phonon gas model (PGM)[73] which treats

phonons or vibrations as quasi-particles and their transport is modeled like gas particles which carry energy ($h\nu$ in case of phonons) and scatter off each other. PGM gives thermal conductivity as:

$$\kappa = \frac{1}{3}\, C_p \nu l$$

where,

C_p is specific heat capacity per unit volume,

ν is phonon velocity, and

l is the phonon mean free path (MFP) and is defined as product of ν and relaxation time (τ).

Although PGM is widely invoked to explain thermal conductivity in all solids, its validity becomes questionable in case of disordered solids, including amorphous polymers. Critical to applicability of PGM is a well-defined phonon velocity which determines the speed at which energy transfers through the material following the temperature gradient. Since defining phonon velocity requires the phonon wave vector to be defined which in turn needs periodicity, phonon velocity cannot be unambiguously defined for amorphous materials which lack long-range order.[73] Nevertheless, PGM can be invoked to gain physical insights as to why amorphous polymers generally have low thermal conductivities. Thermal conductivity of solids spans 5 orders of magnitude (0.1-1000 Wm^{-1}K^{-1}). For all materials, specific heat capacity essentially reaches the same value of $3k_B$ per atom, and phonon velocities are proportional to sound of speed which lies in the range of 1-10 kms^{-1}. This leaves phonon MFP to be the dominant factor which can explain the observed range of thermal conductivities. The relaxation time (and hence, MFP) of phonons in materials can span more than 3 orders of magnitude. The disordered

structure of polymers limits effective length scales over which thermal energy can propagate in amorphous polymers.[73] Consequently, due to infinitesimally short phonon MFP on the order few monomer lengths (typically <10 nm) amorphous polymer have low thermal conductivities within a narrow range of 0.1-0.4 $Wm^{-1}K^{-1}$ (ref. 43).

Building on the model of minimum thermal conductivity originally proposed by Einstein which assumes thermal transport through harmonic coupling of atomic vibrations with varying phases, Allen and Feldman further classified vibrational modes in amorphous materials as locons, diffusons and propagons to explain their contribution to thermal transport.[74,75] Locons are localized vibrational modes and do not contribute to thermal conductivity in the harmonic approximation. Diffusons are non-propagating diffusive modes, and propagons are propagating modes analogous to phonons in crystalline solids.[76] Separate studies have demonstrated important contributions to thermal conductivity from these modes.[76-85]

Molecular dynamic (MD) simulations have demonstrated important contributions to thermal conductivity in polystyrene[77] and proteins[78,79] from anharmonic coupling between localized modes or localized and delocalized modes. However, the proposed mechanism has not been experimentally verified. The most commonly used model for disordered solids is the minimum thermal conductivity model (MTCM)[76,80,81] which is based on Einstein's model of harmonic oscillators. It assumes thermal transport through diffusion of vibrational energy on a timescale of half vibrational period and incorporates Debye density of vibrational states. In the high temperature limit, MTCM gives thermal conductivity as:

$$\kappa = \left(\frac{\pi}{48}\right)^{1/3} k_B n^{2/3} (v_l + 2v_t)$$

where,

n is atomic density

v_l is longitudinal sound velocity

v_t is transverse sound velocity

k_B is Boltzmann constant.

Although the discrepancy between MTCM predicted and measured thermal conductivities lies in the range of 20 – 40% (ref. 82), the fact that the thermal conductivities can be calculated from two experimentally measurable parameters (atomic density and speed of sound) makes it a powerful tool to study heat transport properties of disordered materials. The model has been shown to correctly predict thermal conductivities of amorphous inorganic solids,[80] disordered crystals,[81] and amorphous macromolecules.[76,82,83]

Interestingly, few studies have demonstrated existence of propagating vibrational modes in amorphous solids which is contrary to the long-held notion that disordered or amorphous solids cannot support long-range phonon-like propagating modes.[84,85] Regner et. al. measured thermal conductivity of amorphous silicon oxide (SiO_2) and amorphous silicon (a-Si) as a function of phonon MFP via broadband frequency domain thermoreflectance (BB-FDTR) which allows to modulate the thermal penetration depth (TPD) during measurement.[84] Since any phonon with MFP > TPD would propagate quasi-ballistically through the material, it would not contribute to the *measured* thermal conductivity. A constant value of κ measured for SiO_2 as a function of MFP in the range of 60-900 nm suggested that any phonon-like mode would have MFP < 60 nm. Alternatively, thermal conductivity in SiO_2 could also be diffuson dominated. In contrast

to SiO_2, a-Si showed 35±7% contribution from phonon-like modes with MFP > 100 nm. In a recent study of the size-dependent thermal conductivity of amorphous Si nanotubes and films, existence of phonon-like modes with MFP ranging from 10 nm to 10 μm was established.[85] Moreover, propagons with MFP > 1 μm were found to contribute ~30% to thermal conductivity at 300K. Bulk κ for a-Si was measured to be 5.5 $Wm^{-1}K^{-1}$ which is considerably higher than the amorphous limit of 1 $Wm^{-1}K^{-1}$ given by MTCM. These studies show that while propagating modes can exist in amorphous materials, it is highly dependent on the molecular make-up of the materials.

1.2.4 Insights into Polymer Thermal Conductivity

Due to their extremely high aspect ratios and ensuing configurational entropy gain, polymer chains assume thermodynamically favorable curvilinear shapes with easily accommodated bends and kinks resulting in a highly disordered and entangled amorphous structure.[86] Such a molecular make-up along with inherent defects and chain-ends act as scattering sites for propagating vibrational waves, leading to shortened phonon MFP. Furthermore, their inefficient chain packing causes voids (and low density) that further increase scattering and dampen heat transport. The anharmonic nature of soft bonds as well as the presence of many non-propagating vibrational degrees of freedom likewise contribute to increased scattering. Soft bonds present a particular bottleneck for inter-chain thermal transport, as weak (e.g., van der Waals (vdW)) interactions do not strongly transfer vibrational energy from one chain to another and hence lead to small inter-chain thermal conductances.[87] Together, these effects cause thermal conductivities of amorphous polymers to fall primarily within a small range of 0.1-

0.4 Wm^{-1}K^{-1} (ref. 43). This is in stark contrast to the thermal conductivity of a single PE chain in extended conformation which is computed to be as high as 350 Wm^{-1}K^{-1} for a chain length greater than 100 nm.[66] Consequently, we can identify the following three parameters that together limit efficient heat transport in polymers, namely: a) highly coiled and entangled intra-chain structure, b) intrinsic amorphous loose packing and the existence of voids, and c) inter-chain interactions that are mainly weak (e.g., vdW, dipole-dipole, etc.).

The molecular make-up of polymers can be classified at three levels: 1) chemical structure including chain backbone, side groups and chain length, 2) chain morphology and orientation, and 3) inter-chain interactions. Although the three parameters are intertwined and collectively effect thermal transport properties of polymers, they are discussed separately to provide a clearer picture of materials-property relationship.

1.2.4.1 Chemical Structure

Simulation is the most commonly used tool to study the effect of molecular composition of the polymers which includes the polymer backbone as well as the side groups on their thermal transport properties. Zhang et. al. employed large scale MD simulation to investigate the effects of backbone structure on the thermal conductivity of nanofibers. π-conjugated systems such as polyacetylene (PA), polythiophene (PT), poly(p-pheneylene) (PPP) etc. were found to have higher κ compared to polymers with aliphatic backbone (Figure 1.4).[88] This was attributed to stiffer backbone due to restricted bond rotation in such conjugated systems as the rigid backbones of π-conjugated polymers allow larger phonon group velocity as well as suppress segmental rotation

thereby minimizing phonon scattering. Liu et. al. investigated the effect of disorders related to bond-strength, mass, and orientation on the thermal conductivity of polymer single chains.[89] Mixing covalent bonds of different strengths in the polymer backbone was found to create bond-strength disorder which resulted in lower κ in polybutadiene compared to that in PE or PA. Inclusion of heteroatom in an aliphatic or aromatic chain similarly created a mass disorder which localized vibrational modes thereby impeding heat transfer by delocalized, long wavelength propagating modes. For example, thermal conductivity for poly(ethylene oxide) was measured to be only 4% of that of PE for chains longer than 600 segments. In addition to mass disorder, inclusion of oxygen in poly(p-phenylene) created misalignment of orientation of aromatic rings, i.e., orientational disorder, resulting in lower κ in poly(pheneylene ether).
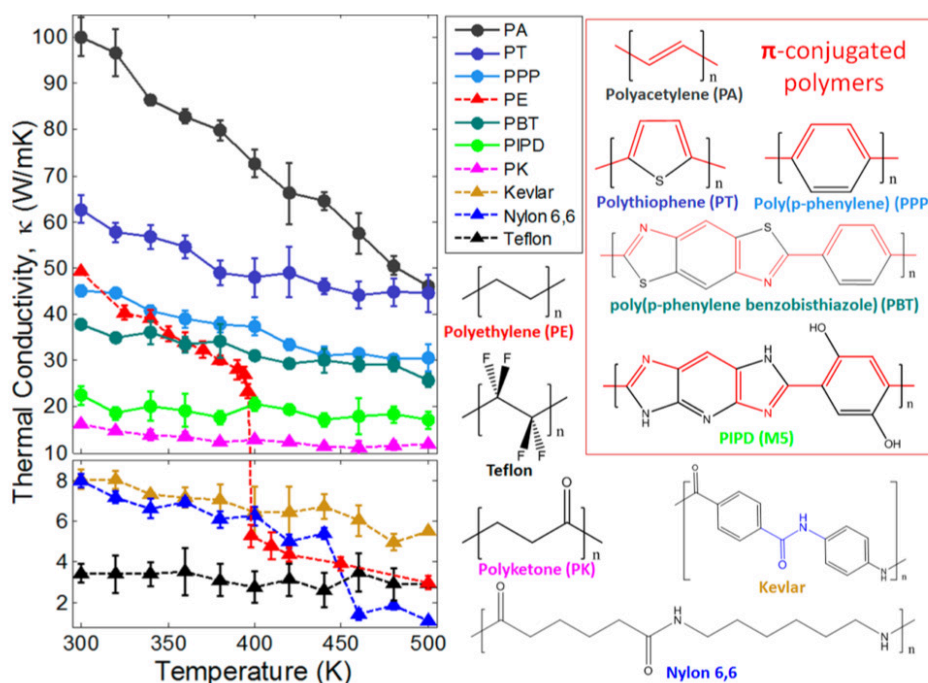
Figure 1.4 | Thermal conductivity and structure of polymer nanofibers at different temperatures. π-conjugated polymers are plotted by solid lines with circle markers, while others are plotted by dashed lines with rectangular markers.[88] (Reprinted with permission from Ref. 88. Copyright 2014 American Chemical Society.)

Liao et. al. applied equilibrium MD simulation to study the effect of chain length, molecular weight of substituent atom (Model C-X) and the ratio of substituent atoms (Model C-H_mY_n) on C-C backbone on the thermal conductivity of single-stranded carbon chain.[90] Thermal conductivities were found to be constant for polymer chains longer than 10 nm and was inversely related to the atomic mass of the substituent atoms (m_x) on the C-C backbone. Replacing a portion of H atoms with Y atoms at equal spacing also resulted in lower thermal conductivity; a mere 3% substitution of H atoms was found to lower thermal conductivity by ~75% (Figure 1.5). It is noted that the chain length dependence of thermal conductivity is in contrast to that reported by Liu et. al.[89] who showed either divergent or convergent dependence.
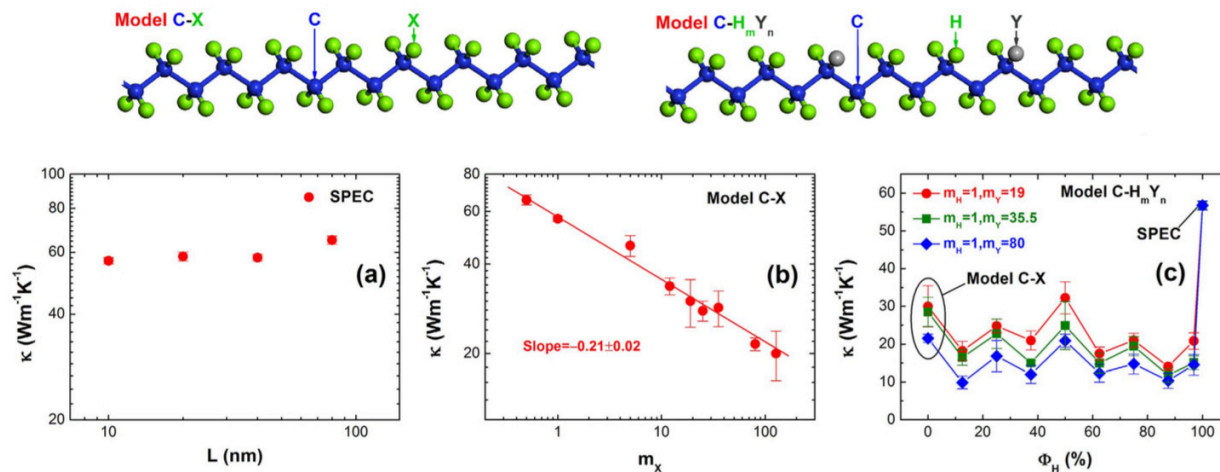
Figure 1.5 | The representative models and thermal conductivity (κ) of single-stranded carbon chain polymer with different atomic masses of X atoms (m_x) calculated by equilibrium molecular dynamics (EMD) simulations at room temperature. a, The thermal conductivity of single polyethylene chain (m_x = 1 g/mol) versus chain length (L). **b,** The thermal conductivity of Model C-X with varied m_x. **c,** The thermal conductivity of Model C-H_mY_n with variable fraction of H atoms Φ_H, where Φ_H is defined as the percentage of H atoms in the total H atoms and Y atoms.[90]

1.2.4.2 Chain Morphology and Orientation

Polymer thermal conductivity is also affected by the morphology of individual chains.[91-96] Since the dihedral angle strength and interchain interaction are the weakest interactions among different interatomic interactions in polymers, they can be easily activated and hence affect large motions of polymer chains. A lower dihedral angle strength can lead to easy segmental rotation of polymer chains inducing disorder in the chain. Such disorders result in phonon scattering thereby reducing thermal conductivity. For example, single chain PE κ was computed to increase with the dihedral angle strength; a 10-fold increase in dihedral energy resulted in more than five times
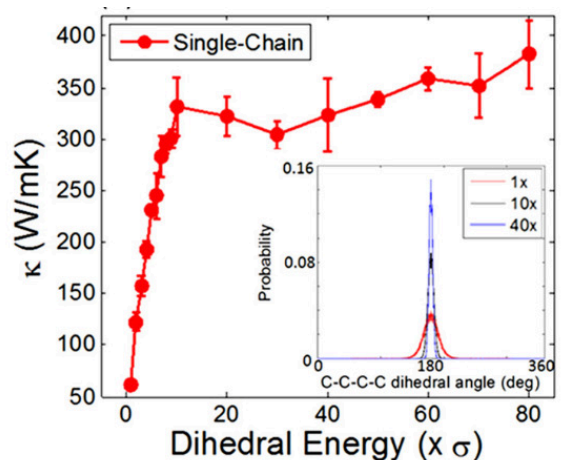
Figure 1.6| Thermal conductivity of single PE chains with different dihedral energies. Inset: probability distribution of the dihedral angle of PE backbones with 1X, 10X, and 40X dihedral energy.[92] (Reprinted from Ref. 92, with the permission of AIP Publishing.)

enhancement in thermal conductivity (Figure 1.6).[92] Compared to high κ in PE single chains[66] (~350 $Wm^{-1}K^{-1}$), poly(dimethylsiloxane) (PDMS) single chains were computed to have low κ (~7 $Wm^{-1}K^{-1}$, ref. 93) even though the phonon group velocity for PDMS (5600 ms^{-1}) was only three times smaller than that of PE (16000 ms^{-1}). Low κ in PDMS was attributed to conformational disorder scattering of phonons due to the rotational softness of Si-O-Si-O bonds resulting in pretty flat torsional potential surface of Si-O-Si-O dihedral angle.[93] Chain morphology is found to similarly affect thermal conductivity of amorphous

polymers. Large persistence length was found to enable polymer chains adopt extended conformation which allowed longer thermal transport path along the polymer backbone.[97]

Since heat is more efficiently transferred along the polymer backbone than in between the chains, thermal conductivity can be significantly higher in the direction of chain orientation. Chain orientation leads to phonon focusing which results in enhancement of group velocity as well as MFP resulting in enhanced κ.[98] Polymer chain orientation is a commonly used technique to make high κ polymer fibers as described in section 3.2. Following from above discussion, it becomes clear that ordering of polymer chains would result in higher thermal conductivity. For the same reason, crystalline polymers with their intrinsic order have higher thermal conductivities (~0.3-0.5 $Wm^{-1}K^{-1}$) than amorphous polymers (~0.1-0.2 $Wm^{-1}K^{-1}$) (ref. 43). Polypropylene (PP) which is a crystalline polymer is an interesting exception. Low κ (0.11-0.17 $Wm^{-1}K^{-}1$) in PP is generally attributed to low crystal density and possible phonon scattering by the methyl side group.[43] Thermal conductivities are also affected by the crystal form of crystalline and semi-crystalline polymers. Generally, extended crystal structure and increased lamellar thickness results in higher κ.[99]

1.2.4.3 Inter-chain Interactions

Inter-chain interactions can affect the thermal conductivity of polymers in two ways: one, by influencing chain segmental motion through confinement effects (i.e., indirectly impacting thermal transport via chain backbone) and two, coupling polymer chains to enhance inter-chain heat transfer.[100] However, the effect of inter-chain interactions is not clearly understood. MD simulation study of Nylon 6-6, Teflon, polyketone (PK) and Kevlar

nanofibers shows reduced segmental motion due to stronger inter-chain interactions like H-bonds in Nylon 6-6 and Kevlar, and strong dipole interactions in PK. Yet, it does not translate into enhanced thermal conductivity in these polymers when compared to PE. This can be attributed to presence of heteroatoms in the polymer backbone in case of Nylon 6-6 and Kevlar. Teflon, despite its strong dipole, suffers from segmental disorder and hence has low thermal conductivity.[88]

Cross-linking polymer chains using covalent chains is a compelling strategy to harness the positive contributions of stronger inter-chain interactions on thermal conductivity as it is widely used in polymer product manufacturing. However, there are serious discrepancies in literature regarding the thermal conductivities of cross-linked polymers.[101-105] While cross-linking can increase inter-chain conductance between prior weakly bonded polymer chains, it can also result in scattering of phonons along the main chain.[100] This is exemplified by the miniscule enhancement in thermal conductivities achieved in cross-linked systems such as polystyrene (PS) cross-linked with divinyl benzene (PS-DVB)[101] and polymethyl methacrylate (PMMA) cross-linked with triallylcyanurate (PMMA-TAC)[101] as well as low κ in some H-bonding polymers (e.g., Nylon 6-6).[106] On the other hand, thermal conductivity of some water soluble polymer such as poly(acrylic acid) (PAA), poly(vinyl alcohol) (PVA) and poly(4-styrene sulfonic acid) (PSS) was found to 1.5-2 times higher than that of non-water-soluble polymers.[82] H-bonding in these polymers was attributed for their higher κ. Interestingly, cross-linking in PAA through anhydride formation resulted in a drop in thermal conductivity.[83] Similarly, salts of PAA, poly(vinyl sulfonic acid) (PVSA) and poly(vinyl phosphonic acid) (PVPA) were found to have higher thermal conductivity reaching up to 0.67 $Wm^{-1}K^{-1}$ in PVPA-

Ca^{+2} salt.[82] High κ was attributed to the presence of ionic inter-chain interactions which are stronger than H-bonding and van der Waals interactions.

1.3 Functional Polymers in Cancer Diagnostics

Cancer is a group of diseases that are characterized by abnormal or uncontrolled growth and spread of cells, and over 100 different types are identified in humans. It is the second leading cause of deaths worldwide behind heart diseases.[107] Metastasis, or spread of tumor to distant parts of the
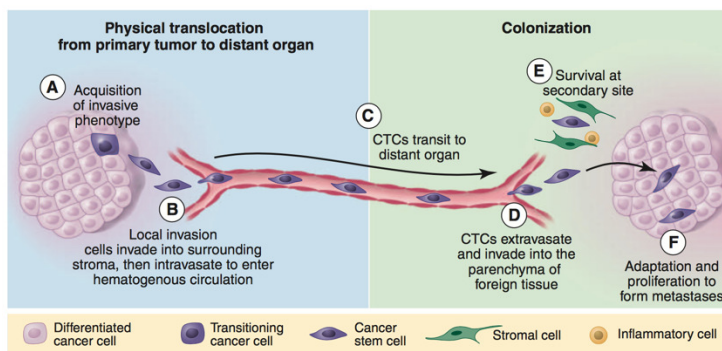
Figure 1.7 | The metastatic cascade[108] (From Ref. 108, Reprinted with permission from AAAS.)

body, is the cause for over 90% of cancer-related deaths (Figure 1.7).[108,109] Circulating tumor cells (CTCs) are those cells that are responsible for tumor metastasis. They are shed into the vasculature from the primary tumor and seed secondary tumors at distant locations.[110] CTCs were first discovered in 1869 by Thomas Ashworth who hypothesized that these cells could be the fundamental precondition to tumor metastasis.[111] Compared to biopsy, the gold standard for cancer diagnosis, CTCs provide easy and non-invasive access to tumor cells. CTCs captured through minimally invasive blood test called 'liquid biopsy', which is amenable to serial sampling, can provide information about intra-tumor heterogeneity and tumor evolution. CTCs have clinical potential as prognostic biomarkers to predict treatment efficacy, progression-free survival, and overall survival in patients.[112-116] Through minimally invasive liquid biopsy, CTCs can also provide real time information

on clonal evolution during therapy and disease progression. CTCs have been proposed as surrogate biomarkers in over 270 clinical trials.[117] However, they have not been incorporated into clinical practice for management of cancer patients. The main challenge is the very low frequency (1-10 cells per 10 mL of blood) of CTCs in blood. Moreover, CTCs are obscured by billions of blood cells which makes their isolation extraordinarily difficult.

1.3.1 Isolation Strategies for CTCs

CTC isolation techniques (Figure 1.8) share many attributes of a conventional biosensor in that they should be highly sensitive to capture the extremely low and heterogeneous population of CTCs as well as demonstrate high specificity to substantially enrich CTCs against the blood cells. It is also important the techniques are repeatable, reliable, cost-effective and rapid.[118] Moreover, they should be amenable to process automation, high-throughput to process clinically relevant volumes of blood, and compatible with downstream CTC analysis techniques.[118] These techniques should be gentle enough not to result in loss of cell viability and/or potential changes in status or phenotype due to the separation process. The CTC isolation technologies are generally evaluated in term of several parameters such as capture efficiency, recovery, CTC enrichment, purity and vitality, processing time, sample capacity and pre-treatment.[118] The optimal isolation technology may require compromise among different parameters to yield a device best suited for the intended downstream analysis techniques to be employed.[118]

Isolation techniques can be classified according to the cell attributes they exploit to separate CTCs. *Immunoaffinity-based isolation* techniques exploit the highly specific interaction between the capture antibodies and the antigens expressed on the cells to either enrich CTCs against blood cells or deplete leucocytes.[118] Introduction of immunomagnetic capture of CTCs by CellSearch system[119] through antibody-coated ferrofluid nanoparticles provided the impetus for the early investigation of CTCs. CellSearch technology with its semi-automated and standardized kits allows robust validation and reliable comparison of results,[120] and remains the only FDA-approved CTC isolation technology for metastatic breast, prostate and colorectal cancer.
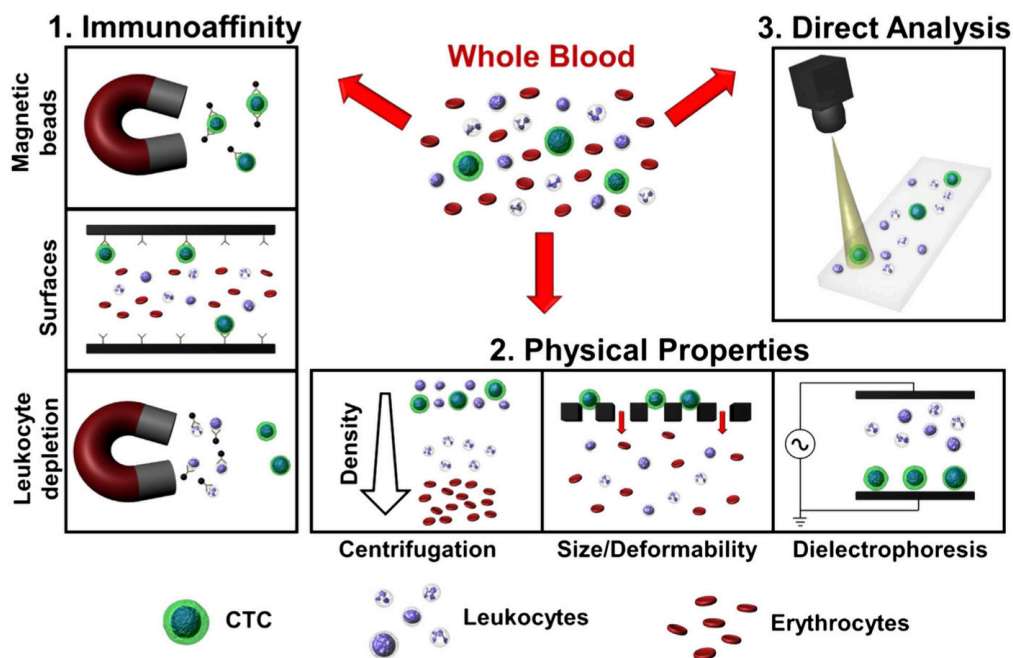
Figure 1.8 | Approaches for isolation of circulating tumor cells (CTCs) from whole blood[118] (Reprinted from Ref. 118, Copyright 2014, with permission from Elsevier.)

However, its large footprint and apparent lack of flexibility vis-à-vis further analysis of isolated cells has prompted the development of newer systems for isolation of CTCs.

Cell capture against capture antibodies tethered to solid substrates has been employed in conjunction with fluid handling systems such as microfluidic devices[121] (discussed in detail later). Other systems include nanostructured surfaces (e.g., Si nanopillars)[122] and microtubes[123] decorates with capture antibodies. A medical wire decorated with capture antibodies and which could be inserted into patient's cubital vein for 30 minutes has been used for in vivo sampling of large volumes (1.5-3 L) of blood.[124] Immunoaffinity-based CTC isolation has many advantages such as high purity of the isolated cells afforded by the high specificity of antibody-antigen interactions, and the ability to employ a cocktail of antibodies against several antigens, thereby allowing to target different subpopulations of CTCs.[125] The major drawback of antibody-based isolation is throughput. Antibody-antigen interactions are shear-dependent.[121,126] At high flow rates, high shear may result in many cells being missed. On the other hand, too low a speed may result in contamination due to non-specific cell binding.[127]

CTC isolation based on physical characteristics of CTCs exploit the differences in size, density, deformability and dielectric properties.[118] The first attempt[128] to isolate CTCs was made with microfiltration which works on the principle of retaining larger CTCs and allowing smaller leukocytes to flow through.[129] Density gradient centrifugation[130] has been used to separate CTCs from erythrocytes and granulocytes based on the difference in density. Microfluidic devices have been employed to achieve hydrodynamic separation of cells by subjecting cells based on their size and deformability to different flow forces.[131-133] Dielectrophoretic (DEP) separation employs application of non-uniform electric field to separate CTCs from normal blood cells.[134] Physical properties based separation of CTCs affords higher throughput than immunoaffinity-based techniques and is not vulnerable to

variability in antigen expression on the CTCs or loss of epithelial markers like in the case of epithelial-to-mesenchymal (EMT) transitions.[118] Centrifugation-based separation generally results in low purity. While microfiltration can process large volumes of blood, it is marred by clogging of filters[135] and loss of cell viability due to high pressure exerted during the separation process.[136] DEP separation has lower throughput and suffers with joule heating and generation of gases such as hydrogen and oxygen during operation which can result in loss of cell viability.[137]

Direct analysis of the entire population of cells in the blood is one alternative to overcome the difficulty of isolating of CTCs.[118] Towards this end, a fiber-optic array scanning technology[138] has been developed which can analyze 300,000 cells per second. A micro-Hall sensor[139] was used to enumerate CTCs by measuring the Hall voltage generated by the magnetic flux of each magnetic bead-conjugated CTC flowing through the device. While direct analysis approaches are promising as they are high throughput and less vulnerable to cell loss during operation, they are largely confined to enumeration and lack CTC enrichment necessary for the downstream analysis of these cells.[118]

1.3.2 Immunoaffinity-based Microfluidic Devices for Isolation of CTCs

Derived from micro total analysis systems (μTAS)[140], microfluidic devices for CTC isolation fall within the broader field of "lab-on-a-chip" technology. Microfluidics refers to the technology of the systems that process or manipulate small quantities (10^{-6} – 10^{-15} mL) of liquid using channels on the length scales of 10-100 μm.[141] Microfluidic devices are fabricated using techniques developed in the semiconductor industry and are generally made of silicon, glass and polymers, particularly PDMS.[142] Such devices have

small footprint for an analytical system, are low cost, use very small quantity of reagents, and allow sensitive separation and detection at rapid processing speeds.[143] Moreover, the length scale of microfluidic devices is on par with that experienced by cells in human body.

Nagrath et. al. developed the first microfluidic device for CTC isolation (Figure 1.9).[121] Named CTC Chip, the device had 78,000 100 μm tall microposts etched in silicon and covered with antibodies against epithelial cell adhesion molecule (EpCAM). The device could capture CTCs from whole blood flowing at 1 mLh^{-1} through it. However, it had low capture efficiency (~60%) and low purity (50%). Subsequent developments tried to overcome the issues of low capture and purity. Geometrically enhanced differential immunocapture (GEDI)[144] device combined the immune-affinity based capture of CTCs on microposts with hydrodynamic chromatography to reduce non-specific capture of

Figure 1.9 | Isolation of CTCs from whole blood using a microfluidic device. a, The workstation setup for CTC separation. The sample is continually mixed on a rocker, and pumped through the chip using a pneumatic-pressure-regulated pump. **b,** The CTC-chip with microposts etched in silicon. **c,** Whole blood flowing through the microfluidic device. **d,** Scanning electron microscope image of a captured NCI-H1650 lung cancer cell spiked into blood (pseudo colored red). The inset shows a high magnification view of the cell.[121] (Reprinted by permission from Macmillan Publishers Ltd: Nature (Ref. 121), copyright 2007)

leukocytes. OncoCEE (CEE, cell enrichment and extraction)[145] used microposts covered with a cocktail of antibodies to enhance capture efficiency. Since the identification and

enumeration of CTCs required immunostaining and high-resolution imaging, these devices with opaque 3D microposts posted challenges. Later developments focused on surface-capture microfluidic devices such as herringbone (HB) chip,[146] geometrically enhanced mixing (GEM) chip,[147] and the graphene oxide (GO) chip.[148] The simplified structure of these devices enabled large-scale production as well as made imaging easier. OncoBean Chip[127] with its radial flow profile enabled high throughput (10 mLh^{-1}) processing of blood samples.

The common problem with all the devices described above was that the captured CTCs could not be recovered (except for trypsin-mediated release[149]) from the devices for downstream analysis. This drawback greatly undermined the utility of these devices. This prompted development of several cell release mechanisms and their incorporation in microfluidic devices to assist post-capture recovery of CTCs. Most of these mechanisms were based on functional polymeric materials which are described in the following section.

1.3.3 Stimuli-responsive Polymers for CTC Isolation Devices

Polymeric materials that undergo changes in conformation, hydrophobicity, solubility, etc. when subjected to external stimuli such as temperature, pH, glucose concentration, voltage or current etc. have been explored as the cell release layer in the microfluidic CTC isolation devices. Enzymatic cleavage of polymeric layers has also been utilized to release captured cells from the surface of microfluidic devices. The cell release mechanisms generally employed can be categorized as:

1. Thermo-responsive release

2. Enzymatic cleavage-assisted release

3. Electro-responsive release

4. Chemically induced release

5. Light-responsive release

1.3.3.1 Thermo-responsive Release

The use of thermo-responsive polymers for cell release in microfluidic devices is inspired by the cell sheet technology wherein thermo-responsive cell culture plates are used to non-invasively obtain confluent cells as a single contiguous sheet with intact cell-cell interactions and extra cellular matrix.[150] Hou et. al. used thermo-responsive polymer brush grafted from Si nanowires for reversible capture/release of CTCs.[151] The polymer brush made via surface initiated atom transfer radical copolymerization of N-isopropyl acrylamide and 3-aminoehtyl methacrylate showed reversible switching between hydrophobic (at 37°C) and hydrophilic (at 4°C) surface. Cells were captured at 37°C and released upon cooling down to 4°C. More than 90% of the cells were successfully captured and released using the platform. Similar approach has also been employed in other devices.[152,153] Thermo-responsive approach has also been applied to deconstruct layer-by-layer assembly of biotinylated-gelatin and streptavidin.[154]

1.3.3.2 Enzymatic Cleavage-assisted Release

Trypsin, a serine protease, is commonly used to harvest cells from cell culture dishes. Aptamer cleavage has been demonstrated for release of captured CTCs.[155] Similar enzymatic cleavage approaches have been adopted with biopolymers. Shah et.

al. used a photo cross-linked alginate layer for cell capture/release.[156] Post-capture treatment with alginate lyase deconstructed the alginate platform. The released cells were found to be viable and proliferative, underlining the effectiveness of the enzyme-mediated release mechanism. Alginate lyase was also used to deconstruct a layer-by-layer assembled alginate/polyallylamine hydrochloride (PAH) platform. Up to 80% capture efficiency and 95% release efficiency with 90% viability was achieved in the optimized system.[157]

1.3.3.3 Electro-responsive Release

Electrochemical degradation of polyelectrolyte single- or multi-layer polyelectrolyte film constructed on a conductive substrate in a layer-by-layer fashion has been used for triggered release of adhered cells.[158] The same principle was employed for the detachment of adherent cells from thin films made of a water-soluble derivative of conducting polymer (CP) poly(3,4-ethylenedioxythiophene) (PEDOT). The CP film swelled and cracked into small flakes on application of potential (>0.7 V) between the film immersed in an electrolyte and a counter electrode. The detached cells, however, were required to be separated from the polymer through filtration.[159] Chen and co-workers[160] developed a 3D CP-based bioelectronic interface coupled with an electronic device for CTC isolation. Biotin-modified poly-(L)-lysine-*graft*-polyethylene glycol (PLL-g-PEG-biotin) was integrated onto 3D PEDOT nanorods. CTCs were captured on to the immobilized antibody conjugated to PLL-g-PEG-biotin which later desorbed from the PEDOT nanorods on electrical stimulation leading to release of captured cells. Jeon et. al. demonstrated a similar electrically-triggered cell release mechanism using biotin-

doped polypyrrole (PPy) substrate.[161] Application of negative potential resulted in >90% release in just 15 seconds. Reductive potential resulted in shrinkage of Ppy backbone thereby liberating the conjugated biotin and attached cells.

1.3.3.4 Chemically Induced Release

Chemically induced cell release has been achieved through modulation of pH and glucose concentration,[162] and ligand exchange.[163,164] pH and glucose dual-responsive surfaces were prepared by grafting poly(acrylamidophenylboronic acid) (polyAAPBA) from Si nanowires.[162] MCF-7 cell capture was mediated through the overexpressed sialic acid in the membrane. Competitive binding of sialic acid and glucose with polyAAPBA at different pH conditions was exploited for reversible cell capture/release. Cell capture efficiency of about 60% and release efficiency over 90% was achieved through this dual-responsive system. Deconstruction of ionically cross-linked sacrificial alginate substrate at low concentration of chelators has also been used for cell release.[163] Recently, a cell release mechanism through disruption of thiol-gold interactions in the presence of excess thiol molecules has been demonstrated.[164] Captured cells tethered to gold nanoparticles through thiol-gold interactions could be released upon addition of glutathione, a thiol-containing tripeptide. Ligand exchange between the original ligands with tethered captured cells and added glutathione resulted in cell release.

1.3.3.5 Light-responsive Release

Photothermal effect of gold nanorods (GNR) coupled with a thermoresponsive hydrogel has been utilized for near infrared (NIR) mediated cell release.[165] GNR-

embedded gelatin hydrogel substrate was imprinted with target cancer cells to create artificial receptors for improved cell capture. Post capture, NIR activation of the photo-thermal effects in GNR caused rapid increase in the temperature of the gelatin hydrogel. Rapid dissolution of gelatin at 37°C resulted in bulk release of the captured cells. Up to 92% cell capture efficiency was achieved on an antibody-coated cell-imprinted gelatin substrate. Bulk dissolution of gelatin through direct temperature modulation released 95% of the captured cells. Site-selective cell release was achieved by selective irradiation of the gelatin substrate under a selected cell; this photo-thermal release mechanism could release up to 92% of the captured cells.

1.4 Summary and Dissertation Outline

In summary, **Chapter 1** provides a general overview of functional polymers detailing their stimuli-responsive and inter-polymer complexation behaviors. Rational designing of polymers regulating their intra-chain and inter-chain interactions can be harnessed to develop polymeric materials for specific applications.

Effective thermal management is critically important for the functioning of any device. As outlined in section 1.2 of this chapter, polymeric materials, driven by the current focus on portable, lightweight and flexible devices, are increasingly assuming more important roles in thermal management applications. The intrinsic low thermal conductivities of polymers have driven the scientific community to devise and develop newer strategies to achieve enhanced thermal transport in polymeric materials. Compounding with high-κ fillers[43] and chain orientation/crystallization[66,71] are the two most prominently used methods to fabricate thermally conductive polymeric materials. However, the drawbacks associated with these two methods leave much to be desired.

In this context, developing thermally conductive amorphous polymers without requiring compounding or specialized fabrication techniques and compatible with traditional manufacturing process is important. Past works on systematic investigation of the relationship between molecular make-up of polymers and their thermal transport properties as discussed in this chapter lay the framework for the work presented in Chapters 2 and 3. Specifically, **Chapter 2** details the design strategies for developing amorphous polymer blends with high thermal conductivities. A high concentration of strong and homogeneously distributed H-bonds achieved through a rationally designed pair of H-bonding polymers is shown to result in enhanced thermal transport. Creation of an efficient percolating network of thermal connections resulted in thermal conductivities reaching up to 1.72 $Wm^{-1}K^{-1}$ in nanoscale films, which is nearly an order of magnitude higher than that of typical amorphous polymers. **Chapter 3** presents an electrostatically engineered amorphous polymer with high thermal conductivity. Extension and stiffening of polymer chains along with better packing afforded by controlled ionization of the polyelectrolyte chains results in enhanced thermal conductivity. In a predominantly ionized polymer film, thermal conductivity up to 1.17 $Wm^{-1}K^{-1}$ – nearly 3.5 times larger than in completely unionized film – was achieved.
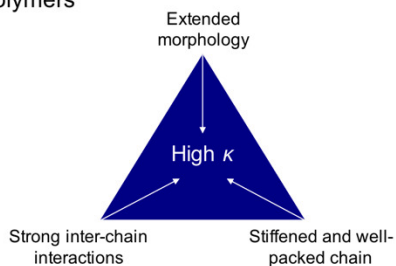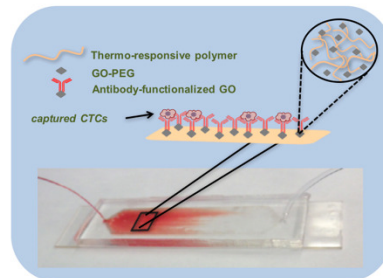
Figure 1.10 | Schematic representation of the research presented in this dissertation

Compared to tissue biopsy, the standard method for cancer diagnosis, CTCs provide easy and non-invasive access to tumor cells and have proven to be valuable biomarkers for disease diagnosis and progression. Development of a microfluidic device[121] with antibody-covered microposts for isolation of these rare cells from blood in 2007 led to paradigm shift in their study and application in clinical research. As discussed in section 1.3 of this chapter, several different strategies have been since developed. Although immunoaffinity-based isolation of CTCs is a highly selective and sensitive technique, most of the devices suffer with a common problem: the cells captured cannot be removed from the devices thus limiting the extent of different cytopathological and cytogenetic testing techniques that can be used to study these rare cells. Functional polymers with various stimuli-responsive behaviors have been used different degrees of success to release the cells captured in a microfluidic device. **Chapter 4** presents a unique polymer-graphene oxide (GO) nanocomposite film which can be applied to

microfluidic devices for isolation of CTCs. Combining the thermal tunability modality of a thermo-responsive polymer with the nanomaterial-assisted cell capturing functionality of GO provides a method of fabricating a planar microfluidic device via simple drop-casting. The fabricated devices demonstrate superior performance and were successfully used for processing clinical samples.

1.5 References

1. Heimenz, P.C., Lodge, T.P., Polymer Chemistry, CRC Press- Taylor and Francis Group, 2nd edition 2007.

2. M. Gross, D. Muller, H. Nothofer, U. Scherf, D. Neher, C. Brauchle, K. Meerholz. Improving the performance of doped pi-conjugated polymers for use in organic light-emitting diodes. *Nature* **405**, 661–665 (2000).

3. I. McCulloch, M. Heeney, C. Bailey, K. Genevicius, I. Macdonald, M. Shkunov, D. Sparrowe, S. Tierney, R. Wagner, W. Zhang, M. L. Chabinyc, R. J. Kline, M. D. McGehee, M. F. Toney. Liquid-crystalline semiconducting polymers with high charge- carrier mobility. *Nature Mater.* **5**, 328–333 (2006).

4. Y. Kim, S. Cook, S. M. Tuladhar, S. A. Choulis, J. Nelson, J. R. Durrant, D. D. C. Bradley, M. Giles, I. McCulloch, C.-S. Ha, M. Ree. A strong regioregularity effect in self-organizing conjugated polymer films and high-efficiency polythiophene: fullerene solar cells. *Nature Mater.* **5**, 197–203 (2006).

5. O. Bubnova, Z. U. Khan, A. Malti, S. Braun, M. Fahlman, M. Berggren, X. Crispin. Optimization of the thermoelectric figure of merit in the conducting polymer poly(3,4-ethylenedioxythiophene). *Nature Mater.* **10**, 429–433 (2011).

6. J. Kim, D. T. McQuade, S. K. McHugh, T. M. Swager. Ion-specific aggregation in conjugated polymers: highly sensitive and selective fluorescent ion chemosensors. *Angew. Chemie* **112**, 4026–4030 (2000).

7. http://www.britannica.com/EBchecked/topic/369081/materials- science /32300/ Materials- for-medicine (Accessed: 7th April 2017)

8. N. Zhang, S. Salzinger and B. Rieger. Poly(vinylphosphonate)s with widely tunable LCST: a promising alternative to conventional thermoresponsive polymers. *Macromol.* **45**, 9751–9758 (2012).

9. Y. Qiu and K. Park. Environment-sensitive hydrogels for drug delivery. *Adv. Drug Delivery Rev.* **53**, 321-339 (2001).

10. P. M. Mendes. Stimuli-responsive surfaces for bio-applications. *Chem. Soc. Rev.* **37**, 2512–2529 (2008).

11. X. Yu, S. Zhou, X. Zheng, T. Guo, Y. Xiao and B. Song. A biodegradable shape-memory nanocomposite with excellent magnetism sensitivity. *Nanotech.* **20**:235702 (2009).

12. R. Liu, P. Liao, J. Liu and P. Feng. Responsive polymer-coated mesoporous silica as a pH-sensitive nanocarrier for controlled release. *Langmuir* **27**, 3095-3099 (2011).

13. M. Mazurowski, M. Gallei, J. Li, H. Didzoleit, B. Stuhn and M. Rehahn. Redox-responsive polymer brushes grafted from polystyrene nanoparticles by means of surface initiated atom transfer radical polymerization. *Macromol.* **45**, 8970-8981 (2012).

14. J. K. Chen, C. Y. Hsieh, C. F. Huang, P. M. Li, S. W. Kuo and F. C. Chang. Using solvent immersion to fabricate variably patterned poly(methyl methacrylate) brushes on silicon surfaces. *Macromol.* **41**, 8729-8736 (2008).

15. O. Chambin, G. Dupuis, D. Champion, A. Voilley and Y. Pourcelot. Colon-specific drug delivery: Influence of solution reticulation properties upon pectin beads performance. *Int. J. Pharm.* **321**, 86-93 (2006).

16. I.Y. Galaev, B. Mattiasson. Smart polymers and what they could do in biotechnology and medicine. *Tibtech.* **17**, 335-340 (1999).

17. V.A. Ganesh, A. Baji, S. Ramakrishna. Smart functional polymers – a new route towards creating a sustainable environment. *RSC Adv.* **4**, 53352-53364 (2014).

18. M. Wei, Y. Gao, X. Li, M.J. Serpe. Stimuli-responsive polymers and their applications. *Polym. Chem.* **8**, 127-143 (2017).

19. L.D. Taylor, L.D. Cerankowski. Preparation of films exhibiting a balanced temperature dependence to permeation by aqueous solution- a study of lower consolute behavior. *J. Polym. Sci.* **3**, 2251-2270 (1975).

20. J.-F. Lutz. Polymerization of oligo(ethylene glycol) (meth)acrylates: toward new generations of smart biocompatible materials. *J. Polym. Sci. Part A* **46**, 3459-3470 (2008).

21. M.A. Ward, T.K. Georgiu. Thermoresponsive polymers for biomedical applications. *Polymers* **3**, 1215-1242 (2011).

22. K.L. Smith, A.E. Winslow, D.E. Petersen. Association reactions for poly(alkylene oxides) and polymeric poly(carboxylic acids), *Ind. Eng. Chem.* **51**, 1361-1364 (1959).

23. F.E. Bailey, R.D. Lundberg, R.W. Callard. Some factors affecting molecular association of poly(ethylene oxide) + poly(acrylic acid) in aqueous solution. *J. Polym. Sci. Part A* **2**, 845–851 (1964).

24. G.R. Desiraju. Hydrogen bonding. In: Encyclopedia of supramolecular chemistry 2004, Marcel Dekker Inc., 658–665.

25. V.V. Khutoryanskiy. Hydrogen-bonded interpolymer complex as materials for pharmaceutical applications. *Inter. J. Pharma.* **334**,15-26 (2007).

26. Z.S. Nurkeeva, G.A. Mun, V.V. Khutoryanskiy. Interpolymer complexes of water-soluble nonionic polysaccharides with polycarboxylic acids and their applications. *Macromol. Biosci.* **3**, 283–295 (2003).

27. T. Ikawa, K. Abe, K., Honda, E. Tsuchida. Interpolymer complex between poly(ethylene oxide) and poly(carboxylic acid). *J. Polym. Sci. Part A: Polym. Chem.* **13**, 1505–1514 (1975).

28. G.A. Mun, Z.S. Nurkeeva, V.V. Khutoryanskiy, A.B. Bitekenova. Effect of copolymer cmposition on interpolymer complex formation of (co)poly(vinyl ether)s with poly(acrylic acid) in aqueous and organic solutions. *Macromol. Rapid Commun.* **21**, 381–384 (2000).

29. G.A. Mun, Z.S. Nurkeeva, V.V. Khutoryanskiy, V.A. Kan, A.D. Sergaziev, E.M. Shaikhutdinov. Effect of hydrophobic interactions on complexing behavior of vinyl ether copolymers. *Polym. Sci. B* **43**, 289–293 (2001).

30. G.A. Mun, Z.S. Nurkeeva, V.V. Khutoryanskiy, A.D. Sergaziev. Interpolymer complexes of copolymers of vinyl ether of diethylene glycol with poly(acrylic acid). *Colloid Polym. Sci.* **280**, 282–289 (2001).

31. G.A. Mun, Z.S. Nurkeeva, V.V. Khutoryanskiy, G.S. Sarybayeva, A.V. Dubolazov. pH effects in the complex formation of polymers. part i. interaction of poly(acrylic acid) with poly(acrylamide). *Eur. Polym. J.* **39**, 1687–1691 (2003).

32. A.S. Michaels, R. Miekke. Polycation-polyanion complexes: preparation and properties of poly-(vinylbenzyltrimethylammonium) poly-(styrenesulfonate). *J. Phys. Chem.* **65**, 1765-1773 (1965).

33. M. Kousathana, P. Lianos, G. Staikos. Investigation of hydrophobic interactions in dilute aqueous solutions of hydrogen-bonding interpolymer complexes by steady-state and time-resolved fluorescence measurements, *Macromol.* **30**, 7798-7802 (1997).

34. V.V. Khutoryanskiy, Z.S. Nurkeeva, G.A. Mun, A.V. Dubolazov. Effect of temperature on aggregation/dissociation behavior of interpolymer complexes stabilized by hydrogen bonds. *J. Appl. Polym. Sci.* **93**, 1946–1950 (2004).

35. V.V. Khutoryanskiy. Hydrogen-bonded interpolymer complex as materials for pharmaceutical applications. *Inter. J. Pharma.* **334**, 15-26 (2007).

36. http://Wm^{-1}K^{-1}.ledsmagazine.com/articles/2005/05/fact-or-fiction-leds-don-t-produce-heat.html (Retrieved: 7th April 2017)

37. S.S. Anandan, V. Ramalingam. Thermal management of electronics: A review of Literature. *Thermal Science* **12**, 5-26 (2008), DOI: 10.2298/TSCI0802005A.

38. W.S. Lee, J. Yu. Comparative study of thermally conductive fillers in underfill for the electronic components. *Diam. Relat. Mater.* **14**, 1647-1653 (2005).

39. Q. Liang, Y. Xiu, W. Lin, K.S. Moon, C.P. Wong. Epoxy/h-BN composites for thermally conductive underfill material. Electronic Components and Technology, IEEE, San Diego, CA, 2009

40. M.A. Vadivelu, C.R. Kumar, G.M. Joshi. Polymer composites for thermal management: a review. *Compos. Interface* **23**, 847-872 (2016).

41. http://www.ptonline.com/articles/plastics-that-conduct-heat (Accessed: 7th April 2017)

42. R. Prasher. Thermal interface materials: historical perspective, status, and future directions. *Proc. IEEE* **94**, 1571-1586 (2006)

43. H. Chen, V.V. Ginzburg, J. Yang, Y. Yang, W. Liu, Y. Huang, L. Du, B. Chen. Thermal conductivity of polymer-based composites: fundamentals and applications. *Prog. Polym. Sci.* **59**, 41-85 (2016).

44. A.L. Moore, L. Shi. Emerging challenges and materials for thermal management of electronics. *Mater. Today* **17**, 163-174 (2014).

45. C. Nylund, K. Meinander. The influence of heat transfer coefficient on cooling time in injection molding. *Heat Mass Transfer* **4**, 428-431 (2005).

46. Y.P. Mamunya, V.V. Davydenko, P. Pissis, E. Lebedev. Electrical and thermal conductivity of polymers filled with metal powders. *Eur. Polym. J.* **38**, 1887–1897 (2002).

47. T. Zhou, X. Wang, G.U. Mingyuan, X. Liu. Study of the thermal conduction mechanism of nano-SiC/DGEBA/EMI-2,4 composites. *Polymer* **49**, 4666–4672 (2008).

48. R.F. Hill, P.H. Supancic. Determination of the Thermal Resistance of the Polymer-Ceramic Interface of Alumina-Filled Polymer Composites. *J. Am. Ceram. Soc.* **87**, 1831–1835 (2004).

49. S.Z. Yu, P. Hing, X. Hu. Thermal conductivity of polystyrene-aluminum nitride composite. *Composites A* **33**, 289-292 (2002).

50. M. Wang, Q.J. Kang, N. Pan. Thermal conductivity enhancement of carbon fiber composites. *Appl. Therm. Eng.* **29**, 418-121 (2009).

51. I. Krupa, I. Novak, I. Chodak. Electrically and thermally conductive polyethylene/graphite composites and their mechanical properties. *Synth. Met.* **145**, 245-52 (2004).

52. L. Zhang, J.T. Wu, L. Jiang. Graphene and its polymer nanocomposites. *Prog. Chem.* **26**, 560-571 (2014).

53. Z.D. Han, A. Fina. Thermal conductivity of carbon nanotubes and their polymer nanocomposites: a review. *Prog. Polym. Sci.* **36**, 914-944 (2011).

54. A. Yu, P. Ramesh, X. Sun, E. Bekyarova, M.E. Itkis, R.C. Haddon. Enhanced thermal conductivity in a hybrid graphite nanoplatelet- carbon nanotube filler for epoxy composites. *Adv. Mater.* **20**, 4740-4744 (2008).

55. P.J. O'Brien, S. Shenogin, J. Liu, P.K. Chow, D. Laurencin, P.H. Mutin, M. Yamaguchi, P. Keblinski & G. Ramanath. Bonding-induced thermal conductance enhancement at inorganic hetero-interfaces using nanomolecular monolayers. *Nature Mater.* **12**, 118-122 (2013).

56. M. Moniruzzaman, K.I. Winey. Polymer nanocomposites containing carbon nanotubes. *Macromol.* **39**, 5194- 5205 (2006).

57. J.R. Potts, D.R. Dreyer, C.W. Bielawski, R.S. Ruoff. Graphene-based polymer nanocomposites. *Polymer* **52**, 5-25 (2011).

58. D. Hansen, G.A. Bernier. Thermal-conductivity of polyethylene – The effects of crystal size, density and orientation on thermal conductivity. *Polym. Eng. Sci.* **12**, 204-208 (1972).

59. C.L. Choy, W.H. Luk, F.C. Chen. Thermal-conductivity of highly oriented polyethylene. *Polymer* **19**,155-162 (1978).

60. K. Anandakumaran, S.K. Roy, R.S. Manley. Drawing-induced changes in the properties of polyethylene fibers prepared by gelation crystallization. *Macromol.* **21**,1746-1751 (1988).

61. Choy CL, Leung WP. Thermal-conductivity of ultradrawn polyethylene. *J. Polym. Sci. Polym. Phys. Ed.* **21**,1243–1246 (1983).

62. T. Kanamoto, A. Tsuruta, K. Tanaka, M. Takeda, R.S. Porter. Superdrawing of ultrahigh molecular weight polyethylene. I: Effect of techniques on drawing of single crystals mats. *Macromol.* **21**, 470–477 (1988).

63. C.L. Choy, Y.W. Wong, G.W. Yang, T. Kanamoto. Elastic modulus and thermal conductivity of ultradrawn polyethylene. *J. Polym. Sci. B Polym. Phys.* **37**, 3359–3367 (1999).

64. B.Y. Cao, Y.W. Li, J. Kong, H. Chen, Y. Xu, K.L. Yung, A. Cai. High thermal conductivity of polyethylene nanowire arrays fabricated by an improved nanoporous template wetting technique. *Polymer* **52**, 1711–1715 (2011).

65. Z.X. Zhong, M.C. Wingert, J. Strzalka, H.H. Wang, T. Sun, J. Wang, R.K. Chen, Z. Jiang. Structure-induced enhancement of thermal conductivities in electrospun polymer nanofibers. *Nanoscale* **6**, 8283–8291 (2014).

66. S. Shen, A. Henry, J. Tong, R.T. Zheng, G. Chen. Polyethylene nanofibres with very high thermal conductivities. *Nature Nanotech.* **5**, 251-255 (2010).

67. E.A. Algaer, M. Alaghemandi, M.C. Bohm, F. Muller-Plathe. Anisotropy of the thermal conductivity of stretched amorphous polystyrene in supercritical carbon dioxide studied by reverse non-equilibrium molecular dynamics simulations. *J. Phys. Chem. B* **113**, 14596–14603 (2009).

68. C.L. Choy. Thermal-conductivity of polymers. *Polymer* **18**, 984–1004 (1977).

69. K. Eiermann, K.H. Hellwege. Thermal conductivity of high polymers from −180°C to 90°C. *J. Polym. Sci.* **57**, 99–106 (1962).

70. J. Hennig. Anisotropy and structure in uniaxially stretched amorphous high polymers. *J. Polym. Sci. C Polym. Symp.* **16**, 2751–2758 (1967).

71. V. Singh, T.L. Bougher, A. Weathers, Y. Cai, K.D. Bi, M.T. Pettes, S.A. McMe-namin, W. Lv, D.P. Resler, T.R. Gattuso, D.H. Altman, K.H. Sandhage, L. Shi, A. Henry, B.A. Cola. High thermal conductivity of chain-oriented amorphous polythiophene. *Nature Nanotech.* **9**, 384–390 (2014).

72. C.C. Bidwell. Thermal conductivity of metals. *Phys. Rev.* **58**, 561-564 (1940).

73. W. Lv, A. Henry. Examining the Validity of the Phonon Gas Model in Amorphous *Materials. Sci. Rep.* **6**:37675 (2016).

74. P.B. Allen and J. L. Feldman. Thermal conductivity of disordered harmonic solids. *Phys. Rev. B* **48**, 12581 (1993).

75. P.B. Allen, J.L. Feldman, J. Fabian, F. Wooten. Diffusons, locons and propagons: Character of atomic vibrations in amorphous Si*. Philos. Mag. B* **79**, 1715-1731 (1999).

76. W.P. Hsieh, M. Losego, P.V. Braun, S. Shenogin, P. Keblinski, D.G. Cahill. Testing the minimum thermal conductivity model for amorphous polymers using high pressure. *Phys. Rev. B* **83**, 1-5 (2011).

77. S. Shenogin, A. Bodapati, P. Keblinski, A.J.H. McGaughey. Predicting the thermal conductivity of inorganic and polymeric glasses: The role of anharmonicity. *J. Appl. Phys.* **105**, 1-6 (2009).

78. D. M. Leitner. Energy Flow in Proteins. *Annu. Rev. Phys. Chem.* **59**, 233-259 (2008).

79. X. Yu and D.M. Leitner. Heat flow in proteins: computation of thermal transport coefficients. *J. Chem. Phys.* **123**, 059903 (2005).

80. D.G. Cahill, R.O. Pohl. Heat flow and lattice vibrations in glasses. *Solid State Commun.* **70**, 927-930 (1989).

81. D.G. Cahill, S.K. Watson, R.O. Pohl. Lower limit to the thermal conductivity of disordered solids. *Phys. Rev. B* **46**, 6131-6140 (1992).

82. X. Xie, K. Yang, D. Li, T.H. Tsai, J. Shin, P.V. Braun, D.G. Cahill. High and low thermal conductivity of amorphous macromolecules. *Phys. Rev. B* **95**, 035406 (2017).

83. X. Xie, D. Li, T.H. Tsai, J. Liu, P.V. Braun, D.G. Cahill. Thermal conductivity, heat capacity, and elastic constants of water-soluble polymers and polymer blends. *Macromol.* **49**, 972-978 (2016).

84. K.T. Regner, D.P. Sellan, Z. Su, C.H. Amon, A.J.H. McGaughey, J.A. Malen. Broadband phonon mean free path contributions to thermal conductivity measured using frequency domain thermoreflectance. *Nature Commun.* **4**, 1640 (2013).

85. S. Kwon, J. Zheng, M.C. Wingert, S. Cui, R. Chen. Unusually high and anisotropic thermal conductivity in amorphous silicon nanostructures. *ACS Nano* **11**, 2470-2476 (2017).

86. Henry, A. Thermal transport in polymers In: Annual review of heat transfer. Volume 17, Begell House, (2014).

87. W. Zhong. Different thermal conductance of the inter- and intrachain interactions in a double-stranded molecular structure. *Phys. Rev. E* **81**, 1–5 (2010).

88. T. Zhang, X.F. Wu, T.F. Luo. Polymer nanofibers with outstanding thermal conductivity and thermal stability: fundamental linkage between molecular characteristics and macroscopic thermal properties. *J. Phys. Chem. C* **118**, 21148–59 (2014).

89. J. Liu, R. Yang. Length-dependent thermal conductivity of single extended polymer chains. *Phys. Rev. B* **86**,104307 (2012).

90. L. Quanwen, Z. Lingping, L. Zhichun, L Wei. Tailoring thermal conductivity of single-stranded carbon-chain polymers through atomic mass modification. *Sci. Rep.* **6**:34999 (2016).

91. T. Zhang, T. Luo. High-contrast, reversible thermal conductivity regulation utilizing the phase transition of polyethylene nanofibers. *ACS Nano* **7**, 7592−7600 (2013).

92. T. Zhang, T. Luo. Morphology-influenced thermal conductivity of polyethylene single chains and crystalline fibers. *J. Appl. Phys.* **112**, 094304 (2012).

93. T. Luo, K. Esfarjani, J. Shiomi, A. Henry, G. Chen. Molecular dynamics simulation of thermal energy transport in polydimethylsiloxane. *J. Appl. Phys.***109**, 074321 (2011).

94. Z. Guo, D. Lee, Y. Liu, F. Sun, A. Sliwinski, H. Gao, P.C. Burns, L. Huang, T. Luo. Tuning the thermal conductivity of solar cell polymers through side chain engineering. *Phys. Chem. Chem. Phys.* **16**, 7764−7771 (2014).

95. E.A. Algaer, M. Alaghemandi, M.C. Böhm, F. Müller-Plathe. Anisotropy of the thermal conductivity of stretched amorphous polystyrene in supercritical carbon dioxide studied by reverse non-equilibrium molecular dynamics simulations. *J. Phys. Chem. B* **113**, 14596−14603 (2009).

96. M. Alaghemandi, M. Gharib-Zahedi, E. Spohr, M.C. Böhm. Thermal conductivity of polyamide-6,6 in the vicinity of charged and uncharged graphene layers: a molecular dynamics analysis. *J. Phys. Chem. C* **116**, 14115−14122 (2012).

97. T. Zhang, T. Luo. Role of chain morphology and stiffness in thermal conductivity of amorphous polymers. *J. Phys. Chem. B* **120**, 803-812 (2016).

98. T. Mugishima, Y. Kogure, Y. Hiki, K. Kawasaki, H. Nakamura. Phonon conduction in polyethylene. *J. Phys. Soc. Jpn.* **57**, 2069-2079 (1988).

99. J.C. Yu, B. Sundqvist, B. Tonpheng, O. Andersson. Thermal conductivity of highly crystallized polyethylene. *Polymer* **55**,195-200 (2014).

100. B. Ni, T. Watanabe, S. R. Phillpot. Thermal transport in polyethylene and at polyethylene–diamond interfaces investigated using molecular dynamics simulation. *J. Phys. Condens. Matter* **21**, 084219 (2009).

101. O. Yamamoto & H. Kambe. Thermal conductivity of cross-linked polymers. A comparison between measured and calculated thermal conductivities. *Polym. J.* **2**, 623-628 (1971).

102. G. Kikugawa, T.G. Desai, P. Keblinski, T. Ohara. Effect of crosslink formation on heat conduction in amorphous polymers. *J. Appl. Phys.* **114**, 034302 (2013).

103. B. Tonpheng, J. Yu, O. Andersson. Effects of cross-links, pressure and temperature on the thermal properties and glass transition behaviour of polybutadiene. *Phys. Chem. Chem. Phys.* **13**, 15047-15054 (2011).

104. S. Yu, C. Park, S.M. Hong, C.M. Koo. Thermal conduction behaviors of chemically cross-linked high-density polyethylenes. *Thermochimica Acta* **583**, 67-71 (2014).

105. W. Knappe, O. Yamamoto. Effects of crosslinking and chain degradation on the thermal conductivity of polymers. *Kolloid-Zeitschrift und Zeitschrift für Polymere* **240**, 775-783 (1970).

106. J.E. Mark. *Physical Properties of Polymers Handbook* (AIP Press, 1996).

107. L.A. Torre, F. Bray, R.L. Siegel, J. Ferlay, J. Lortet-Tieulent, A. Jemal. Global cancer statistics, 2012. *CA Cancer J. Clin.* **65**, 87–108 (2016).

108. C.L. Chaffer, R.A. Weinberg. A perspective on cancer cell metastasis. *Science* **331**, 1559–1564 (2011).

109. R.P. Kulkarni. Perspectives on clinical applications of CTCs. in: (Eds: R.J. Cote, R.H. Datar), Circulating tumor cells, Springer, New York, 2016, pp. 315–323.

110. M. Riquet, C. Rivera, L. Gibault, C. Pricopi, P. Mordant, A. Badia, A. Arame, F. Le Pimpec Barthes. Lymphatic spread of lung cancer: anatomical lymph node chains unchained in zones. *Rev. Pneumol. Clin.* **70**, 16–25 (2014).

111. T.R. Ashworth. A case of cancer in which cells similar to those in the tumours were seen in the blood after death. *Aust. Med. J.* **14**, 146–149 (1869).

112. M. Cristofanilli *et al.* Circulating tumor cells: A novel prognostic factor for newly diagnosed metastatic breast cancer. *J. Clin. Oncol.* **23**, 1420-1430 (2005).

113. S. Riethdorf *et al.* Detection of circulating tumor cells in peripheral blood of patients with metastatic breast cancer: a validation study of the cell search system. *Clin. Cancer Res.* **13**, 920-928 (2007).

114. H. Yagata *et al.* Evaluation of circulating tumor cells in patients with breast cancer: multi-institutional clinical trial in Japan. *Int. J. Clin. Oncol.* **13**, 252-256 (2008).

115. T. Kurihara *et al.* Detection of circulating tumor cells in patients with pancreatic cancer: a preliminary result. *J. Hepatobiliary Pancreat. Surg.* **15**, 189-195 (2008).

116. L. Khoja *et al.* A pilot study to explore circulating tumour cells in pancreatic cancer as a novel biomarker. *Br. J. Cancer* **106**, 508-516 (2011).

117. C. Alix-Panabieres & K. Pantel. Challenges in circulating tumour cell research. *Nature Rev. Cancer* **14**, 623-631 (2014).

118. R. Harouaka, Z. Kang, S.Y. Zheng, L. Cao. Circulating tumor cells: advances in isolation and analysis, and challenges for clinical applications. *Pharmacol. Ther.* **141**, 209–221 (2014).

119. https://www.cellsearchctc.com (Retrieved: 15th March 2017)

120. S. Riethdorf, H. Fritsche, V. Müller, T. Rau, C. Schindlbeck, B. Rack, W. Janni, C. Coith, K. Beck, F. Ja€nicke, S. Jackson, T. Gornet, M. Cristofanilli, K. Pantel. Detection of circulating tumor cells in peripheral blood of patients with metastatic breast cancer: a validation study of the Cell Search system. *Clin. Cancer Res.* **13**, 920-928 (2007).

121. S. Nagrath, L.V. Sequist, S. Maheswaran, D.W. Bell, D. Irimia, L. Ulkus, M.R. Smith, E.L. Kwak, S. Digumarthy, A. Muzikansky, P. Ryan, U.J. Balis, R.G. Tompkins, D.A. Haber, M. Toner. Isolation of rare circulating tumour cells in cancer patients by microchip technology. *Nature* **450**, 1235-1239 (2007).

122. S. Wang, H. Wang, J. Jiao, K.J. Chen, G.E. Owens, K. Kamei *et al*. Three-dimensional nanostructured substrates toward efficient capture of circulating tumor cells. *Angew. Chem. Int. Ed. Engl.* **48**, 8970–8973 (2009).

123. A.D. Hughes, J. Mattison, L.T. Western, J.D. Powderly, B.T. Greene, & M.R. King. Microtube device for selectin-mediated capture of viable circulating tumor cells from blood. *Clin. Chem.* **58**, 846–853 (2012).

124. N. Saucedo-Zeni, S. Mewes, R. Niestroj, L. Gasiorowski, D. Murawa, P. Nowaczyk *et al.* A novel method for the in vivo isolation of circulating tumor cells from peripheral blood of cancer patients using a functionalized and structured medical wire. *Int. J. Oncol.* **41**, 1241-1250 (2012).

125. C.V. Pecot, F.Z. Bischoff, J.A. Mayer, K.L. Wong, T. Pham, J. Bottsford-Miller, R.L. Stone, Y.G. Lin, P. Jaladurgam, J.W. Roh, B.W. Goodman, W.M. Merritt, T.J. Pircher, S.D. Mikolajczyk, A.M. Nick, J. Celestino, C. Eng, L.M. Ellis, M.T. Deavers, A.K. Sood. A novel platform for detection of CK+ and CK- CTCs. *Cancer Discovery* **1**, 580-586 (2011).

126. S. Mittal, I.Y. Wong, W.M. Deen, M. Toner. Antibody-functionalized fluid-permeable surfaces for rolling cell capture at high flow rates. *Biophys J.* **102**, 721-730 (2012).

127. V. Murlidhar, M. Zeinali, S. Grabauskiene, M. Ghannad-Rezaie, M.S. Wicha, D.M. Simeone, N. Ramnath, R.M. Reddy, S. Nagrath. A radial flow microfluidic device for ultra-high-throughput affinity-based isolation of circulating tumor cells. *Small* **10**, 4895-4904 (2014).

128. I. Salgado, J.F. Hopkirk, R.C. Long, A.C. Ritchie, S. Ritchie, D.R. Webster. Tumour cells in the blood. *Can Med. Assoc. J.* **81**, 619-622 (1959).

129. G. Vona, A. Sabile, M. Louha, V. Sitruk, S. Romana, K. Schutze *et al*. Isolation by size of epithelial tumor cells—a new method for the immune-morphological and molecular characterization of circulating tumor cells. *Am. J. Pathol.* **156**, 57–63 (2000).

130. R. Rosenberg, R. Gertler, J. Friederichs, K. Fuehrer, M. Dahm, R. Phelps *et al*. Comparison of two density gradient centrifugation systems for the enrichment of disseminated tumor cells in blood. *Cytometry* **49**, 150–158 (2002).

131. D.D. Carlo, D. Irimia, R.G. Tompkins, M. Toner. Continuous inertial focusing, ordering, and separation of particles in microchannels. *Proc. Natl. Acad. Sci. USA* **104**, 18892-18897 (2007).

132. A. Russom, A.K. Gupta, S. Nagrath, D. Di Carlo, J.F. Edd, M. Toner. Differential inertial focusing of particles in curved low-aspect-ratio microchannels. *New J. Phys.*, **11**, 75025 (2009).

133. J.A. Davis, D.W. Inglis, K.J. Morton, D.A. Lawrence, L.R. Huang, S.Y. Chou, J.C. Sturm, R.H. Austin. Deterministic hydrodynamics: taking blood apart. *Proc. Natl. Acad. Sci. USA* **103**, 14779-84 (2006).

134. F.F. Becker, X.B. Wang, Y. Huang, R. Pethig, J. Vykoukal, P.R. Gascoyne. Separation of human breast cancer cells from blood by differential dielectric affinity. *Proc. Natl. Acad. Sci. USA* **92**, 860–864 (1995).

135. D.R. Gossett, W.M. Weaver, A.J. Mach, S.C. Hur, H.T. Tse, W. Lee, H. Amini, D.D. Carlo. Label-free cell separation and sorting in microfluidic systems. *Anal. Bioanal. Chem.* **397**, 3249-3267 (2010).

136. M.D. Zhou, S. Hao, A.J. Williams, R.A. Harouaka, B. Schrand, S. Rawal, Z. Ao, R. Brennaman, E. Gilboa, B. Lu, S. Wang, J. Zhu, R. Datar, R. Cote, Y.C. Tai, S.Y. Zheng. Separable bilayer microfiltration device for viable label-free enrichment of circulating tumour cells. *Scientific Reports* **4**: 7392 (2014).

137. Z.T.F. Yu, K.M. Aw Yong, J. Fu. Microfluidic blood cell preparation: now and beyond. *Small* **10**, 1687-1703 (2014).

138. R.T. Krivacic, A. Ladanyi, D.N. Curry, H.B. Hsieh, P. Kuhn, D.E. Bergsrud *et al*. A rare-cell detector for cancer. *Proc. Natl. Acad. Sci. U.S.A.* **101**, 10501–10504 (2004).

139. D. Issadore, J. Chung, H. Shao, M. Liong, A.A. Ghazani, C.M. Castro R. Weissleder *et al*. Ultrasensitive clinical enumeration of rare cells ex-vivo using a micro-Hall detector. *Sci. Transl. Med*. **4**, 141ra192 (2012).

140. A. Manz, N. Graber, H.M. Widmer. Miniaturized total chemical analysis systems: a novel concept for chemical sensing. *Sensors Actuat. B Chem.* **1,** 244–248 (1990).

141. N.T. Nguyen, S.T. Wereley. Fundamentals and applications of microfluidics, Artech House, Boston/London, 2002.

142. J. Zhang, J. Chen, K. Fan. Circulating tumor cells isolation and analysis. in: advances in clinical chemistry (Ed: G.S. Makowski), Volume **75**, Elsevier (2016).

143. A. Manz, D.J. Harrison, E.M.J. Verpoorte, J.C. Fettinger, A. Paulus, H. Ludi, H.M. Widmer. Planar chips technology for miniaturization and integration of separation techniques into monitoring systems: Capillary electrophoresis on a chip. *J. Chromatogr. A.* **593,** 253–258 (1992).

144. J.P. Gleghorn, E.D. Pratt, D. Denning, H. Liu, N.H. Bander, S.T. Tagawa, D.M. Nanus, P.A. Giannakakou, B.J. Kirby. Capture of circulating tumor cells from whole blood of prostate cancer patients using geometrically enhanced differential immunocapture (GEDI) and a prostate-specific antibody. *Lab chip* **10**, 27–29 (2010).

145. M.N. Dickson, P. Tsinberg, Z. Tang, F.Z. Bischoff, T. Wilson. E.F. Leonard. Efficient capture of circulating tumor cells with a novel immunocytochemical microfluidic device. *Biomicrofluidics* **5**, 34119-3411915 (2011).

146. S.L. Stott, C.H. Hsu, D.I. Tsukrov, M. Yu, D.T. Miyamoto, B.A. Waltman *et al.* Isolation of circulating tumor cells using a microvortex-generating herringbone-chip. *Proc. Natl. Acad. Sci. USA* **107**, 18392–18397 (2010).

147. W. Sheng, O.O. Ogunwobi, T. Chen, J. Zhang, T.J. George, C. Liu *et al.* Capture, release and culture of circulating tumor cells from pancreatic cancer patients using an enhanced mixing chip. *Lab Chip* **14**, 89–98 (2014).

148. H.J. Yoon, T.H. Kim, Z. Zhang, E. Azizi, T.M. Pham, C. Paoletti C *et al.* Sensitive capture of circulating tumour cells by functionalized graphene oxide nanosheets. *Nature Nanotech.* **8**, 735–741 (2013).

149. A. A. Adams, P. I. Okagbare, J. Feng, M. L. Hupert, D. Patterson, J. Göttert, R. L. McCarley, D. Nikitopoulos, M. C. Murphy, S. A. Soper. Highly efficient circulating tumor cell isolation from whole blood and label-free enumeration using polymer-based microfluidics with an integrated conductivity sensor. *J. Am. Chem. Soc.* **130**, 8633-8641 (2008).

150. M. Yamato, T. Okano. Cell sheet engineering. *Mater. Today.* **7**, 42-47 (2004).

151. S. Hou, H. Zhao, L. Zhao, Q. Shen, K.S. Wei, D.Y. Suh, A. Nakao, M.A. Garcia, M. Song, T. Lee, B. Xiong, S. Luo, H. Tseng, H. Yu. Capture and stimulated release of circulating tumor cells on polymer-grafted silicon nanostructures. *Adv. Mater.* **25**, 1547–1551 (2013).

152. H. Liu, X. Liu, J. Meng, P. Zhang, G. Yang, B. Su, K. Sun, L. Chen, D. Han, S. Wang, L. Jiang. Hydrophobic interaction-mediated capture and release of cancer cells on thermoresponsive nanostructured surfaces *Adv. Mater.* **25**, 922–927 (2013).

153. Z. Ke, M. Lin, J. Chen, J. Choi, Y. Zhang, A. Fong, A. Liang, S. Chen, Q. Li, W. Fang, P. Zhang, M.A. Garcia, T. Lee, M. Song, H. Lin, H. Zhao, S. Luo, S. Hou, H. Yu, H. Tseng· Programming thermoresponsiveness of nanovelcro substrates enables effective purification of circulating tumor cells in lung cancer patients. *ACS Nano* **9**, 62-70 (2015).

154. E. Reátegui, N. Aceto, E.J. Lim, J.P. Sullivan, A.E. Jensen, M. Zeinali, J.M. Martel, A.J. Aranyosi, W. Li, S. Castleberry, A. Bardia, L.V. Sequist, D.A. Haber, S. Maheswaran, P.T. Hammond, M. Toner, S.L. Stott. Tunable nanostructured coating for the capture and selective release of viable circulating tumor cells. *Adv. Mater*. **27**, 1593–1599 (2015).

155. Q. Shen, L. Xu, L. Zhao, D. Wu, Y. Fan, Y. Zhou, W. OuYang, X. Xu, Z. Zhang, M. Song, T. Lee, M.A. Garcia, B. Xiong, S. Hou, H. Tseng, X. Fang. Specific capture and release of circulating tumor cells using aptamer-modified nanosubstrates. *Adv. Mater*. **25**, 2368–2373 (2013).

156. A.M. Shah, M. Yu, Z. Nakamura, J. Ciciliano, M. Ulman, K. Kotz, S.L. Stott, S. Maheswaran, D.A. Haber, M. Toner. Biopolymer system for cell recovery from microfluidic cell capture devices. *Anal. Chem*. **84**, 3682−3688 (2012).

157. W. Li, E. Reategui, M. Park, S. Castleberry, J.Z. Deng, B. Hsu, S. Mayner, A.E. Jensen, L.V. Sequist, S. Maheswaran, D.A. Haber, M. Toner, S.L. Stott, P.T. Hammond. Biodegradable nano-films for capture and non-invasive release of circulating tumor cells. *Biomaterials* **65**, 93-102 (2015).

158. O. Gentil, Y. Akiyama, M. Schuler, C. Tang, M. Textor, M. Yamato, T. Okano, J. Vörös. Polyelectrolyte coatings with a potential for electronic control and cell sheet engineering. *Adv. Mater.* **20**, 560–565 (2008).

159. K.M. Persson, R. Karlsson, K. Svennersten, S. Löffler, E.W.H. Jager, A.R. Dahlfors, P. Konradsson, M. Berggren. Electronic control of cell detachment using a self-doped conducting polymer. *Adv. Mater.* **23**, 4403–4408 (2011).

160. Y.S. Hsiao, B.C. Ho, H.X. Yan, C.W. Kuo, D.Y. Chueh, H. Y, P. Chen. Integrated 3D conducting polymer-based bioelectronics for capture and release of circulating tumor cells. *J. Mater. Chem. B* **3**, 5103-5110 (2015).

161. S. Jeon, W. Hong, E.S. Lee, Y. Cho. High-purity isolation and recovery of circulating tumor cells using conducting polymer-deposited microfluidic device. *Theranostics* **4**, 1123-1132 (2014).

162. H. Liu, Y. Li, K. Sun, J. Fan, P. Zhang, J. Meng, S. Wang, L. Jiang. Dual-responsive surfaces modified with phenylboronic acid-containing polymer brush to reversibly capture and release cancer cells. *J. Am. Chem. Soc.* **135**, 7603−7609 (2013).

163. A. Hatch, G. Hansmann, S.K. Murthy. Engineered alginate hydrogels for effective microfluidic capture and release of endothelial progenitor cells from whole blood. *Langmuir* **27**, 4257–4264 (2011).

164. M.H. Park, E. Reatégui, W. Li, S.N. Tessier, K.H. Wong, A.E. Jensen, V. Thapar, D. Ting, M. Toner, S.L. Stott, P.T. Hammond. Enhanced isolation and release of circulating tumor cells using nanoparticle binding and ligand exchange in a microfluidic chip. *J. Am. Chem. Soc.* **139**, 2741−2749 (2017).

165. S.W. Lv, Y. Liu, M. Xie, J. Wang, X. W. Yan, Z. Li, W.G. Dong, W.H. Huang. Near-infrared light-responsive hydrogel for specific recognition and photothermal site-release of circulating tumor cells. *ACS Nano* **10**, 6201−6210 (2016).

Chapter 2

High Thermal Conductivity in Amorphous Polymer Blends by Engineered Interchain Interactions

Nature Materials **14**, 295-300 (2015); published by Nature Publishing Group

2.1 Introduction

Thermal conductivity is an important property for polymers, as it often affects product reliability (for example, electronics packaging), functionality (for example, thermal interface materials) and/or manufacturing cost.[1] However, polymer thermal conductivities primarily fall within a relatively narrow range (0.1–0.5 $Wm^{-1}K^{-1}$) and are largely unexplored.

A common method to enhance a polymer's thermal conductivity (κ) is to blend it with high-κ fillers such as metal[2] or ceramic[3] particles, yielding reported values of κ that range from 1 to 10 $Wm^{-1}K^{-1}$ (refs. 2, 3). However, the large amount of fillers required to exceed the percolation threshold can not only significantly increase the material cost (for example, nylon-6,6: \$2 kg^{-1} versus alumina particles: \$100 kg^{-1}) but may also change other important characteristics such as electrical and optical properties. Alignment of polymer chains[4–7] has been another route explored to realize high κ in polymers, although

these high values of κ are limited to the direction of chain orientation and require certain fabrication techniques (for example, electrospinning[4], nanoscale templating[5], mechanical stretching[8]). For practical applications, high-κ polymers that are more compatible with conventional manufacturing processes (for example, solution casting) are desired, yet no such materials with $\kappa > 0.6$ Wm^{-1}K^{-1} have been reported without the aid of high-κ fillers.

The underlying mechanisms of thermal conductivity in amorphous materials are not completely understood, with separate studies indicating important contributions to heat transfer by the diffusion of energy through non-propagating vibrational modes[9,10], the anharmonic coupling of localized modes[11], and the ballistic propagation of delocalized modes[12]. In polymer systems, high κ measured in aligned systems[4–7] suggests that heat is transferred much more efficiently along a covalently bonded chain than between chains bonded by weak van der Waals (vdW) interactions. Increasing the strength of a molecular bond has been shown to improve its thermal conductance in a nanomolecular monolayer[13]; improvements in interchain thermal conductance may likewise contribute to improvements in bulk polymer thermal conductivity. However, interchain bond strength alone does not dictate κ in bulk polymers, as evidenced by minuscule improvements in κ for crosslinked polymers[14] as well as low values of κ for numerous polymers capable of strong hydrogen bonding (for example, nylon-6,6: 0.25 Wm^{-1}K^{-1}; ref. 15).

Rather, maximizing interchain thermal conductance in a bulk polymeric material requires that strong intermolecular bonds used to replace weak vdW interactions must connect as closely as possible to the polymer backbones through a low-mass and short chemical linker. Furthermore, it is critical that a homogeneous distribution of these bonds

is achieved at a concentration above the percolation threshold to form a continuous thermal network (Figure 2.1).
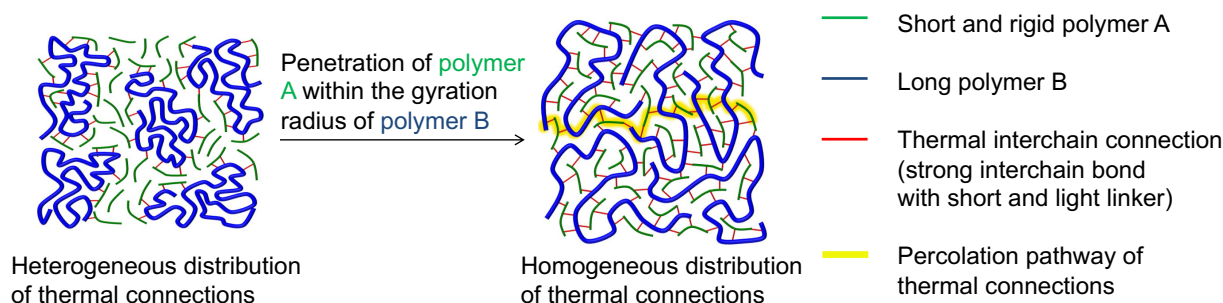
Figure 2.1 | **High thermal conductivity in amorphous polymer blends by engineered interchain interactions.** Illustrations of heterogeneous (*left*) and homogeneous (*right*) distributions of thermally conductive interchain connections at the same concentration of H-bonding moieties, showing how the homogeneity of the bonding distribution can affect the formation of percolating thermal pathways. The relatively short and rigid polymer A penetrates within the gyration radius of a longer polymer B and holds it in an extended conformation by means of strong interchain bonds, improving both intrachain and interchain heat transfer.

Hydrogen bonding (H-bonding) is approximately 10–100 times stronger than the vdW interaction[16]. There are numerous available H-bonding-capable moieties and linker units, allowing sufficient design flexibility to investigate thermally conductive interchain connections. To achieve a large number of inter-polymer H-bonds, the H-bond-donating and -accepting polymers should have high number densities of H-bond-capable moieties. To realize a uniform and homogeneous distribution of H-bonds, the H-bond-accepting and -donating polymers are required to be not only homogeneously dispersed, but also miscible at the molecular level to allow polymers to intertwine within the radius of gyration.[17] Here, we show that a blend of two polymers with high miscibility and appropriately chosen linker structure can yield a dense and homogeneously distributed thermal network. A sharp increase in cross-plane thermal conductivity is observed under

these conditions, reaching over 1.5 Wm^{-1}K^{-1} in typical spin-cast polymer blend films of nanoscale thickness, which is approximately an order of magnitude larger than that of other amorphous polymers.

2.2 Experimental Section

2.2.1 Chemicals and Materials

Acryloyl chloride (Fluka), azobisisobutyronitrile (AIBN) (Aldrich), piperidine (Aldrich), and triethylamine (Aldrich) were used without further purification. AIBN was recrystallized from methanol. Poly(acrylic acid) (PAA) (Aldrich, M_v = 450 kDa), poly(vinyl alcohol) (PVA) (Aldrich, 80% hydrolyzed, M_w = 10 kDa) and poly(4-vinyl phenol) (PVPh) (Aldrich, M_w = 25 kDa) were used without further purification. The weight average molecular weight (M_w) of PAA is expected to be somewhat larger than its viscosity average molecular weight (M_v) provided by Aldrich. Dichloromethane (DCM), diethyl ether, methanol, hexane, ethyl acetate, and anisole were used as solvents without further purification. *N,N*-dimethylformamide (DMF) (Aldrich, anhydrous, 99.8%) was used in sample preparation for thermal conductivity and IR measurements.

2.2.2 Polymer Synthesis

N-acryloyl piperidine was synthesized according to a previously reported method[18] with some modifications. In a typical reaction, 0.11 mole of piperidine and 0.12 mole of triethylamine were dissolved in 100 ml DCM. The solution was then added dropwise over 3 hr under constant stirring to a 7.5 ml DCM solution of acryloyl chloride maintained at 3-5 °C. After complete addition, the reaction mixture was stirred at room temperature for 24

hours. The resulting mixture was extracted using DCM and water and purified by column chromatography (hexane:ethyl acetate 1:1) to yield colorless to light yellow liquid. *N*-acryloyl piperidine was polymerized via free radical polymerization using AIBN as initiator. In the polymerization process, 5 millimole of acryloyl piperidine and 0.015 millimole of AIBN were dissolved in anisole, and the solution was purged with argon for 30 minutes. The monomer/solvent weight ratio was kept at ~20% and the reaction was carried out at 60-65 °C for 24 hours. The PAP polymer (M_w = 58 kDa) was precipitated in diethyl ether and dried under vacuum overnight (Figure 2.2).
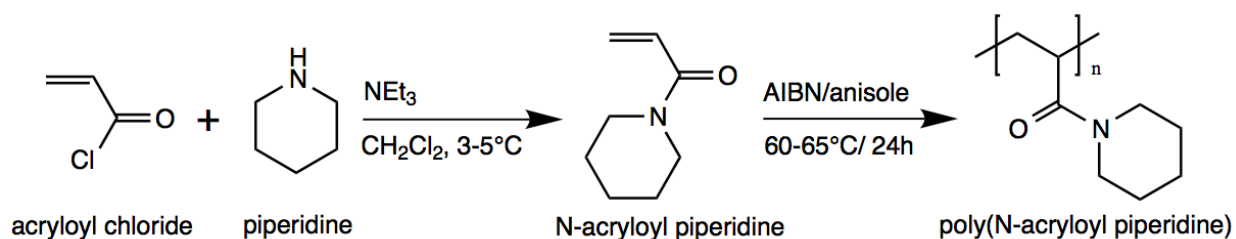
Figure 2.2 | Synthetic scheme for poly(*N*-acryloyl piperidine), PAP

2.2.3 Sample Preparation

1 wt.% of PAP, PAA, PVA, and PVPh were separately dissolved in DMF and heated to 150°C for 10 minutes to ensure complete dissolution. Solutions of PAA, PVA, and PVPh were then separately mixed with the PAP solution, and the mixed solutions were heated to 150°C for 5 minutes. The mixture ratio (i.e., φ_{PAP}) was calculated as (# PAP monomers) / (# PAP monomers + # H-bond donating monomers) in order to best quantify the control of φ_H by φ_{PAP}. DMF was chosen as a solvent to avoid polymer aggregation and precipitation due to H-bonding between the two polymers in solution.

Solutions of various mixture ratios were spin-cast (Laurell Technologies Corporation, Model: WS-650MZ- 23NPP/LITE) on a pre-cleaned (sequential sonication

with detergent, deionized water, acetone, and isopropanol, followed by UV ozone treatment for 20 minutes) heavily doped silicon substrate at 1500 rpm for 30 seconds. The spin-cast films were annealed at 150°C for 15 minutes and kept in a vacuum chamber for 30 minutes. All processes from spin-casting to thermal annealing were done under nitrogen atmosphere. To create the reference region for 3ω measurement, part of the spin-cast film was removed after thermal annealing by a steel blade; the residual discontinuous film in this area was then further removed by a swab soaked in acetone and isopropanol, resulting in a clean substrate surface with no polymer residuals.

2.2.4 Thermal Conductivity Measurement: Differential 3ω Method

2.2.4.1 3ω Set-up and Measurement

The differential 3ω method can be used to measure the temperature rise across a film of interest without uncertainties associated with the thermal properties of other layers. In our samples, the only difference between the sample and reference regions is the presence of the polymer film (Figure 2.3a), causing the difference in temperature rise for the two regions to represent the temperature rise across the polymer film. For a heater line with a large width (50 μm) compared to the film thickness (< 100 nm), heat conduction through the polymer film is approximately 1-dimensional, and κ can be calculated using Fourier's 1D conduction law:

$$\kappa_y = \frac{P_s.d_f}{wl\Delta T_f} \tag{1}$$

where P_s is the heating power applied to the sample region, d_f is the polymer film thickness, w and l are the width and the length of the heater line, and y is the coordinate

perpendicular to the substrate. The temperature rise ΔT_f across the polymer film is given by[19]:

$$\frac{\Delta T_f}{P_s} = \frac{\Delta T_s}{P_s} - \frac{\Delta T_r}{P_r} \tag{2}$$

where P and ΔT are the applied heating power and resulting temperature rise for heater lines on the sample (subscript "s") and reference (subscript "r") regions, respectively. It should be noted that Eq. 2 assumes identical w and l for the heater lines on the two regions. ΔT_s and ΔT_r can be experimentally determined from the measured voltages oscillating at 3ω and ω (measured by SR830 Lock-in Amplifier, Stanford Research Systems)[20]:

$$\Delta T = 2R\frac{dT}{dR}\frac{V_{3\omega}}{V_\omega} \tag{3}$$

where dR/RdT is the temperature coefficient of electrical resistance in the metal line.

The thermal penetration depth (δ) is given by $(\alpha_{sub}/2\omega)^{1/2}$,[20,21] where α_{sub} is the thermal diffusivity of the substrate. For a silicon substrate (α_{sub} = 0.8 cm^{2}s^{-1}) that is heated by alternating current at 100 Hz, δ is calculated to be 252 μm. Since this is much larger than the half-widths of the heaters (1–2 μm or 25 μm), the heaters satisfy the condition of a line heat source, and since it is smaller than the substrate thickness (550 or 700 μm), the measured ΔT is independent of the boundary condition at the bottom of the substrate. Parasitic effects due to a penetration depth which is too short would be expected to appear as a nonlinearity in ΔT versus log(ω)[20,21]; however, as shown in Figure 2.3b, ΔT_s and ΔT_r are quite linear versus log(ω). Furthermore, the potential error due to a penetration depth which is too short would be greatly reduced by the differential nature of our measurement ($\Delta T_f = \Delta T_s - \Delta T_r$), particularly since the thicknesses of the sample films

57

(<75 nm) are much smaller than the penetration depths over the range of frequencies used and heat transfer within the films is 1-dimensional.
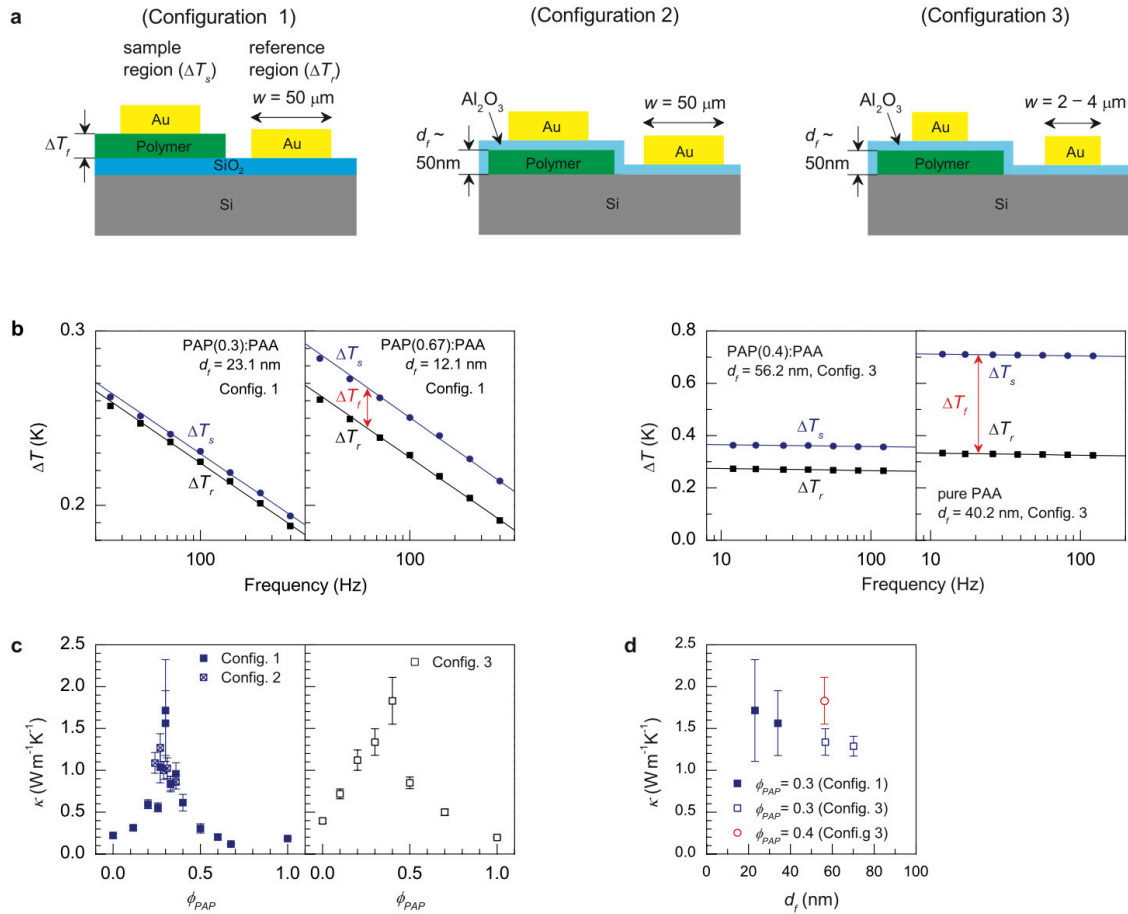
Figure 2.3 | 3ω measurement of thermal conductivity (κ). a, Cross-section of the sample geometry for three different configurations used. While only wide heater lines defined by shadow masking were used for Configuration 1, narrow lines could be patterned by photolithography without damaging the polymer blend for Configuration 3. **b**, Temperature rise on the sample (ΔT_s) and reference regions (ΔT_r), the difference of which is the temperature rise across the polymer film (ΔT_f). **c**, Comparison of measured thermal conductivities in different PAP:PAA films measured using wide (*left*) and narrow (*right*) heater lines in Configurations 1 and 2 (closed symbols) or 3 (open symbols). **d**, κ measured for five different PAP:PAA samples at φ_{PAP} = 0.3 or 0.4 using Configuration 1 or 3. Narrow heater lines lead to decreased $(\Delta T_s^2 + \Delta T_r^2)^{1/2} / \Delta T_f$ and thereby improved signal-to-noise ratio.

For 3ω measurements with 50 μm heater line width, either a silicon substrate capped with a thin SiO$_2$ layer or a bare silicon substrate on which a thin (40 nm) Al$_2$O$_3$

layer (1.5 $Wm^{-1}K^{-1}$) was deposited at 80°C by atomic layer deposition following polymer coating was used; for 3ω measurements with 2–4 μm heater line width, a bare silicon substrate on which a thin (40 nm) Al_2O_3 layer was deposited at 80°C by atomic layer deposition following polymer coating was used. 50 μm wide heater lines (5 nm thick Ti followed by 300 nm thick Au) were then deposited by electron-beam deposition in vacuum simultaneously on both sample and reference regions. Narrow heater lines between 2 μm and 4 μm wide (measured with 0.18 μm error by optical microscopy) and 260 μm long were patterned by photolithography on an Al_2O_3 (40 nm thick, 1.5 $Wm^{-1}K^{-1}$) layer that was used to both electrically isolate the substrate from the gold heater line (the polymer films themselves being insulating) and shield the sample film from the chemicals used during photolithography. Thermal conductivities measured using 50 μm and 2-4 μm heater lines were similar in values (Figure 2.3c). Narrow heater lines gave lower error compared to the wider heater lines (Figure 2.3d).

2.2.4.2 Error Analysis

A key assumption for the differential 3ω technique is that all conditions between the sample and reference regions are identical except the presence of the thin film of interest. While uncertainties originating from variations in the thermal properties of the substrate and SiO_2 can be minimized by making the sample and the reference regions close to each other (~10 mm) as well as by using a single crystal substrate, several parameters (e.g., d_f, dR/RdT, and w in Eqs. 1, 2, and 3) are subject to experimental uncertainties and must be independently determined.

Thickness measurements The polymer film thickness (d_f) was measured by three different methods: surface profilometry (Dektak XT Surface Profilometer), ellipsometry (Woollam M-2000DI ellipsometer), and atomic force microscopy (AFM) (Bruker ICON AFM). Among the three thicknesses measured by the Dektak, averaged AFM topography, and ellipsometry, we chose to use the thicknesses measured by ellipsometry for all compositions of PAP:PAA (and other blends) in order to set a lower bound for the derived κ, which is proportional to thickness (d_f). Ellipsometry has been shown to measure the thickness of a thin polymer film with an error less than 5 Å;[22] the error in thickness for the films measured by ellipsometry in this work is set to be ±3% based on 5 Å error for the minimum film thickness (20 nm).

Temperature coefficient of resistance and heating wire width dR/RdT and w were measured in forty heater lines to obtain standard deviations of ±2.7% and ±1.1%, respectively. While error in dR/RdT is largely mitigated when calculating the difference between ΔT_s and ΔT_r since the gold heater lines on the sample and reference regions are deposited at the same time, error in w is magnified[19] by $(\Delta T_s^2 + \Delta T_r^2)^{1/2}/\Delta T_f$ and affects ΔT_s and ΔT_r independently. In other words, a small independent variation in ΔT_s or ΔT_r can lead to a large variation in ΔT_f depending on the magnitude of $(\Delta T_s^2 + \Delta T_r^2)^{1/2}/\Delta T_f$. For this reason, $\sigma_{SDEV,w} \times (\Delta T_s^2 + \Delta T_r^2)^{1/2}/\Delta T_f$ rather than $\sigma_{SDEV,w}$ was used when calculating the error in κ.

Thermal boundary resistance Metal heaters and Al_2O_3 in the sample and reference regions were deposited at the same time on the same substrate with a small separation distance of 10 mm in order to minimize variations in thermal boundary conductances (TBCs) between the two regions. To assess the potential impact of TBC variations, we

can calculate the TBCs that would be required to generate the lumped thermal conductances (polymer film + TBCs above and below it) that were measured, if the polymer film were assumed to have a constant value of κ = 0.5 $Wm^{-1}K^{-1}$ for all blend fractions. Assuming a typical[23] TBC of 100 $MWm^{-2}K^{-1}$ for the Ti/SiO$_2$ interface in the reference region, the required total TBC (for interfaces on both sides of the polymer film) in the sample region is plotted in Figure 2.4a. For the samples near φ_{PAP} = 0.3, the
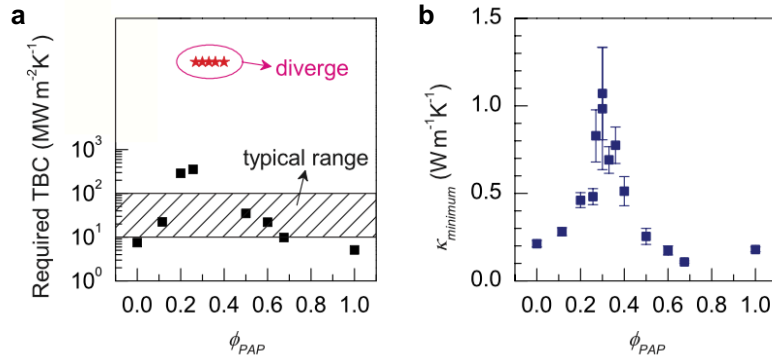
Figure 2.4 | Thermal boundary conductance and minimum κ. a, Total thermal boundary conductance (TBC) on either side the polymer film that is required to fit the measured data (from Configuration 1) under the assumption of a constant κ = 0.5 $Wm^{-1}K^{-1}$ for the polymer film. TBC for Ti/SiO$_2$ in the reference region is assumed to be 100 $MWm^{-2}K^{-1}$. **b**, Minimum κ the polymer film would need to have in order to fit the measured data (from Configuration 1), if a TBC of 100 $MWm^{-2}K^{-1}$ is again assumed for the Ti/SiO$_2$ interface in the reference region and the two interfaces in the sample region are allowed to have zero resistance.

required TBC diverges, as a polymer film with κ = 0.5 $Wm^{-1}K^{-1}$ would not be able to fit the data even if the interfaces on either side of it had zero thermal resistance. This same concept is presented in Figure 2.4b, which plots the minimum thermal conductivity the polymer film would need to have in order to fit the data, if a TBC of 100 $MWm^{-2}K^{-1}$ were again assumed for the Ti/SiO$_2$ interface in the reference region and the two interfaces in the sample region were allowed to have zero resistance. We note that in reality the

thermal boundary resistance of the polymer/SiO$_2$ interface is not zero and may well be larger than that of the Ti/SiO$_2$ interface,[23,24] making the true thermal conductivities of the blend films even larger than the values presented here.

2.2.5 Materials Characterization

2.2.5.1 Fourier Transform Infrared (FTIR) Spectroscopy and Calculation of H-bond Concentration

FTIR was performed by a Nicolet 6700 spectrometer using the grazing angle accessory (Smart SAGA) at a grazing angle of 85°; 128 scans were taken for each sample followed by a blank measurement for calibration. IR spectra were deconvoluted using Origin 8 data analysis and graphing software. IR spectra of PAP:PAA and PAP:PVPh were fit with Gaussian function with five peaks and four peaks, respectively. While the width and peak center were user defined, the area under the curve was automatically calculated by the software. Figure 2.5a shows a representative IR spectrum with deconvoluted peaks for PAP:PAA (φ_{PAP} = 0.3) in the carbonyl (C=O) stretching region of PAP and PAA. It is well known that the C=O stretching peak is shifted to a lower wavenumber for an H-bond acceptor, while the shift is opposite for an H-bond donor.[25-28] H-bonding between PAP and PAA results in the PAP C=O stretching peak (Peak 1) shifting from 1645 cm^{-1} to a lower wavenumber near 1602-1614 cm^{-1}; likewise, it results in the PAA C=O stretching peak (Peak 5) shifting from 1720 cm^{-1} to a higher wavenumber near 1737-1742 cm^{-1}. Since the carboxyl groups in PAA have both H-bond donor (OH) and H-bond acceptor (C=O) units, it can form self-associated H-bonding, resulting in a shift in the carbonyl stretching peak (Peak 3) to a lower wavenumber near 1700-1702 cm$^-$

1. Given the fact that Peaks 1 and 5 originate from the same H-bonding, the fraction of intermolecular bonds in PAP:PAA that are H-bonds (φ_H) can be calculated by:

$$\varphi_H = 0.5\left(\frac{A_{Peak1}}{A_{Peak1} + A_{Peak2}}\varphi_{PAP} + \frac{A_{Peak5}}{A_{Peak3} + A_{Peak4} + A_{Peak5}}\varphi_{PAA}\right) + \frac{A_{Peak3}}{A_{peak3} + A_{Peak4} + A_{Peak5}}\varphi_{PAA} \quad (4)$$

where A_{peakX} is the area of Peak X.
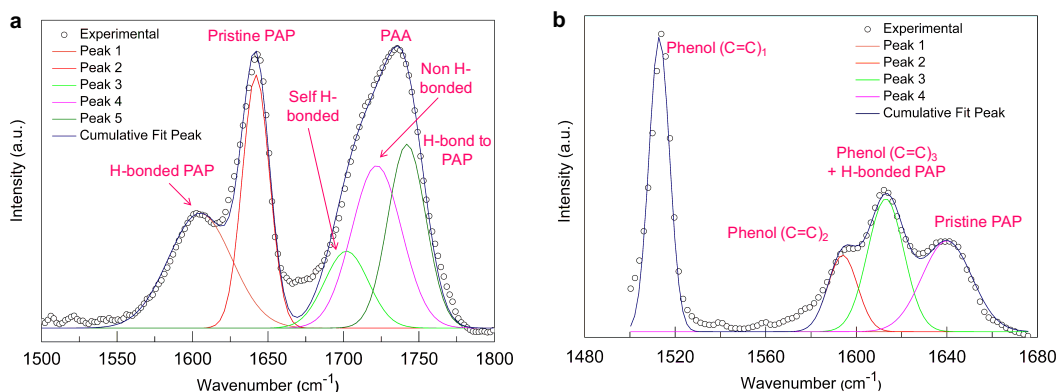
Figure 2.5 | Representative FTIR spectra with deconvoluted peaks. a, PAP:PAA. **b,** PAP:PVPh.

Figure 2.5b shows a representative FTIR spectrum with deconvoluted peaks for the PAP:PVPh pair in the arene C=C stretching region of PVPh and the carbonyl C=O stretching region of PAP. Because the peak formed by H-bonded PAP carbonyl stretching overlaps with the third benzene C=C peak of pure PVPh (these benzene peaks being known[29,30] to occur at 1513 cm⁻¹ (Peak 1), 1596 cm⁻¹ (Peak 2), and 1612 cm⁻¹ (Peak 3)), we implemented a procedure to isolate the H-bonded PAP carbonyl stretching contribution as follows. The areal ratios of the three benzene C=C peaks were first obtained from the IR spectrum of pure PVPh ($A_{peak3} = 0.25A_{peak1}$ and $A_{peak2} = 0.13A_{peak1}$). The areal ratio of Peaks 1 and 2 was found to be nearly the same for pure PVPh and PAP:PVPh blends, but the areal ratio of Peaks 1 and 3 was found to be quite different,

suggesting that H-bonded PAP carbonyl stretching has a strong contribution at 1612 cm^{-1}. The fraction of intermolecular bonds in PAP:PVPh that are H-bonds was then calculated by subtracting the areal contribution of the benzene C=C peak from the total peak area at 1612 cm^{-1} and comparing the resultant area to Peak 4 (which arises in PAP:PVPh due to non-H-bonded PAP carbonyl stretching):

$$\varphi_H = \frac{A_{Peak3} - 0.25 A_{Peak1}}{A_{Peak3} - 0.25 A_{Peak1} + A_{Peak4}} \varphi_{PAP} \tag{5}$$

It should be noted however that φ_H as calculated by Eq. 5 does not include the self-associated H-bonding of PVPh, as the hydroxyl (–OH) peak in PVPh is too broad (3200-3500 cm^{-1}) to perform reliable deconvolution. For this reason, φ_H plotted for PAP:PVPh in Figure 2.7d is likely underestimated.

2.2.5.2 Atomic Force Microscopy (AFM)

Morphological and compositional properties of the polymer blends were studied using tapping-mode AFM (Bruker ICON AFM), the phase images of which are known to correlate with spatial variations in surface stiffness[31] (which relates to the density of H-bonds) and polymer chain density.[32] The AFM tip and measurement settings were kept the same when obtaining images for PAP:PAA, PAP:PVA, and PAP:PVPh.

2.2.5.3 Differential Scanning Calorimetry (DSC)

Glass transitions of PAP:PAA at various φ_{PAP} were studied based on DSC curves measured under nitrogen gas by a TA Instruments Discovery Series DSC. PAP:PAA solutions (1 wt.%) were drop-cast on a glass substrate and annealed at 150°C for 20

minutes. Each dried film was ground to a fine powder and stored in a vacuum chamber for 10 hours, after which it was sealed in a Tzero hermetic pan and used for DSC measurements. DSC samples were first heated to 220°C at a rate of 20°Cmin^{-1}, then cooled down to 0°C at 15°Cmin^{-1}, and finally heated at a rate of 10°Cmin^{-1}; during this final heating, glass transition data was obtained.

2.2.5.4 Positronium Annihilation Lifetime Spectroscopy (PALS)

PALS data for PAP:PAA and PAP:PVPh blends were acquired using a focused positron beam having a positron implantation energy of 1.2 keV. PAP showed a positronium (Ps) intensity of (19±1) % with a corresponding Ps lifetime in its free volume voids of $1.70\pm0.05\times10^{-9}$ s; PAA showed a low Ps intensity of (2.6±0.1)% with a corresponding Ps lifetime of $(2.7\pm0.1)\times10^{-9}$ s; and PVPh showed a Ps intensity of (10.3±0.3)% with a corresponding Ps lifetime of $(2.4\pm0.1)\times10^{-9}$ s. It is noted that the larger Ps intensity of PAP compared to that of PAA does not necessarily represent a larger free volume in PAP compared to PAA, since the Ps formation yield is different for each polymer due to their different chemistries. In contrast, changes in the product of Ps intensity and lifetime within the same polymer represent changes in its free volume. In polymer blends, Ps is formed and annihilated in each component polymer according to its weight fraction.

2.2.5.5 Grazing-incidence X-ray Scattering

Grazing-incidence small angle (GISAXS) and wide angle (GIWAXS) X-ray scattering measurements for spin-cast PAP:PAA thin films were carried out on a Rigaku

Rotating Anode X-Ray Diffractometer (X-ray wavelength: 1.54 Å). A single crystalline silicon substrate was used as it introduces negligible background signal at the grazing angle used (1°). Each PAP:PAA film used for GIXS measurements was prepared by multiple (50×) spin-castings in order to maximize the signal from the film.

2.3 Results and Discussion

To investigate the hypotheses put forth in Section 2.1, we rationally designed three polymer pairs in which the H-bond-accepting polymer, PAP, was fixed. PAP has a strong H-bond-accepting amide functional group as a side chain on every other carbon atom along its backbone, allowing a direct thermal connection to its backbone. Its piperidine ring is expected to make its backbone rigid[33] and promote extended conformation for polymers with which it interacts through strong H-bonds. Three H-bond-donating polymers, viz., PAA, PVA, and PVPh, were chosen to examine the effects of several different H-bonding strategies on κ (Figure 2.6). PAA, PVPh, and PVA each has a H-bond-donating –OH group associated with every other carbon atom along their backbones; however, they differ both in how the –OH group attaches to the polymer backbone and in the H-bond-donating power of the –OH group. The high acidities of the carboxylic acid (–COOH) in PAA and the phenol (–PhOH) in PVPh give their –OH groups a stronger H-bond-donating power than the –OH groups in PVA. While the –OH is closely connected to the backbone in PAA and PVA, it is linked to the backbone via a benzene ring in PVPh.

Cross-plane thermal conductivities (perpendicular to the centrifugal force during spin-casting) of the spin-cast polymer blend films were measured by the differential 3ω

method.[19,20] Figure 2.6 summarizes the measured thermal conductivities of PAP blend films with PAA, PVA, or PVPh at various fractions of PAP in the blend (φ_{PAP}). Certain blends of PAP:PAA yielded an exceptionally homogeneous distribution of strong H-bonds at a concentration that exceeded the percolation threshold (*vide infra*). For these blends,
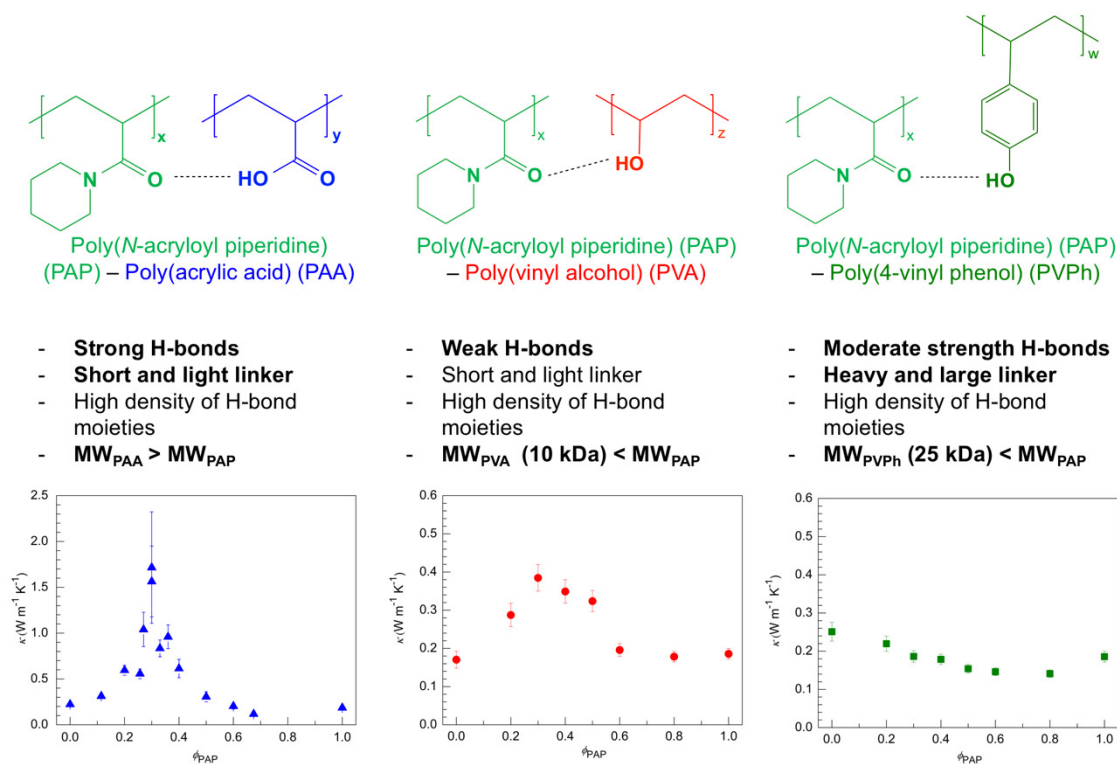
Figure 2.6 | Measured thermal conductivities of spin-cast blend films. a, PAP:PAA, **b,** PAP:PVA and **c,** PAP:PVPh films at various monomer mole fractions of PAP (φ_{PAP}). Error bars were estimated based on uncertainties associated with the film thickness, the temperature coefficient of electrical resistance for the heater, and the heater width.

κ was measured to be greater than 1.5W m^{-1}K^{-1}, which is nearly an order of magnitude larger than that of its constituent components, PAP (0.19 ± 0.02Wm^{-1}K^{-1}) and PAA (0.22 ± 0.02 Wm^{-1}K^{-1}). While PAP:PVA shows a trend of increased κ similar to PAP:PAA, its thermal conductivity gain is much smaller (κ = 0.38 ± 0.04 Wm^{-1}K^{-1}), consistent with its weaker H-bond strength. In contrast, the thermal conductivity of PAP:PVPh, which forms

stronger H-bonds than PAP:PVA, shows no enhancement relative to values for the pure PAP and PVPh constituents. As discussed in more detail below, we attribute this in part to the fact that the H-bond-donating hydroxyl group does not attach directly to the PVPh backbone but rather via a benzene ring as a linker, similar to crosslinked polystyrene.[34]
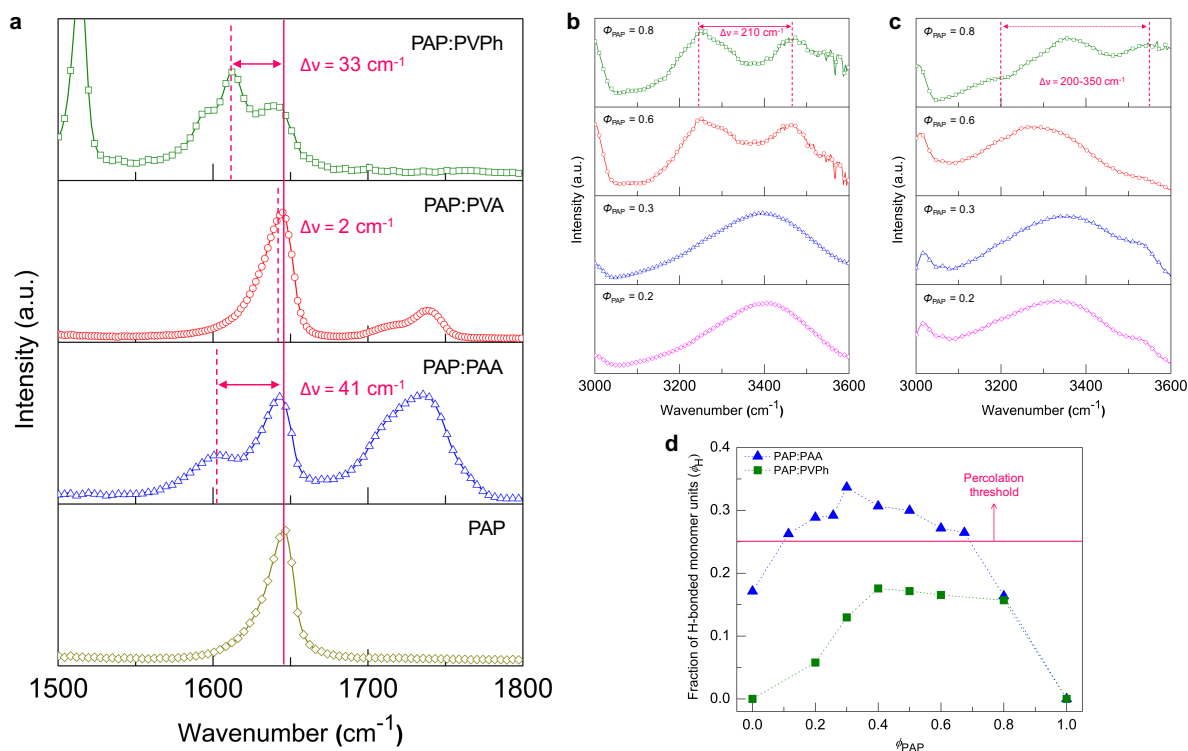
Figure 2.7 | FTIR spectra of polymer blends. a, FTIR spectroscopy data for PAP:PAA, PAP:PVPh and PAP:PVA at φ_{PAP} = 0.3 showing the relatively peak shifts for carbonyl (-C=O) stretching in PAP upon H-bonding with different H-bond donor polymers. **b, c** Hydroxyl (-OH) stretching region of FTIR spectra of PAP:PVA **(b)** and PAP:PVPh **(c)**. **d,** Fraction of H-bonded monomer unit (φ_H) in PAP:PAA and PAP:PVPh as calculated by areal integrations of the deconvoluted H-bonded and pristine carbonyl stretching bands shown in **a.** Also shown is the bonding percolation threshold for a simple cubic lattice (solid line).

FTIR spectroscopy was employed to quantify the strength and concentration of H-bonding for the polymer blends. Since the carbonyl (-C=O) moiety of the amide group on

the H-bond acceptor polymer, PAP, is the primary H-bond accepting site, the strength of H-bond formed can be gauged by the shift in the carbonyl stretching peak compared to that in pristine PAP. As can be seen in Figure 2.7a, the shift of the carbonyl (C=O) stretching band in PAP due to H-bond formation is large in PAP:PAA (41 cm^{-1}), modest in PAP:PVPh (33 cm^{-1}), and small in PAP:PVA (2 cm^{-1}), consistent with their reported H-bond strengths.[16] The relative H-bond strengths are further confirmed by the peak shift due to –OH single-bond stretching, which is large in PAP:PAA (500–1,000 cm^{-1}), and similar in PAP:PVPh (200–350 cm^{-1}; Figure 2.7b) and PAP:PVA (210 cm^{-1}; Figure 2.7c).

The fraction of intermolecular bonds that are H-bonds (φ_H) in PAP:PAA was estimated from the areal ratio of H-bond bands to pristine carbonyl stretching bands in FTIR spectroscopy data. We note that a certain number of H-bonds in PAP:PAA are self-associated within PAA. Accounting for the fact that PAP cannot form H-bonds with these self-associated PAA units, the largest number of H-bonds between PAP and PAA is expected to occur at φ_{PAP} = 0.33, which is close to the observed maximum shown in Figure 2.7d at φ_{PAP} =0.3. For this blend, φ_H reaches 0.34, which is greater than the bonding percolation threshold for a simple cubic lattice (0.25; ref. 35). On the other hand, φ_H for PAP:PVPh reaches up to only ~0.18 signifying that PAP:PVPh blend films lack a continuous network of H-bonded domains required to assist efficient thermal conduction. It is noted that φ_H is underestimated for PAP:PVPh blends as it doesn't include the self-associated H-bonding of phenolic hydroxyl groups.

Atomic force microscopy (AFM) was used to assess the homogeneity of H-bond distribution in the spin-cast blend films. Phase imaging in taping-mode AFM can characterize the spatial variations in surface stiffness[31] and thereby distinguish the stiff

H-bonded regions from the relatively softer regions with only vdW interactions.[36] Because

the AFM tip interacts with soft materials longer, a negative phase shift (appearing as a

dark color in the phase images of Figure 2.8a-c) represents a vdW-rich region, whereas

a positive phase shift (appearing as a bright color) corresponds to an H-bond-rich region.

Figure 8a-c show AFM phase images of PAP:PAA, PAP:PVA, and PAP:PVPh blends at

various PAP monomer fractions (φ_{PAP}). The phase images of PAP:PAA are observed to

get smoother (that is, exhibit a smaller standard deviation (σ_{sd}) in phase) as

φ_{PAP} approaches 0.3 (Figure 2.8f), the fraction at which both the maximum φ_H and the

maximum κ are observed. Also, the mean phase shift (θ_{mean}) becomes significantly

positive at φ_{PAP} = 0.3 (Figure 2.8e), which together with low σ_{sd} indicates a

homogeneously distributed dense network of H-bonds. We note that the rapid removal of

the solvent during spin-casting as well as the thin solution concentration (1 wt.%) likely

play important roles in producing a homogeneous network of H-bonds in the polymer

blend film. In thicker solutions, PAP and PAA are expected to aggregate due to their

strong H-bond interactions, leading to a heterogeneous H-bond network in the resulting

solid film. Consistent with φ_H lower than the percolation threshold for PAP:PVPh, it

showed significant phase roughness and a negative phase shift indicating film softness

(probably due to interference between the piperidine and benzene rings which disrupts

PAP and PVPh chain conformations) (Figure 2.8d).
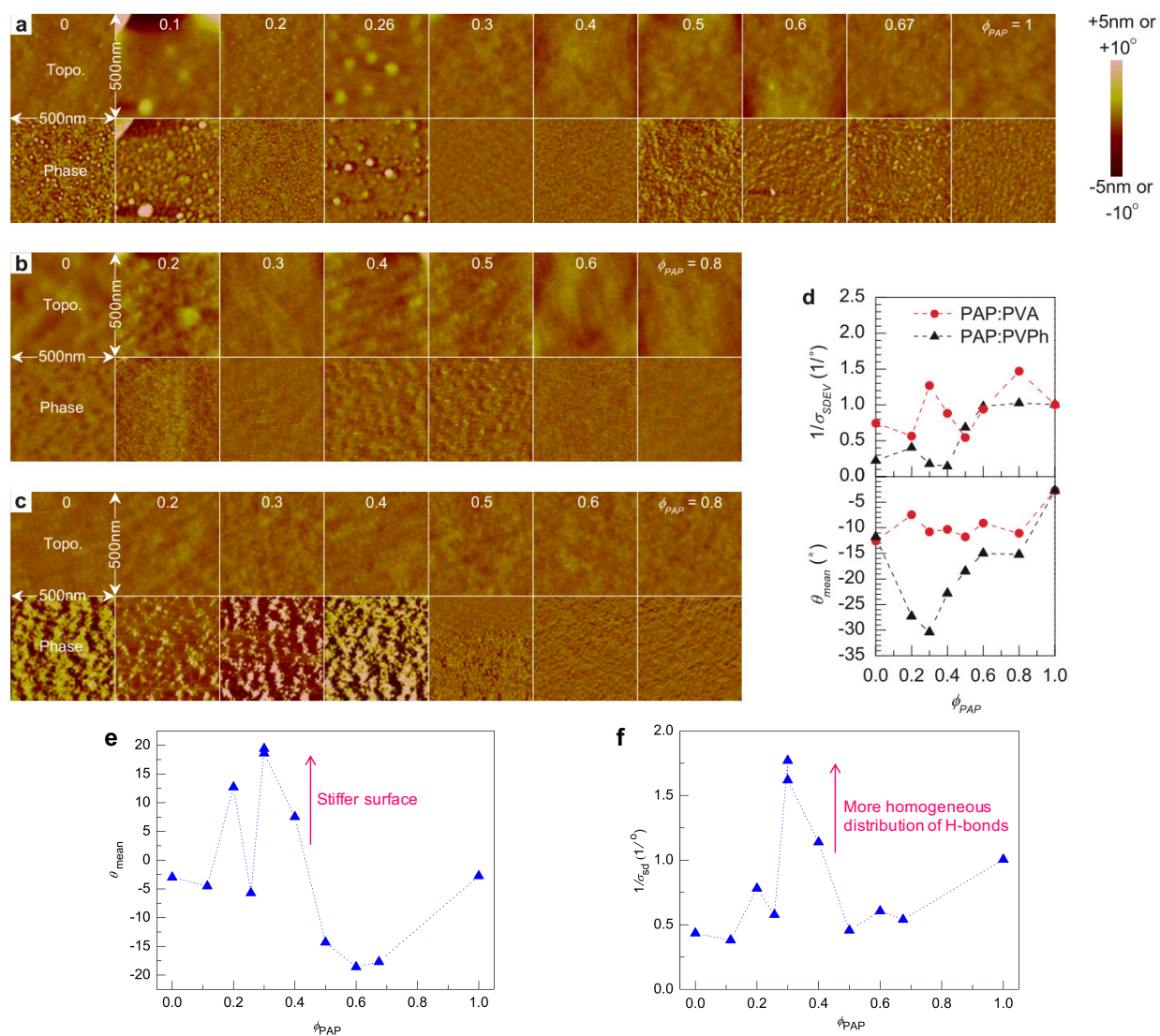
Figure 2.8 | Tapping-mode AFM topography and phase images for PAP:PAA, PAP:PVA and PAP:PVPh. AFM topography (upper) and phase (lower) images measured for PAP:PAA (**a**), PAP:PVA (**b**), and PAP:PVPh (**c**) at various φ_{PAP}. All images shown have a scanning area of 500nm × 500nm and were flattened (i.e., shifted to give zero mean value) for illustration purposes. **d**, Inverse of standard deviation extracted from AFM phase images (upper) and mean phase shift (before flattening) (lower) for PAP:PVA and PAP:PVPh. PAP:PVPh blends show the largest σ_{SDEV} and most negative θ_{mean}, which suggest a heterogeneous distribution of H-bonds and decreased chain packing density, respectively, and are consistent with its lack of enhancement in κ. **e,** θ_{mean} before image flattening, versus φ_{PAP} for PAP:PAA. **f,** Inverse of the standard deviation ($1/\sigma_{sd}$) of AFM phase data for PAP:PAA, indicating bonding homogeneity. PAP:PAA at φ_{PAP} =0.3 has the smallest σ_{sd} and largest θ_{mean}, indicating a dense and homogeneously distributed network of strong H-bonds.

71

The glass transition of a polymer blend provides information regarding the miscibility of its constituent polymers (Figure 2.9a).[17] For all PAP:PAA mixture ratios, the glass transition was found to occur at a single temperature (T_g), indicating uniform physical dispersion of PAP and PAA. T_g of PAP:PAA increased greatly for blends near φ_{PAP} = 0.3 (Figure 2.9b), indicating exceptionally strong H-bonding between PAP and PAA at that ratio. In fact, the difference of 48°C between measured (158°C) and theoretical Flory-Fox predicted (110°C) values is extraordinary among polymer blends in the literature.[37,38] Furthermore, the temperature range over which the glass transition occurs (T_g) was found to be narrow for $\varphi_{PAP} \leq 0.4$ (Figure 2.9d), indicating that PAP strongly interacts and intermixes with PAA within the PAA radius of gyration for this range of blends.[17] The change in specific heat capacity during the glass transition (ΔC_p) was found to decrease considerably as φ_{PAP} approaches 0.3 (Figure 2.9e). A primary contributor to a change in specific heat during a polymer's glass transition is a change in the degrees of freedom that occurs when the polymer transitions from a highly self-entangled state (Figure 2.9c) to a state in which the backbone is extended, as observed in polystyrene.[39]
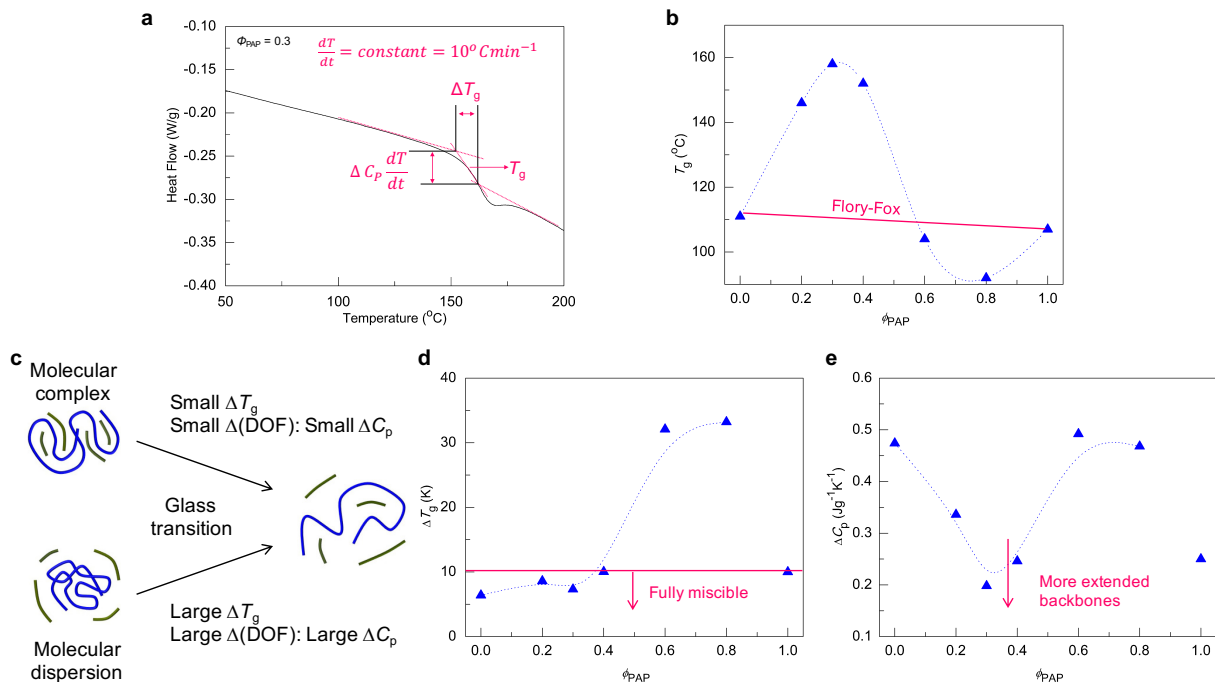
Figure 2.9 | Differential scanning calorimetry (DSC) data for PAP:PAA. a, Determination of glass transition temperature(T_g), glass transition width (ΔT_g) and change in specific heat capacity at glass transition (ΔC_p). T_g was set to the middle point of the solid line that connects two asymptotic dashed lines. **b,** T_g measured for PAP:PAA at various φ_{PAP}, indicating extraordinarily strong H-bonding for $\varphi_{PAP} \approx 0.3$. The solid line indicates T_g as predicted by the Flory–Fox equation, with the dashed line drawn to illustrate the data trend. **c,** Illustration of glass transitions in polymer blends with different degrees of miscibility and entanglement. **e, f,** ΔT_g (**e**) and ΔC_p (**f**) for PAP:PAA at various φ_{PAP}. Polymer blends with $\Delta T_g < 10^{\circ}$C are fully miscible, whereas those with $\Delta T_g > 32^{\circ}$C approach immiscibility. Blends with larger ΔC_p experience greater changes in their molecular degrees of freedom (DOF), indicating a transition from an un-extended to an extended conformation. Dashed lines were drawn to illustrate the data trend.

The minimum ΔC_p at φ_{PAP} = 0.3 therefore suggests that the backbones of both PAP and PAA are mostly extended for this blend before the glass transition at 158°C. In fact, ΔC_p for PAP:PAA at φ_{PAP} =0.3 is similar to that pure PAP of pure PAP but far lower than that of pure PAA, implying that the relatively rigid and short PAP chains penetrate within the PAA gyration radius and hold the flexible PAA chains in an extended state by means of strong H-bonds.[40] This extension of the PAA backbones is expected to improve intrachain

heat transport, similar to previous work in aligned polymers[4–7]; in contrast to studies of polymers at high hydrostatic pressures, in which the diffusion of energy through non-propagating vibrational modes was shown to dominate heat transfer.[10] While T_g exceeds the Flory–Fox prediction for $\varphi_{PAP} \leq 0.4$ (Figure 2.9b), indicating strong H-bonding, the fact that it is smaller than the Flory–Fox prediction for $\varphi_{PAP} > 0.4$ suggests phase inversion from a PAA matrix to a PAP matrix for this high range of PAP concentrations. Reduction in T_g due to phase inversion has previously been observed.[38] Likewise, T_g, ΔC_p and σ_{sd} become large for $\varphi_{PAP} > 0.4$, suggesting heterogeneous rather than homogeneous blends of PAP and PAA; as a consequence of phase inversion, the relatively flexible PAA chains, which have a large molecular weight and large radius of gyration, do not penetrate efficiently into the matrix of smaller PAP chains, leading to heterogeneous blends. Consequently, κ in PAP:PAA did not exhibit a meaningful increase for $\varphi_{PAP} > 0.4$.

To rule out any density- and crystallinity-related contributions to observed high thermal conductivity in PAP:PAA blends, positronium annihilation lifetime spectroscopy (PALS) and x-ray scattering were used to assess film porosity and crystallinity, respectively. PALS data indicate a smooth change in mass density between pure PAA and pure PAP, with no anomalies present that would suggest a density-related contribution to the sharply peaked increase in κ near $\varphi_{PAP} = 0.3$ (Figure 2.10b). PAP:PVPh too had a smooth reduction in density from pure PVPh to pure PAP, consistent with the measured decline in κ. Grazing-incidence small- and wide-angle x-ray scattering (GISAXS and GIWAXS) data did not show any sign of short or long-range order in PAP:PAA blend films (Figure 2.10c).
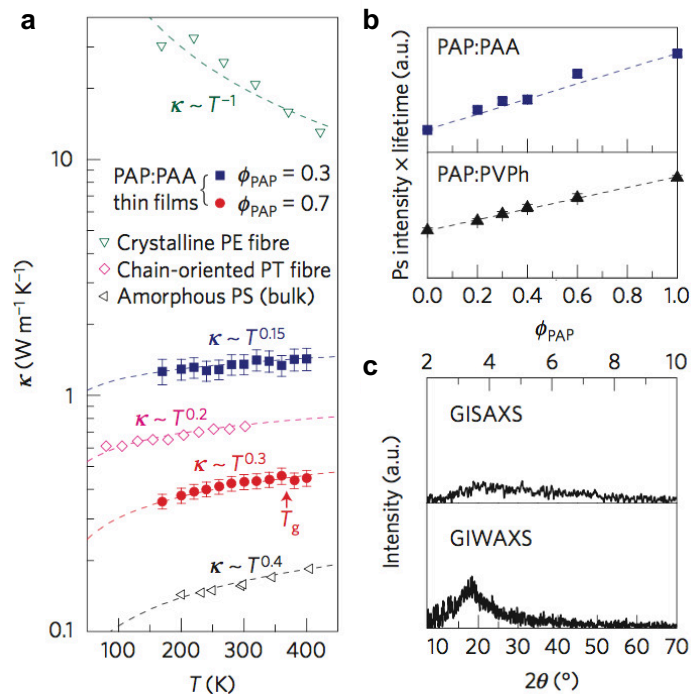
Figure 2.10 | Thermal and structural properties of PAP:PAA. a, $\kappa(T)$ in PAP:PAA at φ_{PAP} =0.3 and 0.7, compared with $\kappa(T)$ in other crystalline (polyethylene (PE)[6]) and amorphous (polythiophene (PT)[5], polystyrene (PS)[41]) polymers. Dashed lines represent T^x. Error bars were estimated based on uncertainties associated with the film thickness, temperature coefficient of electrical resistance for the heater and the heater width. **b**, Positronium annihilation lifetime spectroscopy data for PAP:PAA and PAP:PVPh blends at various φ_{PAP}. The product of positronium (Ps) intensity and lifetime increases monotonically with φ_{PAP} for both blends, indicating a smooth change in density. Error bars were estimated based on the positron beam intensity fluctuation (the size of the error bars is comparable to that of the symbols). Dashed lines are linear fits. **c**, Grazing-incidence small- and wide-angle X-ray scattering (GISAXS, GIWAXS) data for a PAP:PAA spin-cast film at φ_{PAP} = 0.3, suggesting the absence of short- and long-range order, respectively. We note that the broad peak observed in GIWAXS, known as an amorphous halo, is characteristic of amorphous materials.

The amorphous nature of PAP:PAA blends can also be ascertained from the temperature dependence of measured κ as it is known to have different dependencies: T^1 for crystalline and T^x, x>0 for amorphous polymers. As shown in Figure 2.10a, κ in PAP:PAA at φ_{PAP} = 0.3 increases with T, which is consistent with its amorphous character (Figure 2.10c). Note that the crystalline PE fiber data shown in Figure 2.10a exhibit a

strong negative temperature dependence, indicating that the anharmonic scattering of acoustic modes dominates.[6] The small $d\kappa/dT$ for φ_{PAP} = 0.3 relative to that for φ_{PAP} = 0.7 may indicate a lesser contribution of localized vibrational modes[11] as weak VDW bonds are replaced by a homogeneous network of strong H-bonds with lower acoustic contrast relative to the backbone covalent bonds.

To verify the low thermal conductivity in PAP:PVPh blends, we fabricated an additional blend sample by mixing PAP with poly(4-vinylbenzoic acid) (PVBA) which has

a strong H-bond donating carboxylic acid group like PAA but connected to the polymer backbone via a benzene linker. Similar to PAP:PVPh, PAP:PVBA blend films showed miniscule enhancement in thermal conductivity (Figure 2.11). In addition to the factors related to concentration and distribution of H-bonds in PAP:PVPh films, the heavy benzene ring presents a large impedance contrast to vibrational modes

Figure 2.11 | Thermal conductivity of PAP:PVBA blend as a function of φ_{PAP}. Chemical structure of PVBA is also shown. Similar to PAP:PVPh, no appreciable enhancement in κ is observed.

which transfer energy between PAP and PVPh or PVBA. It can also be attributed to the localization[42] of the heat conducting vibrational states in the benzene moiety of PVPh and PVBA.

2.4 Conclusions

In summary, it was shown that large enhancement in thermal conductivity can be achieved through molecular engineering of the inter-chain interactions between two

polymers in a blend. Replacing the weak vdW interactions with strong H-bonds distributed homogeneously and at a concentration higher than the percolation threshold creates a continuous network of thermally conductive pathways. Thermal conductivity was found to be strongly correlated to H-bond concentration (φ_H) and distribution homogeneity (σ_{sd}), as shown in Figure 2.12. We, however, note that this large κ was realized in films up to 70 nm thick.
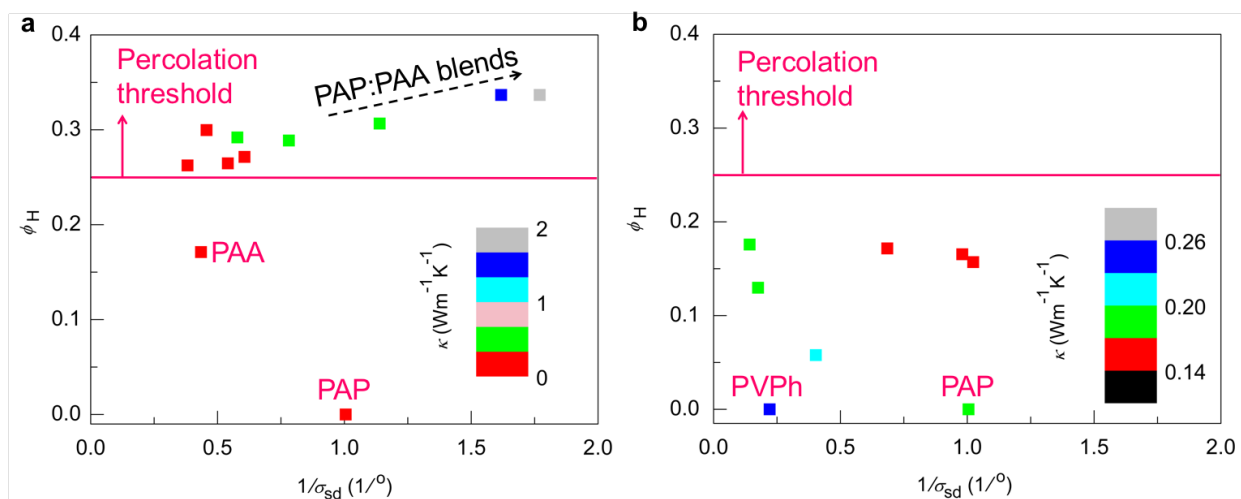
Figure 2.12 | Blend thermal conductivity as a function of concentration and distribution homogeneity of H-bonds. *κ* (color scale) of PAP:PAA **(a)** and PAP:PVPh **(b)** as a function of σ_{sd} and φ_H obtained from AFM phase image and FTIR spectroscopy, respectively, showing the strong dependence of *κ* on bonding homogeneity (that is, $1/\sigma_{sd}$) above the percolation threshold for PAP:PAA. Low φ_H and inhomogeneous distribution of H-bonds (low $1/\sigma_{sd}$) for PAP:PVPh results in inappreciable enhancement of *κ*.

2.5 Author Contributions

G-H.K. conceived the initial ideas with the help of K.P.P., and measured and analyzed the thermal conductivity and AFM data. J.K., D.L. and A.S. designed the polymer systems. D.L., A.S. and G-H.K. prepared the polymer blend films. D.L. and A.S. measured and analyzed FTIR spectroscopy data. L.S. deposited metal patterns and measured film thicknesses. G-H.K., A.S., and M.S.K. measured and analyzed DSC data. D.L. measured GIXS. D.G. measured PALS. J.K. and K.P.P. supervised the work. G-H.K. wrote the manuscript with contributions from all authors, and J.K. and K.P.P. revised the manuscript.

2.6 References

1. M. Chanda, S.K. Roy. *Plastics Technology Handbook* 4th edition (CRC Press/Taylor Francis Group, 2007).

2. Y.P. Mamunya, V.V. Davydenko, P. Pissis, P. E. Lebedev. Electrical and thermal conductivity of polymers filled with metal powders. *Eur. Polym. J.* **38,** 1887–1897 (2002).

3. C.P. Wong, R.S. Bollampally. Thermal conductivity, elastic modulus, and coefficient of thermal expansion of polymer composites filled with ceramic particles for electronic packaging. *J. Appl. Polym. Sci.* **74,** 3396–3403 (1999).

4. S. Shen, A. Henry, J. Tong, R.T. Zheng, G. Chen. Polyethylene nanofibres with very high thermal conductivities. *Nature Nanotech.* **5,** 251–255 (2010).

5. V. Singh *et al.* High thermal conductivity of chain-oriented amorphous polythiophene. *Nature Nanotech.* **9,** 384–390 (2014).

6. X.J. Wang, V. Ho, R.A. Segalman, D.G. Cahill. Thermal conductivity of high-modulus polymer fibers. *Macromol.* **46,** 4937–4943 (2013).

7. K. Kurabayashi, M. Asheghi, M. Touzelbaev, K.E. Goodson, K. E. Measurement of the thermal conductivity anisotropy in polyimide films. *J. Microelectromech. Syst.* **8,** 180–191 (1999).

8. C.L. Choy. Thermal conductivity of polymers. *Polymer* **18,** 984–1004 (1977).

9. P.B. Allen, J.L. Feldman, J. Fabian, F. Wooten. Diffusons, locons and propagons: character of atomic vibrations in amorphous Si. *Phil. Mag. B* **79,** 1715–1731 (1999).

10. W.P. Hsieh *et al.* Testing the minimum thermal conductivity model for amorphous polymers using high pressure. *Phys. Rev. B* **83,** 174205 (2011).

11. S. Shenogin, A. Bodapati, P. Keblinski, A.J.H. McGaughey. Predicting the thermal conductivity of inorganic and polymeric glasses: The role of anharmonicity. *J. Appl. Phys.* **105,** 034906 (2009).

12. K.T. Regner *et al.* Broadband phonon mean free path contributions to thermal conductivity measured using frequency domain thermoreflectance. *Nature Commun.* **4,** 1640 (2013).

13. P.J. O'Brien *et al.* Bonding-induced thermal conductance enhancement at inorganic heterointerfaces using nanomolecular monolayers. *Nature Mater.* **12,** 118–122 (2013).

14. O. Yamamoto, H. Kambe. Thermal conductivity of cross-linked polymers— comparison between measured and calculated thermal conductivities. *Polym. J.* **2,** 623–628 (1971).

15. J.E. Mark. *Physical Properties of Polymers Handbook* (AIP Press, 1996).

16. T. Steiner. The hydrogen bond in the solid state. *Angew. Chem. Int. Ed.* **41,** 48–76 (2002).

17. L.A. Utracki. *Polymer Blends Handbook* (Kluwer Academic Publishers, 2002).

18. Y.S. Jo *et al.* RAFT homo- and copolymerization of N-acryloyl-morpholine, piperidine, and azocane and their self-assembled structures. *Macromol.* **41**, 1140-1150 (2008).

19. Y.K. Koh *et al.* Comparison of the 3 omega method and time-domain thermoreflectance for measurements of the cross-plane thermal conductivity of epitaxial semiconductors. *J. Appl. Phys.* **105**, 054303 (2009).

20. T. Borca-Tasciuc, A.R. Kumar, G. Chen. Data reduction in 3 omega method for thin-film thermal conductivity determination. *Rev. Sci. Instrum.* **72**, 2139-2147 (2001).

21. D.G. Cahill. Thermal-Conductivity Measurement from 30-K to 750-K - the 3-omega method. *Rev. Sci. Instrum.* **61**, 802-808 (1990).

22. A. Richter, R. Guico, J. Wang. Calibrating an ellipsometer using x-ray reflectivity. *Rev. Sci. Instrum.* **72**, 3004-3007 (2001).

23. R.J. Stevens, A.N. Smith, P.M. Norris. Measurement of thermal boundary conductance of a series of metal-dielectric interfaces by the transient thermoreflectance technique. *J. Heat Trans.-T Asme* **127**, 315-322, (2005).

24. J. Liu, S. Ju, Y.F. Ding, R.G. Yang. Size effect on the thermal conductivity of ultrathin polystyrene films. *Appl. Phys. Lett.* **104**, 153110 (2014).

25. C.M. Schilli *et al.* A new double-responsive block copolymer synthesized via RAFT polymerization: Poly(N-isopropylacrylamide)-block-poly(acrylic acid). *Macromol.* **37**, 7861-7866 (2004).

26. T. Shibanuma *et al.* Thermosensitive phase-separation behavior of poly(acrylic acid)-graft-poly(N,N- dimethylacrylamide) aqueous solution. *Macromol.* **33**, 444-450 (2000).

27. S.W. Kuo, F.C. Chang. Studies of miscibility behavior and hydrogen bonding in blends of poly(vinylphenol) and poly(vinylpyrrolidone). *Macromol.* **34**, 5224-5228 (2001).

28. C. Qin, A.T.N. Pires, L.A. Belfiore. Spectroscopic investigations of specific interactions in amorphous polymer polymer blends - poly(vinylphenol) and poly(vinyl methyl ketone). *Macromol.* **24**, 666-670 (1991).

29. S.W Kuo, P.H. Tung, F.C. Chang. Syntheses and the study of strongly hydrogen-bonded poly(vinylphenol- b-vinylpyridine) diblock copolymer through anionic polymerization. *Macromol.* **39**, 9388-9395 (2006).

30. M.R. Landry *et al.* A survey of polyvinylphenol blend miscibility. *J. Appl. Polym. Sci.* **54**, 991-1011 (1994).

31. S.N. Magonov, V. Elings, M.H. Whangbo. Phase imaging and stiffness in tapping-mode atomic force microscopy. *Surf. Sci.* **375**, L385-L391 (1997).

32. P.M. Kosaka *et al.* Atomic force microscopy reveals two phases in single stranded DNA self-assembled monolayers. *Nanoscale* **5**, 7425-7432 (2013).

33. K. Kunal, C.G. Robertson, S. Pawlus, S.F. Hahn, A.P. Sokolov. Role of chemical structure in fragility of polymers: A qualitative picture. *Macromol.* **41,** 7232–7238 (2008).

34. G. Kikugawa, T.G. Desai, P. Keblinski, T. Ohara. Effect of crosslink formation on heat conduction in amorphous polymers. *J. Appl. Phys.* **114,** 034302 (2013).

35. D. Stauffer, A. Aharony. *Introduction to Percolation Theory*, 2nd edition (Taylor & Francis, 1992).

36. P. Podsiadlo *et al.* Ultrastrong and stiff layered polymer nanocomposites. *Science* **318,** 80–83 (2007).

37. M.M. Coleman, P.C. Painter. Hydrogen-bonded polymer blends. *Prog. Polym. Sci.* **20,** 1–59 (1995).

38. A.A. Lin, T.K. Kwei, A. Reiser. On the physical meaning of the Kwei equation for the glass-transition temperature of polymer blends. *Macromol.* **22,** 4112–4119 (1989).

39. W.R. Rong, Z.Y. Fan, Y. Yu, H.S. Bu, M. Wang. Influence of entanglements on glass transition of atactic polystyrene. *J. Polym. Sci. Part B* **43,** 2243–2251 (2005).

40. P.J. Lemstra, L.A. Kleintjens, L. A. *Integration of fundamental polymer science and technology-2* 222–226 (Elsevier Applied Science, 1988).

41. W.M. Underwood, J.R. Taylor. Thermal-conductivity of several plastics determined by an improved line-source apparatus. *Polym. Eng. Sci.* **18,** 556–563 (1978).

42. X. Xie, K. Yang, D. Li, T.-H. Tsai, J. Shin, P.V. Braun, D.G. Cahill. High and low thermal conductivity of amorphous macromolecules. *Phys. Rev. B* **95**, 035406 (2017).

Chapter 3

High Thermal Conductivity in Electrostatically Engineered Amorphous Polymers

3.1 Introduction

Effective thermal management in applications such as batteries, automobile cooling systems and high power density electronic devices where heat accumulation can have deleterious effects is critically important to ensure system performance and reliability, and enhance lifetime. Despite their poor thermal conductivity (κ), various advantages including light weight, low cost and easy processability make polymers the material of choice for several heat intensive applications like electronic chip encapsulation, cellphone casing, LED housing, etc. These existing applications along with emerging technologies such as flexible electronics, for which the requirements on flexibility and light weight simply cannot be met by conventional thermal management materials (metals and ceramics), put greater technological incentives on developing thermally conductive polymers.

Blending with high-κ fillers such as metal or ceramic particles, carbon nanotubes (CNTs), or graphene flakes is the most commonly used method to enhance polymers'

thermal conductivity.[1] However, the large volume fraction of fillers required to achieve appreciable enhancement in κ often leads to undesired optical or electrical properties, increased weight, high cost (e.g., CNT: ~\$1000 kg^{-1} vs. PMMA: ~\$2 kg^{-1}), or loss of the easy processability generally associated with polymers.

In contrast to low κ in bulk samples, constituent individual polymer chains are believed to have very large κ. The thermal conductivity of a single polymer chain, in which the elastic disorder[2] between intra-chain covalent and inter-chain van der Waals bonds is absent, was calculated to be as large as few hundreds of Wm^{-1}K^{-1} (ref. 3). Ultra-drawn crystalline nano-fibers with aligned polymer chains were measured to have κ over 100 Wm^{-1}K^{-1} in the alignment direction.[4] The large thermal conductivities of single or few-chain fibers can be retained in amorphous polymers in the direction of chain orientation[5,6] along which heat propagation occurs predominantly through intra-chain transport. Singh et al. reported a significant increase in κ in amorphous polythiophene fabricated via a nano template-assisted electrochemical method that allows polythiophene chains to be oriented in the vertical direction.[7] Thermal conductivity greater than 2 Wm^{-1}K^{-1} has been similarly reported for covalently grafted poly(3-methyl thiophene) brushes. Covalent grafting led to enhanced chain alignment as well as reduction in energetic and positional disorder in such surface-grafted films.[8] These high thermal conductivities reported in polymers with extended chain conformation stand in contrast to surface-grown polymer brushes[9] and polymer films under high pressure,[10] in which the coiled conformation of polymer chains likely remained and enhancement in κ was found to be relatively moderate. However, these approaches either limit the orientation of chain extension to a certain direction or pose challenges in terms of scaling-up the nanoscale films for practical

applications. Therefore, it's desirable to achieve high κ in both in- and out-of-plane directions in bulk amorphous polymers using common fabrication processes.
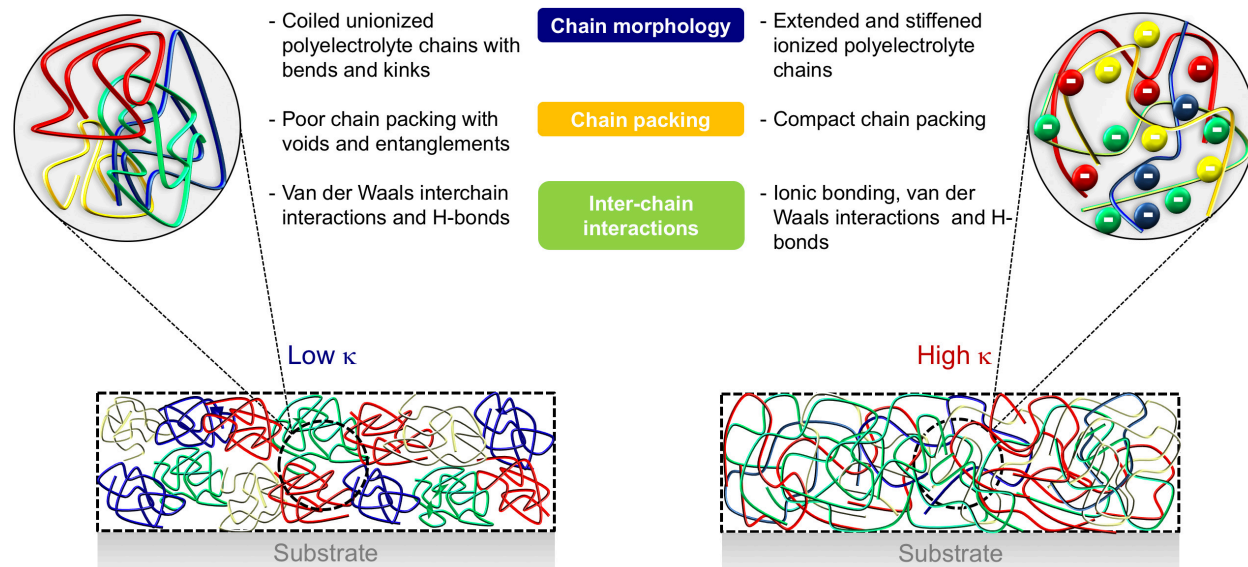
Figure 3.1 | High thermal conductivity in polyelectrolyte thin films via controlled ionization. Illustrations of chain conformation and packing in spin-cast polymer films: coiled unionized polyelectrolyte (*left*) and extended ionized polyelectrolyte (*right*). The zoomed in images show chain confirmation at the molecular level.

While the mechanisms of thermal transport in amorphous materials continue to be studied,[10-13] it is generally believed that the thermal conductivity in bulk amorphous polymers (a class of disordered solids) is inhibited by: a) highly coiled and entangled intra-chain structure, b) loose chain packing with voids that dampen the speed at which vibrations propagate, and c) weak non-bonding inter-chain interactions (e.g., van der Waals, dipole-dipole).[14] In this work, we demonstrate an unexplored molecular engineering route that attack these three bottlenecks simultaneously. By employing the coulombic repulsive forces between ionized pendant groups on the backbone of polyelectrolytes to "stretch" the main chain at the molecular level, we achieve significant

enhancements of thermal conductivity in amorphous polymer with randomly oriented yet superiorly packed extended polymer chains and strong ionic inter-chain interactions (Figure 3.1). Moreover, the favorable conformation change is accomplished in a thermodynamically driven process, making it amenable for scale-up.

3.2 Experimental Section

3.2.1 Chemicals and Materials

Atactic poly(acrylic acid) (PAA, MW 100 kDa and 450 kDa) and atactic poly(*N*-vinyl pyrrolidone) (PVP, MW 40 kDa) were purchased from Sigma Aldrich and were used without further purification. PAA (MW 100 kDa) supplied in the form of 35% aqueous solution was first concentrated at elevated temperature (<100°C) under reduced pressure and then further dried at 60°C under vacuum for 5 days prior to use. Sodium chloride (NaCl) and hydrochloric acid (HCl, 12N) were purchased from EMD Chemicals. Sodium hydroxide (NaOH) was procured from Acros. pH strips for ranges 0-6 and 7-14 with least count of 0.5 pH units and for range 6-7.7 with least count of 0.3 or 0.4 pH units were purchased from Sigma. Silicon wafers with 98 nm of oxide layer for thermal conductivity measurement and Si wafers without oxide layer (native oxide layer thickness ~1.8 nm) for SEM, AFM and XRD analyses were purchased from University Wafers.

3.2.2 Sample Preparation

Polymer Solution and Thin Film Preparation First, the required amount of polymer (PAA or PVP) was dissolved in de-ionized (DI) water by heating at 90°C to ensure complete dissolution. These solutions were then allowed to cool down to room

temperature and the pH was adjusted by adding freshly prepared 1M HCl or 1M NaOH solutions. The solutions were vortexed in between the acid or base additions to allow complete reaction between the base and the polymer (PAA in this case). Finally, the final concentration of solution was adjusted to 0.5 wt.% (PAA) or 1 wt.% (PVP) by adding DI water. The final pH was then measured using the pH strips.

Silicon wafers were cleaned by sequential washing in detergent solution, DI water, acetone and isopropanol by sonicating for 5 minutes each followed by UV-ozone treatment for 20 minutes. The prepared solutions were spin-cast (Laurell Technologies Corporation, Model: WS-650MZ-23NPP/LITE) on pre-cleaned Si substrate at 1500 rpm for 30 seconds. The spin-cast films were then annealed at 100°C for 1 hour. Spin-coating as well as thermal annealing were carried out in a glove box under nitrogen atmosphere. For solvent vapor annealed samples, as-cast PAA films were solvent annealed for 30 minutes under water vapor atmosphere and then annealed at 100°C for 30 minutes. For 3ω measurement, Si wafer with 100 nm SiO_2 layer was used. Si wafer without SiO_2 layer was used for PALS, AFM and SEM analyses. For FTIR, Si substrate coated with Au layer was used. To create the reference region for 3ω measurement, part of the spin-coated film was scratched with a steel blade after which the residual polymer film was removed by a swab soaked in water and ethanol resulting in a clean surface without any polymer residue. Heater lines (5 nm thick Ti adhesion layer + 200 nm Au) were then simultaneously deposited on both sample and reference regions by electron-beam deposition under vacuum. If required, a Al_2O_3 capping layer (to block humidity) was sputter-coated prior to deposition of Au heater lines.

Solvent vapor annealing (SVA) For solvent vapor annealing, the as-made PAA films were kept in an enclosed chamber saturated with water vapor and heated at 90°C for 30 minutes. Post SVA, the samples were removed from the chamber and further annealed on a hot plate at 100°C for 15 minutes, after which all samples are sealed in either a vacuum desiccator or a N_2-filled glovebox.

Blade coating A computer controlled blade-coater from Newmark Systems Inc. (Model MS-1-24) was used to prepare thick film samples. A certain amount of polymer solution (PAA, 450 kDa, 2 wt.%) was dispensed on to the substrate kept on a hot plate at 90°C. The gap between the coating blade and the substrate was then adjusted to get the desired thickness. The blade speed was kept constant at 0.02 mms^{-1} for all the samples. The film thickness is mainly controlled by the gap between the substrate and the blade, and solution concentration. The contact-coated films were very smooth and were annealed at 100°C for 1-2 hours.

Since PAA and its salts are hygroscopic in nature, stringent care was taken during the experiments to avoid exposing the spin-coated and blade-coated samples to atmosphere for any prolonged duration of time. All the samples were stored under nitrogen atmosphere in a glove box prior to any measurement. All the samples were triple-sealed for protection against humidity and usually transported in a desiccator.

3.2.3 Thermal Conductivity Measurement: Differential 3ω Method

3.2.3.1 3ω Set-up and Measurement

A differential 3ω technique was used to measure thermal conductivity of polymer thin films.[15,16] During 3ω measurement, an AC current with frequency ω is applied to

metal heater lines deposited on sample (subscript "s") and reference (subscript "r") regions, inducing a 3ω voltage. Temperature rise (ΔT) in the cross-plane direction is related to $V_{3\omega}$ by[15]:

$$\Delta T = 2\frac{RdT}{dR}\frac{V_\omega}{V_{3\omega}} \tag{1}$$

where dR/RdT is the temperature coefficient of electrical resistance (TCR) for metal heater line and V_ω is voltage applied.

Temperature rises in sample (ΔT_s) and reference regions (ΔT_r) are extracted by measuring voltages that oscillate at frequency ω and 3ω with a lock-in amplifier (SR830 Lock-in Amplifier, Stanford Research Systems), which are then used to calculate the temperature rise across thin film of interest (ΔT_f)[17]:

$$\frac{\Delta T_f}{P_s} = \frac{\Delta T_s}{P_s} - \frac{\Delta T_r}{P_r} \tag{2}$$

where P represents Joule heating power.

Since the width of the heater line (44.7 μm) greatly exceeds the thickness ($t_f < 80$ nm) of spin-cast films, a 1-D heat transfer model based on Fourier's law is sufficient for calculating cross-plane thermal conductivity (κ_z):

$$\kappa_z = P_s\frac{t_f}{wl\cdot\Delta T_f} \tag{3}$$

In the standard sample configuration (Figure 3.2a, center panel), a lithography-fabricated shadow mask with precisely defined geometry (± 1 μm) was attached on a silicon substrate (thickness = 500 μm) with 100 nm thermally-grown SiO_2 for electrical insulation and spin-cast polymer film (on one half of the substrate) for heater line deposition. A 5 nm adhesion layer (Ti) was first deposited via electron beam evaporation (SJ-20 Evaporator, Denton Vacuum) followed by 200 nm of heater line material (Au).

Since PAA is hygroscopic and the absorbed humidity could alter charge density along the backbone as well as disrupt various hydrogen-bonds within the thin film, an alternative sample configuration (Figure 3.2a, right panel) with a 50 nm sputter-coated alumina capping layer (to block humidity) was also used for 3ω measurement. As the alumina capping layer was deposited on the sample and reference regions simultaneously, the temperature rises across it were approximately equal in both regions, making errors caused by the thin Al_2O_3 layer negligible. We note that, in order to minimize sample degradation due to humidity, all PAA samples were kept under vacuum prior to 3ω measurements, and consequently values of κ measured from both configurations are consistent within sample-to-sample variations (Figure 3.2c).

A crucial assumption embedded in Eq. 2 is that the heater lines deposited in the sample and reference regions are identical. This is ensured by simultaneous deposition of closely-placed heater lines (distance ~10 mm) in both regions using shadow masks with precise and consistent dimensions. Four identical heater lines (indexed "1", "2", "3", "4") are deposited on sample and reference regions respectively to facilitate cross-checking (i.e., obtain κ values from different combinations of heater lines in both regions). Good agreements between κ measured from various heater line combinations indicate minuscule variations among heater lines deposited using the same mask (Figure 3.2b).

For spin-cast films, an upper limit of heating frequency (f) equal to 442 Hz was chosen to satisfy the line source approximation adapted in the thermal model. This corresponds to a lower bound of thermal penetration depth (TPD) equal to 120 μm (TPD $= (\alpha_{sub}/2\omega)^{1/2}$, where $\alpha_{sub} = 0.8$ cm^{2}s^{-1} is the thermal diffusivity of the silicon substrate and $\omega = 2\pi f$ (refs. 17,18) that is much greater than heater line half-width ($b = w/2 = 22.3$ μm).

Meanwhile, the lower limit of heating frequency was set at 175 Hz, yielding an upper bound of TPD equal to 191 μm that is well below the substrate thickness (500 μm), validating the 1-dimensionalilty of heat transfer as well as semi-infinite substrate approximation. As for the blade-coated samples with large thicknesses (d_f > 2 μm), a lower range of heating frequencies were selected. A prior work[17] has examined the deviation from 1-D heat transfer due to lateral (in-plane) heat spreading, which can be sizable as d_f becomes comparable to heater line half width. Furthermore, it is possible that shear-force-induced short-range chain ordering in the blade-coating direction (in-plane)[19] gives rise to a higher in-plane thermal conductivity (κ_x) than its cross-plane counterpart (κ_z), amplifying lateral heat spreading.[17] However, using an analytical model developed in Ref. 17, we find the error in κ_z due to lateral heat spreading can be largely mitigated (<1% deviation from κ calculated using a 2-D thermal model) by replacing heater line width with a corrected value of (w + 0.88d_f). In addition, a range of heating frequencies was selected for blade-coated PAA films such that it was low enough to enlarge TPD/d_f and further suppress lateral heat transfer, but at the same time high enough to constrain the TPD (~460 μm for the lowest heating frequency used) within the substrate thickness (Figure 3.2f). As a check for semi-infinite substrate approximation, it is known that parasitic effect due to insufficient TPD appears as a deviation from linearity in ΔT vs. log(ω) (refs. 17, 18), which is not evident in our results (Figures 3.2d, e).
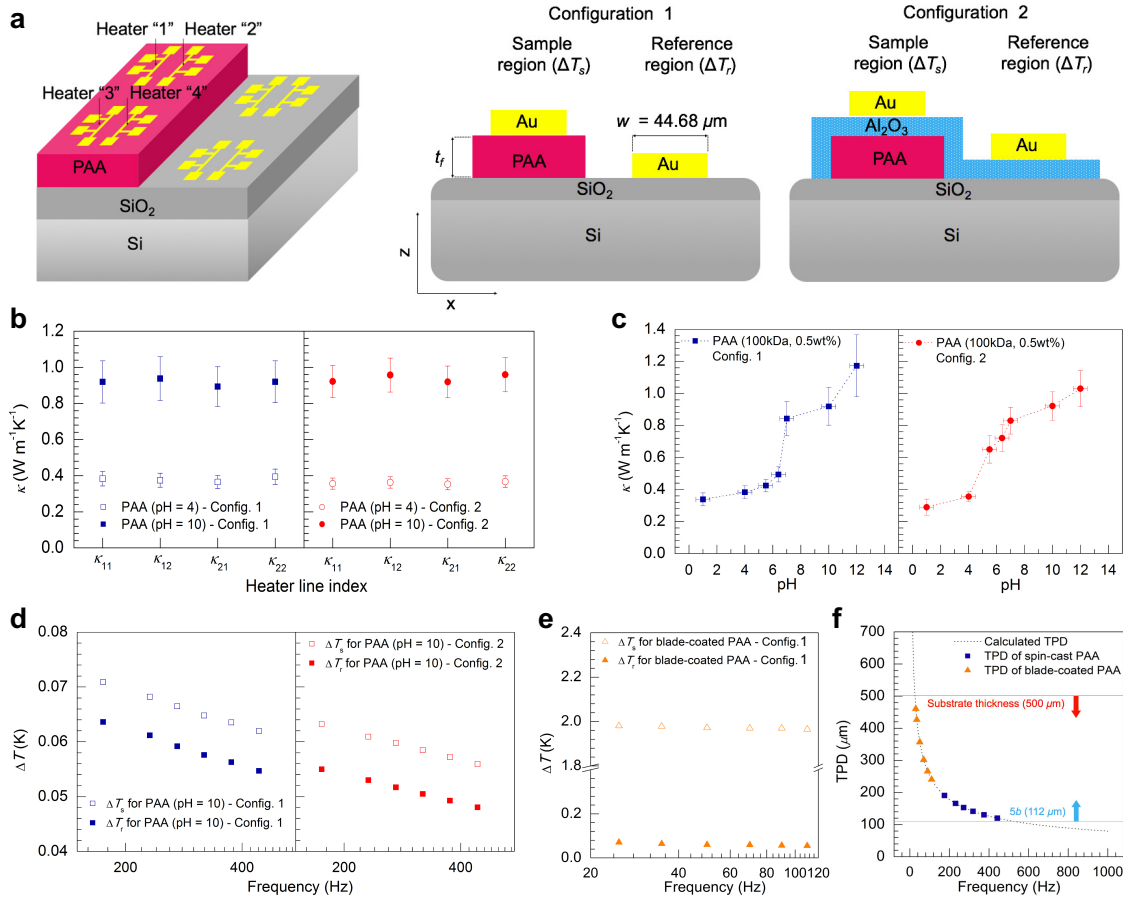
Figure 3.2 | Differential 3ω measurement of thermal conductivity (κ). a, Cross-section (not drawn to scale) of sample geometry showing four identical heater lines (indexed "1", "2", "3", "4") deposited on both the sample and reference regions. Indices are the same for heater lines on both regions. Configuration 2 includes a 50 nm alumina capping layer to block humidity. **b,** κ of pH=4 and 10 samples measured from different combinations of heater lines (for example, "$κ_{11}$" represents κ measured using heater line "1" in both sample and reference regions) using both sample configurations. **c,** Thermal conductivities of PAA as a function of solution pH measured from both configurations, showing good agreement of measured κ. **d and e,** Temperature rise on sample ($ΔT_s$) and reference ($ΔT_r$) regions for spun-cast **(d)** and blade-coated films **(e),** the difference of which is the temperate rise across PAA films ($ΔT_f$). **f,** TPD versus heating frequencies (*f*). Several heating frequencies were chosen such that their corresponding TPDs were greater than 5 times the heater line half-width ($5b$=112 μm) but lower than the substrate thickness (500 *μ*m), validating the semi-infinite substrate and 1-D heat transfer approximations adopted in the thermal model.

We note that in reality potential errors that usually stem from line source and 1-D heat transfer approximations can be largely mitigated by the differential nature of our

experiment. Lastly, to check measurement accuracy, thermal conductivities of spin-cast poly(methyl methacrylate) (PMMA) and PAA (dissolved in DMF) were measured to be 0.21 ± 0.02 Wm^{-1}K^{-1} and 0.35 ± 0.03 Wm^{-1}K^{-1}, respectively, agreeing well with reported values obtained by time-domain thermal reflectance for films of similar thicknesses and produced under identical conditions.[20]

3.2.3.2 Error Analysis

As mentioned above, the accuracy of differential 3ω technique depends primarily on heater lines and substrate conditions being identical in the sample and reference regions. While good agreement between values of κ measured from different heater line combinations indicates measurement robustness, several parameters (w, TCR, d_f and thermal boundary conductance) are subject to experimental uncertainties and their consequential errors are analyzed below.

Heater line width, temperature coefficient of resistance and film thickness Widths (w) of forty heater lines measured by an optical microscope yielded a standard deviation ($\sigma_{SD, w}$) of 0.933%. Since $\sigma_{sd, w}$ affects temperature rises in the sample and reference regions independently, it is magnified by the inverse of signal-to-noise ratio $(\Delta T_s^2 + \Delta T_r^2)^{1/2}/\Delta T_f$ (ref. 18) so that a small variation in w may lead to an enlarged uncertainty in measured κ depending on the magnitude of $(\Delta T_s^2 + \Delta T_r^2)^{1/2}/\Delta T_f$. Therefore, $\sigma_{sd, w} \times (\Delta T_s^2 + \Delta T_r^2)^{1/2}/\Delta T_f$ was used for error calculation. TCRs of forty heater lines were measured previously in a cryogenic setup with a homemade LabVIEW data acquisition program. Since TCR varies for heater lines deposited using different deposition tools, the same e-

beam evaporator has been used for all the experiments. $\sigma_{sd,TCR}$ was found to be small (2.7%) and it is further minimized by the differential nature of our experiment.

Thickness (d_f) of spin-cast PAA films was measured by ellipsometry (Woollam M-2000DI Ellipsometer) and surface profilometry (Dektak XT Surface Profilometer) while d_f of blade-coated films were measured using only the latter due to their greater film roughness. Ellipsometry is ideal for measuring the thicknesses of smooth films, typically yielding a measurement error within 5 Å (ref. 21); assuming a lower bound of d_f equal to 10 nm, we set the thickness error to be 5 % (5 Å/10 nm) for error calculation. During ellipsometry, the laser beam spot was focused on the same region where the heater lines were to be deposited later to ensure d_f and κ were measured in an overlapping region, thereby minimizing errors in κ caused by spatial variation within the film. Thicknesses of twenty PAA samples were cross-checked using Dektak surface profilometer. Prior to profilometry, thin grooves were made by scratching the polymer film with a steel blade (hardness: steel < SiO_2) while keeping the SiO_2 layer intact. Since Dektak stylus radius (12 μm) is smaller than the width of the steel blade (25 μm), it is able to measure the depth of the groove as the stylus sweeps across. Dektak-measured thicknesses (averaged over three positions along the groove) matched well with the ellipsometry-measured values, which is consistent with smooth sample morphology. For blade-coated samples, the thickness was measured in a way that the stylus moved from a point close to the heater line in the sample region to the reference region. The error caused by intrinsic height variation due to this translational movement (which is around 1 cm) was estimated to be 20 nm (ref. 22), which is negligible compared to the film thickness (>2 μm).

Thermal boundary conductance Previous study[23] suggests that thermal boundary conductance (TBC) of polymer-inorganic interface could vary as the polymer film thickness becomes comparable to its radius of gyration, owing to polymer chain re-orientation near the substrate. Conceivably, ionization-induced chain extension could lead to better adhesion between polymer and substrate, thereby enhancing the measured effective thermal conductivities of PAA spin-cast from high pH solutions due to a larger PAA/SiO$_2$ TBC.[24] However, we found the enhancement in TBC, if any, insufficient to account for the measured high thermal conductivities. Assuming an actual PAA (100kDa, pH = 10) thermal conductivity of 0.35 Wm^{-1}K^{-1} and a Ti/SiO$_2$ TBC of 100 MWm^{-2}K^{-1} (ref. 25) in the reference region, a diverging TBC on either side of PAA yielded only a measured κ_{eff} equal to 0.424 Wm^{-1}K^{-1}, significantly lower than the values measured for high pH samples (κ = 0.922 Wm^{-1}K^{-1} for pH 10 sample, see Figure 3.3a).
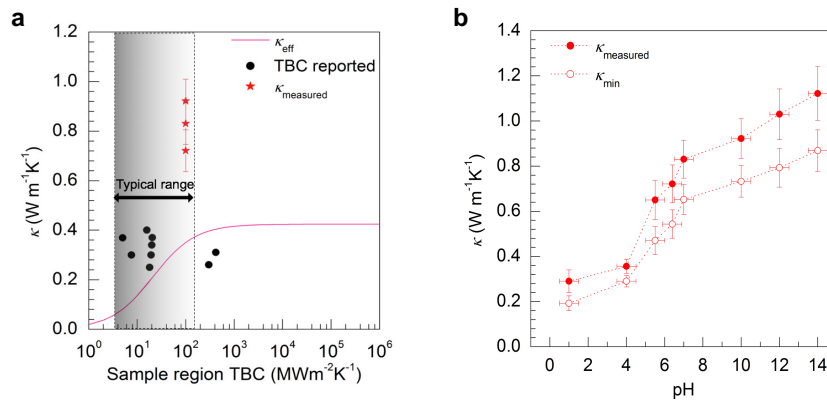
Figure 3.3 | TBC analysis and minimum κ. a, b, $\kappa_{measured}$ (Configuration 2) and κ_{min} versus pH. κ_{min} is the minimum thermal conductivities PAA films need to have in order to fit the measured values, by assuming an infinite TBC in the sample region and a Ti/SiO$_2$ TBC equal to 100 MWm^{-2}K^{-1} in the reference region.

Similarly, as shown in Figure 3.3b, we calculated the minimum PAA conductivities (κ_{min}) required to fit the measured values ($\kappa_{measured}$), assuming again an infinite TBC in the

sample region and a Ti/SiO$_2$ TBC of 100 MWm^{-2}K^{-1} in the reference region. We note that various experimental studies[23,24,26,27] have reported smaller TBC values for inorganic/polymer interface compared to that of metal/ceramic interface (Ti/SiO$_2$ in the reference region, see Figure 3.3a), such that in reality we could very well be underestimating the measured thermal conductivity values. In addition, since errors due to variations in TBC become negligible in thick (>2 μm) blade-coated samples due to large thermal resistance.

3.2.4 Materials Characterization

3.2.4.1 Fourier Transform Infrared (FTIR) Spectroscopy and Quantification of Degree of Ionization

FTIR spectra were recorded on a Nicolet 6700 spectrometer using a grazing angle accessory (Smart SAGA) at a grazing angle of 85$^\mathrm{o}$. 128 scans were recorded for each sample followed by a blank measurement for calibration. Origin 8 software was used to deconvolute the IR spectra; a Gaussian function with 2 or 3 peaks was used to fit the PAA spectra.[28,29] While the baseline was user-defined, peak center, peak width and the area under the curve ($A_{\mathrm{peak\ x}}$, x = 1, 2 or 3 as described below) was calculated by the software. Figure 3.4 shows representative IR spectra with deconvoluted peaks for pH 4, 7 and 12 samples. Peak 1 refers to asymmetric carboxylate (-COO$^-$) stretching band (1556-1594 cm^{-1}), peak 2 (1678-1704 cm^{-1}) refers to self-associated hydrogen bonding carbonyl stretching band of carboxylic acid (-COOH) and peak 3 (1722-1732 cm^{-1}) to non H-bonded carbonyl stretching bands of carboxylic acid. PAA film at pH 1 did not have any ionized groups and thus had no corresponding peak (peak 1) in FTIR spectrum. Films at

pH 1, 4 and 5.5 had both self H-bonded and non H-bonded carboxylic acid groups as evidenced from peak broadening that required two Gaussian peaks to fit. As the degree of ionization increased further, only self H-bonded carboxylic acid groups remained in addition to the ionized groups. The degree of ionization (α) was then calculated as:

$$\alpha = \frac{A_{peak\ 1}}{\left(A_{peak\ 1} + A_{peak\ 2} + A_{peak\ 3}\right)} \times 100\% \qquad (4)$$
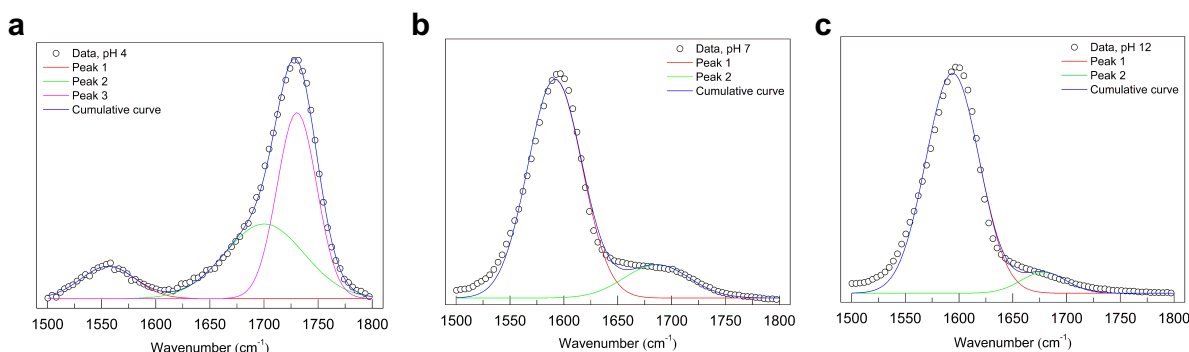
Figure 3.4 | Representative FTIR spectra with deconvoluted peaks. a, FTIR spectrum of pH 4 sample. **b,** FTIR spectrum of pH 7 sample and **c,** FTIR spectrum of pH 12 sample. Peaks were fitted assuming Gaussian distribution. Peak 1 refers to asymmetric carboxylate ($-COO^-$) stretching band (1556-1594 cm^{-1}), peak 2 (1678-1704 cm^{-1}) refers to self-associated hydrogen bonding carbonyl stretching band of carboxylic acid ($-COOH$) and peak 3 (1722-1732 cm^{-1}) to non H-bonded carbonyl stretching bands of carboxylic acid.

3.2.4.2 Viscosity Measurement

Viscosity was measured on a TA Instruments Advantage Rheology G2 instrument using a cone plate configuration with a steel cone of 40 mm diameter and cone angle of 2°. The plate temperature was maintained at 25°C. 2 wt.% solution of PAA (100 kDa) and 8 wt.% solutions of PVP (40 kDa) with adjusted pH was used for viscosity measurement to get more reliable values. Measurements for PAA were done at three shear rates: 120 s^{-1}, 150 s^{-1} and 200 s^{-1} and the viscosity was found to be consistent across shear rates

with the least oscillation at the highest shear rate (reported here). For PVP, measurements were done at two shear rates of 120 s^{-1} and 200 s^{-1} (data shown here). Data was collected at intervals of 5 s for 2 minutes for each shear rate.

3.2.4.3 Positronium Annihilation Lifetime Spectroscopy (PALS)

PAA films were prepared by spin-casting polymer (100 kDa) solutions at different pH on Si wafers without an oxide layer. PALS data[30] was obtained using a focused positron beam having a positron implantation energy of 0.7 keV. Fitting the PALS spectrum yields a positronium intensity, I (%), and lifetime (which is directly related to pore volume, V (nm^3)). The relative change in the product of I and V represents the fractional change in film porosity. The fitted values of I were corrected for positron transmission through the thin film (primarily for films with pH < 6; pH 1 sample film thickness was too small for accurate PALS measurement). Errors in the IV products are estimated from the standard deviations in the fitting of I and V (from lifetime) and the error in the beam transmission correction.

3.2.4.4 Nano-indentation for Elastic Modulus Measurement

Due to the inherent difficulty of measuring modulus for nano-scale spin-cast films, nano-indentation (Hysitron 950 triboindenter) was performed on thick blade-coated samples to quantify the modulus contribution to the measured high κ. The nano-indenter was equipped with a Berkovich probe that had a diamond tip with known geometry, controlled by a piezoelectric transducer with loading force resolution of 1 nN and displacement resolution of 0.02 nm. Prior to measurement, the probe was calibrated

against a fused quartz sample with known elastic modulus. We note that the elastic modulus (11.58 GPa) measured for pH = 1 film is similar to that measured for PAA thin film by picosecond acoustic measurement (E= ~9.86 GPa; E = $2C_{44}(1+ v)$, C_{44} = 3.6 ± 0.1 GPa, v = 0.37).[31] All measurements were performed under a constant Ar gas flow over the sample mounted on the instrument stage and at a constant maximum indentation depth ("displacement") of 400 nm. The samples were annealed at 100°C for 10 minutes right before transferring to the instrument where they were under constant Ar gas flow. This was done to avoid moisture absorption in the PAA films. Elastic modulus was measured on 4 different regions on each sample to yield an average value, with their standard deviation set as the error bar. Model fitting was done for the unloading part of the force-displacement curve (Figure 3.5). Reduced modulus (E_r) was calculated according to the standard Oliver and Pharr method[32]:

$$E_{\mathrm{r}} = \frac{S\sqrt{\pi}}{2\sqrt{A}} \tag{5}$$

where S is the slope of the loading force vs. displacement curve in the upper portion of the unloading data and A is the probe/sample contact area, respectively. We note that due to the viscoelastic nature of PAA films, the fitting was carried out in the 20-80% range of the unloading data to avoid potential errors stemming from sticking of the polymer film to the probe during initial retraction.
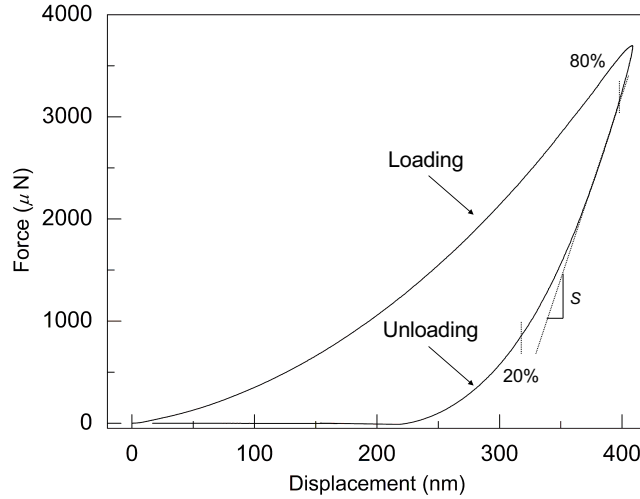
Figure 3.5 | A typical force vs. displacement curve from nano-indentation of a blade-coated PAA film. The unloading curve in the range of 20-80% was used for data fitting of *S*, which was then used to calculate the reduced modulus based on the Oliver and Pharr relation. A consistent maximum displacement equal to 400 nm was chosen for all measurements.

Finally, the actual film modulus was calculated using the following relation[32]:

$$\frac{1-v^2}{E} = \frac{1}{E_r} - \frac{1-v_i{}^2}{E_i} \tag{6}$$

where v, v_i and E_i are the Poisson's ratio of PAA, Poisson's ratio of the diamond tip (0.07) and the elastic modulus of the diamond tip (1140 GPa), respectively. To calculate E using equation 6, $v = 0.37$ was used for pH 1 and 4 samples, and $v = 0.25$ was used for pH 7, 10 and 12 samples.[31]

3.2.4.5 Atomic Force Microscopy

AFM was carried out on a Bruker ICON AFM. Under AFM tapping mode, topography and phase images were recorded to visualize the sample surface morphology and to characterize the spatial variations in surface stiffness,[33] respectively.

3.2.4.6 Scanning Electron Microscopy (SEM) and Focused Ion Beam (FIB)-assisted SEM

SEM was carried out on FEI Nova 200 Nanolab SEM. Bare silicon substrate without thermally grown oxides was used for SEM imaging to facilitate charge dissipation. A relatively small acceleration voltage was used to avoid damaging PAA films, yet at the chosen voltage a few nanometer imaging depths can still be achieved.[34] Focused ion beam (FIB)-assisted SEM was used to image the cross-section of a sample beneath the gold heater line. Focused ion beam (FIB) was used to etch out a 20 μm long and 10 μm deep indentation on a heater line, exposing a sharp cross-section centered around the boundary between sample and reference region. A thin layer of gold was then sputter-coated for imaging.

3.2.4.7 Grazing-incidence X-ray Diffraction (GI-XRD)

GI-XRD measurements were carried out on a Rigaku Ultima IV diffractometer with Cu K_α source (λ = 1.54 Å). To maximize signal from the films, 3 wt.% PAA (100 kDa) solutions were used for preparing the spin-coated films on a Si substrate with 100 nm oxide layer. Incidence angle was set at 0.2^o and data was collected from 5° to 50° at 0.1^o intervals with a dwell time of 4 seconds per data point.

3.2.5 Theoretical Calculations

Theoretical calculation of degree of ionization (α) Degree of ionization (α) was theoretically calculated from the following equation:

$$[H^+] + [Na^+] = [OH^-] + [COO^-] \tag{7}$$

Total number of carboxylic acid groups, [COOH], was calculated from the amount of polymer added in the prepared solution as number of repeating units (monomer MW = 72 Da) ignoring the chain end groups. Concentration of Na^+ ions ($[Na^+]$) was calculated from the known amount of NaOH added in the solution and $[H^+]$ and $[OH^-]$ ions were calculated from the measured pH. Applying charge balance, concentration of carboxylate ions, $[COO^-]$, was obtained. Degree of ionization was then calculated as ratio of carboxylate ions to total carboxylic acid groups, i.e. $[COO^-]/[COOH]$, in the solution.

Theoretical calculation of NaOH volume fraction The theoretical volume fraction of NaOH crystals (V_{NaOH}) was similarly calculated for spin-cast thin films. Since majority of hydroxyl ions are consumed in the acid-base reaction with carboxylic acid groups, OH^- ions instead of Na^+ ions are the limiting species for NaOH crystal formation. With the PAA solution pH and amount of polymer as well as NaOH added known, we calculated the concentration of OH^- ions in the solution based on charge balance. Assuming that ions and polymer chains are retained proportionally in the spin-cast film from the solution and that all left-over OH^- ions form NaOH crystals, we calculated the volume fraction of crystals in the film (V_{NaOH}) using standard values of densities[35] for bulk PAA (V_{PAA} = 1.41 gcm^{-3}) and NaOH (V_{NaOH} = 2.13 gcm^{-3}). We note that this calculation yields an upper bound of V_{NaOH} since more polymer chains are retained in the film during spin-casting compared to the smaller Na^+ and OH^- ions and not all OH^- ions may end up forming NaOH crystals.

3.3 Results and Discussion

To test our idea, we used a weak polyelectrolyte, polyacrylic acid (PAA, atactic), made up of a C-C backbone with a carboxylic acid (-COOH) group at alternate carbon atoms that can be ionized to a carboxylate (-COO⁻) by addition of a base, i.e., with increase of the polymer solution pH. The close proximity of the densely packed ionizable groups to the polymer main chain allows the effect of electrostatic repulsion between them to easily translate to the backbone, resulting in chain extension with increasing ionization. As a negative control, a water soluble polymer, poly(*N*-vinyl pyrrolidone) (PVP, atactic), without an ionizable pendant group, was employed. Cross-plane thermal conductivities of spin-cast polymer films were measured by a differential 3ω method, which is a standard technique for such measurements in films with thicknesses as small as few nanometers.[17,36] As shown in Figure 3.6a, the thermal conductivity of PAA increased from 0.34 ± 0.04 Wm^{-1}K^{-1} at pH 1 when the PAA chains are completely unionized to 1.17 ± 0.19 Wm^{-1}K^{-1} at pH 12 when the PAA chains are predominantly ionized (>90%, *vide infra*). The thermal conductivity of PVP, however, measured ~0.2 Wm^{-1}K^{-1} across the entire pH range, consistent with its non-electrolyte nature.
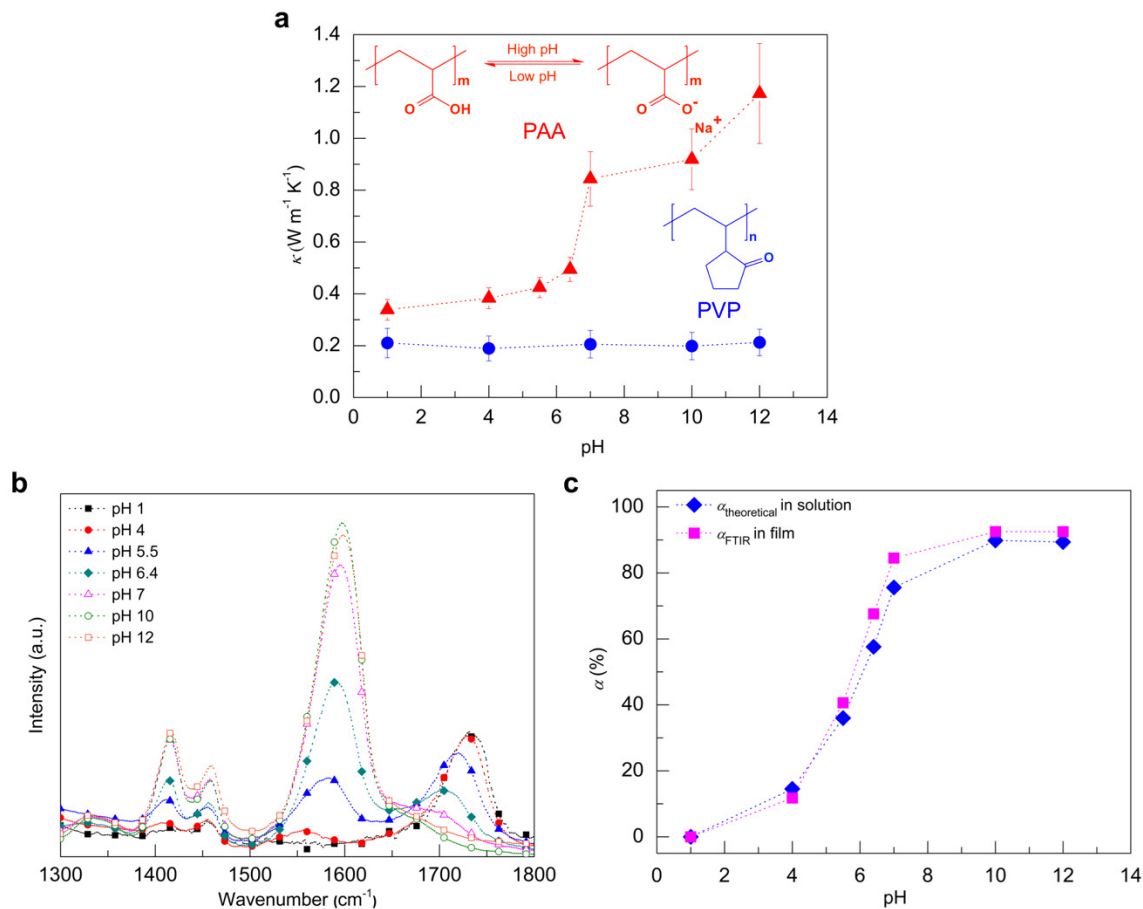
Figure 3.6 | Thermal conductivity of PAA and PVP, and FTIR spectra of PAA as a function of pH. a, Cross-plane thermal conductivity of a weak polyelectrolyte, PAA (MW 100kDa), and a non-ionizable water soluble polymer, PVP (MW 40kDa) thin films spin-cast from polymer solutions of different pH. Error bars were calculated based on uncertainties in film thickness, temperature coefficient of electrical resistance for the heater, and heater width. Chemical structures of the polymers and ionization reaction for PAA are also shown. **b,** Fourier transform infrared (FTIR) spectra of PAA films spin-cast from solution of different pH. **c,** Fraction of ionized carboxylic acid groups (α) as a function of solution pH: calculated from the FTIR spectra and by applying charge balance on PAA solutions.

Fourier transform infrared (FTIR) spectroscopy was used to confirm and quantify the extent of ionization of PAA. Figure 3.6b shows the FTIR spectra of PAA films spin-cast from solutions of different pH. The decrease in intensity of the carbonyl (–C=O) stretching band (1680-1730 cm^{-1}) of the carboxylic acid (-COOH) group with pH and

103

concomitant increase in the intensity of the asymmetric carboxylate (-COO⁻) stretching band (1556-1594 cm⁻¹) indicate ionization of the PAA chains.[28] The degree of ionization (α) of PAA as a function of solution pH (Figure 3.6c), calculated from the areal ratio of peaks corresponding to ionized and unionized acidic groups fitted assuming Gaussian distributions and the same extinction coefficient for the two bands[29] matches with previously reported trends.[28] A theoretical charge balance calculation for the PAA solution yielded similar values for α confirming that PAA retains its ionization in the thin film state. In contrast, FTIR spectra did not show any change in chemical signature with pH for PVP (Figure 3.8a).

We further measured viscosities of PAA solutions at different pH, and porosities and elastic moduli of PAA thin films fabricated from solutions at different pH to quantify the three ionization-induced effects, viz., polymer chain extension,[37] chain packing,[37] and chain stiffening,[38] respectively. As shown in Figure 3.7a, the relative viscosity, η_r (= $\eta_{polymer}$ / η_{water}, η_{water} = 10^{-3} Pa.s), increases with solution pH, indicating that coulombic repulsion between ionized carboxylic acid groups stretches out the PAA chains, resulting in an extended morphology and hence increased solution viscosity.[39] Under the same spin-casting conditions, the trend in film thickness (d_f) matches well with that of solution viscosity, suggesting that the extended conformations of PAA chains in solution are likely preserved in the thin films. We note that it is likely that upon spin-cast the sodium ions condense close to the negatively-charged pendant groups of PAA to maintain charge neutrality, reducing the degree of chain extension due to charge screening. However, a previous AFM study on spin-cast samples of a brush polymer with grafted PAA side chains demonstrated systematic extension in chain morphology as pH increased,[40]

corroborating our assertion that at least some level of chain extension has been preserved in the solid-state films. The viscosities of PVP solutions as well as the film thicknesses for spin-cast PVP samples remained unchanged across the pH range as expected (Figure 3.8b).
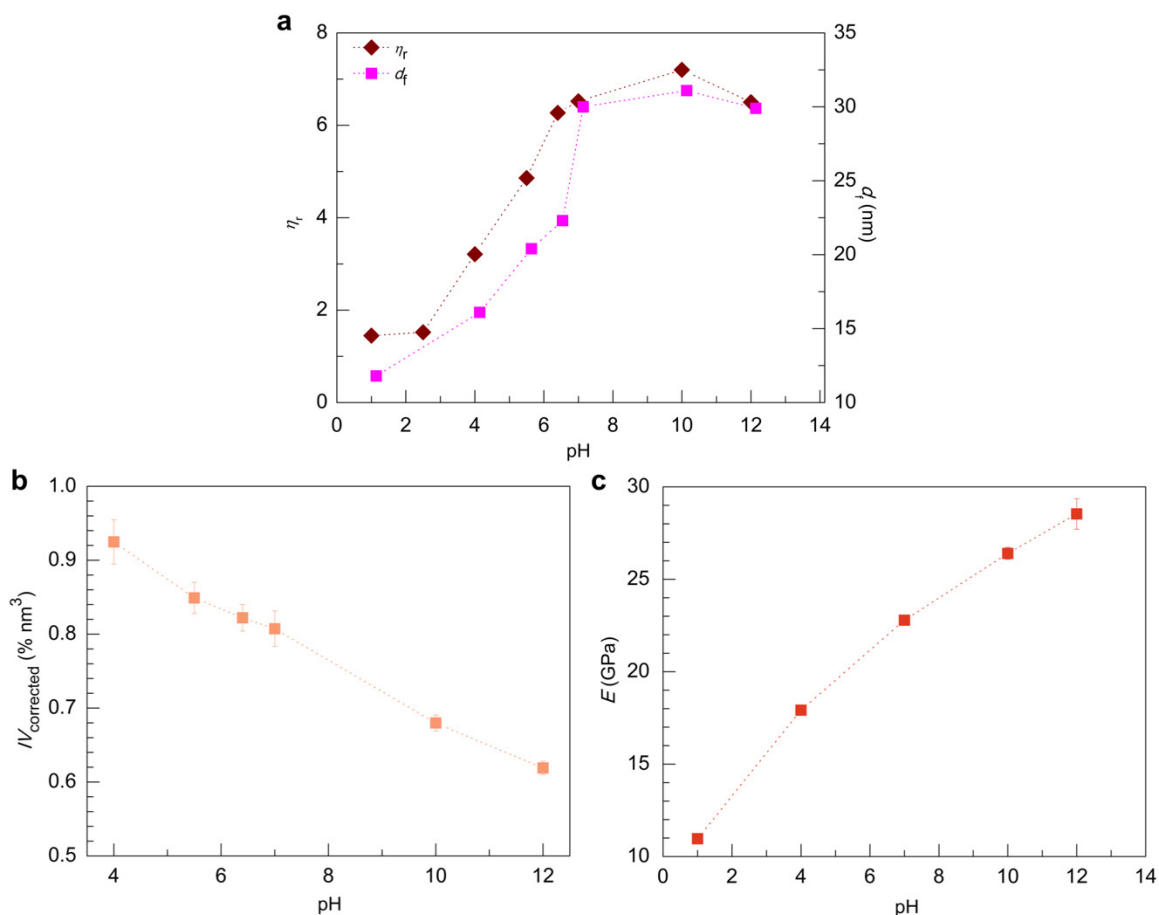
Figure 3.7 | Effects of PAA ionization. **a,** Relative viscosity, η_r (= $\eta_{polymer}/\eta_{water}$, η_{water} = 10^{-3} Pa.s), of a 2 wt.% solution of PAA, and film thickness, d_f, of spin-cast samples (from 0.5wt.% solution) as a function of pH. **b,** Positronium annihilation lifetime spectroscopy data for PAA films at different pH. The change in the product of positronium (Ps) intensity (I, %) and pore volume (V, in nm^3) represents the change in film porosity. Error bars were estimated based on the errors from fitting I and V plus an estimate of the error in the positron transmission correction. **c,** Elastic modulus of blade-coated PAA (MW 450kDa) films measured by nano-indentation. The error bar shows standard deviation of measurements at four different points on the film.

Since polymer density in confined films is known to differ from the bulk value and depends on the film thickness,[41] it was necessary to assess the change in density of PAA films with pH. Positronium annihilation lifetime spectroscopy (PALS)[30] was used to measure porosity of spin-cast PAA films. PALS data (Figure 3.7b) shows a linear decrease in PAA film porosity with pH, which can be explained by better chain packing in the spin-cast thin films afforded by extended ionized chains. The measured ~33% drop in film porosity from pH 4 to pH 12 is consistent with the previously measured trend in bulk density of partially ionized PAA.[35] Due to the inherent difficulty of performing nano-indentation[32] on nano-scale spin-cast films, micrometer-thick blade-coated PAA (MW 450 kDa, atactic) films[19] were used for elastic modulus (E) measurement. As shown in Figure 3.7c, elastic modulus increased with pH, i.e., with ionization of PAA chains. A similar chain stiffening effect caused by reduced chain segmental mobility due to strong ionic interactions between the negatively charged polymer chains and the surrounding positive cationic coordination sphere[42] is generally attributed for the large increase in glass transition temperature (T_g) of PAA with ionization.[43]
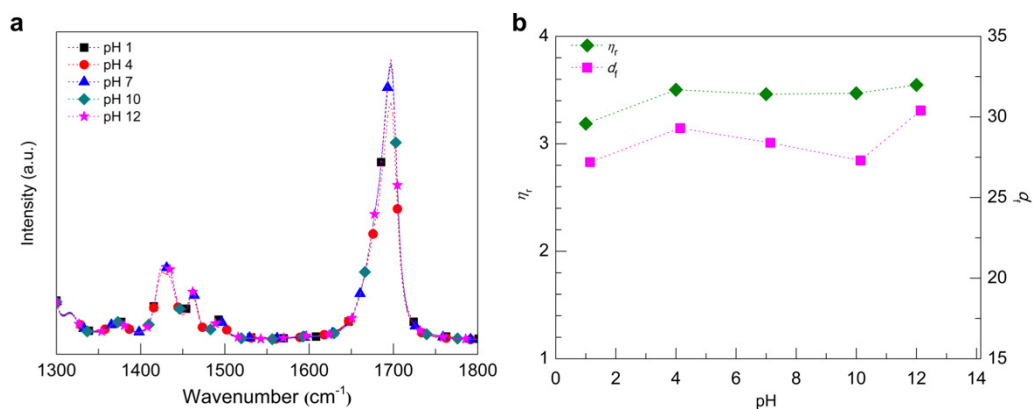
Figure 3.8 | Characterization of PVP films and solutions. a, FTIR spectra of spin-cast PVP films as a function of pH. **b,** Relative viscosities of 8 wt.% aqueous solutions of PVP and film thicknesses for the spin-cast samples shown in Fig. 3.6a.

Furthermore, grazing-incidence x-ray diffraction measurements carried out on spin-cast PAA films did not show any sign of polymer crystallinity (Figure 3.9) thereby ruling out any crystallinity-related contribution to the measured thermal conductivity. We note that the broad diffused peak, known as amorphous halo, seen for all samples is characteristic of amorphous polymers including PAA[44] and PAA salts.[45]
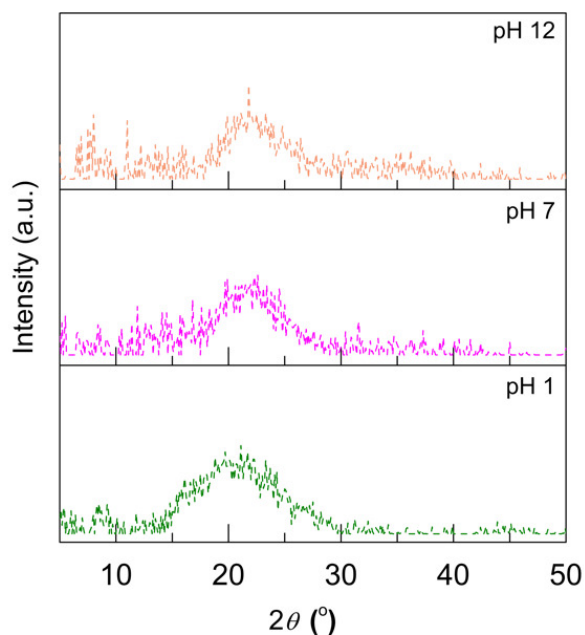
Figure 3.9 | Grazing-incidence x-ray diffraction spectra of PAA films at different pH. The broad diffused peak from ~15°-30°, called amorphous halo, is characteristic of amorphous polymers.

In order to rule out the possible contributions of NaOH crystals that could potentially act as high-κ fillers to measured thermal conductivity, we calculated the maximum possible volume fraction of NaOH crystals (V_{NaOH}) in the resulting polymer films. Such NaOH crystals formed from residual Na^+ and OH^- ions in the polymer solution could act as high-κ fillers and contribute to thermal conductivity enhancement. However,

based on the known amount of PAA and NaOH added in the polymer solutions at various pH, the calculated V_{NaOH} was found to be negligible (V_{NaOH} ~1.65% for the highest pH 12 sample) except for an additional sample (not shown in the data of Figures 3.6a and Figure 3.7) for which excess NaOH was added specifically to probe the potential contribution of NaOH crystals (shown in Figures 3.10a and 3.10b). While crystals were not observed in the samples except for the one with excess NaOH, a Maxwell model was nevertheless used to predict the thermal conductivities that would be expected if the NaOH crystals were homogeneously distributed within the film as nano-sized spherical fillers,[46] for comparison with values measured for chain-extended PAA films. A volumetric percolation threshold equal to 25% is required for appreciable κ enhancement in such composites; this is not reached even for the highest pH PAA film (pH 12; V_{NaOH} = 1.65%). The fact that the measured PAA thermal conductivities are significantly greater than Maxwell-predicted values (Figure 3.10e) indicates that κ enhancement due to ionization-induced effects dominates over the possible contributions of high-κ fillers over the range of pH selected.

Tapping-mode atomic force microscopy (AFM) and scanning electron microscopy (SEM) analyses of the PAA films further corroborate the theoretical calculation of V_{NaOH}. As can be seen in Figure 3.10a, AFM topography images show a smooth featureless film surface morphology for values of pH up to 12. Small spherical NaOH crystals can be seen in the thin film spin-cast from polymer solution with excess NaOH added. The standard deviation in AFM phase image (σ_{SDEV}) is small and shows no systematic trend as a function of pH, indicating compositional homogeneity (Figure 3.10c). The mean phase shift (φ_{mean}) as a function of pH is shown in Figure 3.10d. The pH 12 sample has a significantly more positive phase shift, indicating a stiffened chain likely due to the

presence of excessive Na$^+$ ions. SEM images were used to confirm surface morphology as well as investigate the potential presence of NaOH crystals buried within the film (Figure 3.10b). We did not observe any sign of NaOH crystals except for the sample with excess NaOH added, which is consistent with the AFM topography images.
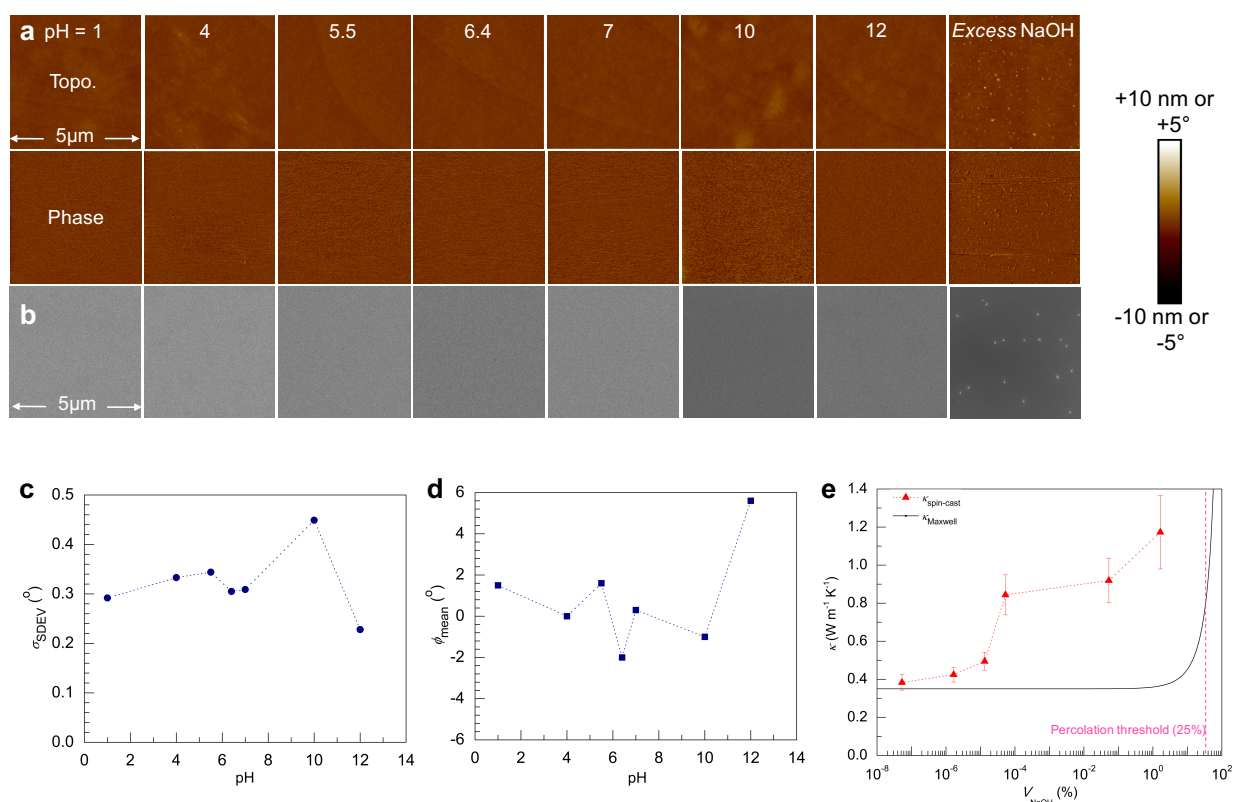
Figure 3.10 | Tapping-mode AFM and SEM analyses of PAA films. a, Tapping-mode topography (top) and phase (bottom) images (5 μm x 5 μm) of PAA films spin-cast from solutions of different pH. AFM images have been shifted to zero mean values (i.e." flattened") for illustration purposes. Nano-sized NaOH crystals are only visible in sample with excess amount of NaOH added to the PAA solution. **b,** SEM images (5 μm x 5 μm) of the same films analyzed by AFM. NaOH crystals can be seen only when excess NaOH is added, consistent with the AFM data. **c,** Standard deviation in AFM phase image for spin-cast PAA films. σ_{SDEV} is small and shows no systematic trend as a function of pH, indicating high level of film homogeneity over the entire pH range. **d,** Mean phase shift (prior to flattening) of spin-cast PAA films. The greater φ_{mean} found in the pH 12 sample may come from excessive Na$^+$ ions causing stiffening of the polymer chains. **e,** Measured thermal conductivities, $\kappa_{spin-cast}$, for spin-cast films greatly exceeds the Maxwell-model predicted values, indicating enhancement is not primarily due to a high-κ filler effect.

To investigate whether preferential crystallization of NaOH occurs in the polymer film beneath the gold heater lines (i.e., metal-polymer interface) due to heterogeneous nucleation,[47] FIB-assisted SEM was used to image the cross-section of a pH 10 sample beneath the gold heater line. From Figure 3.11 (right panel), small grains (~10 nm) of the Pt layer are clearly observed, indicating a SEM resolution that is sufficient to characterize features on similar length scale. No sign of NaOH crystals buried underneath the gold heart line was observed thereby ruling out the possibility of preferential crystallization of NaOH due to heterogeneous nucleation[47] at the metal-polymer interface.
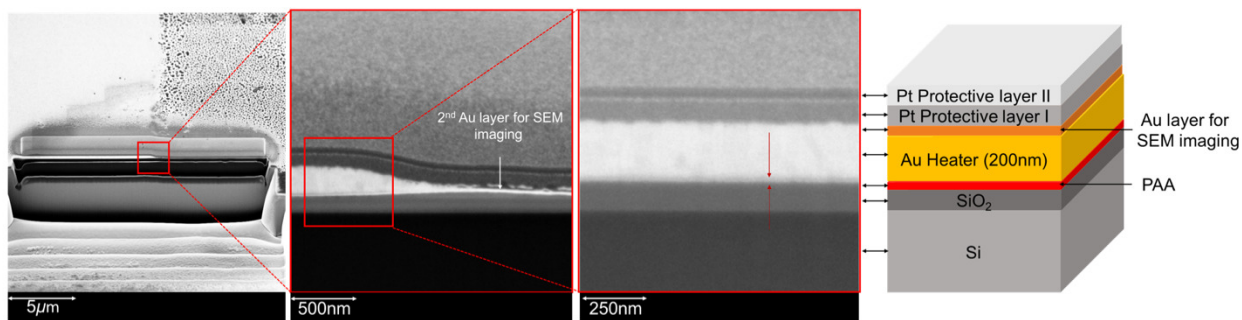
Figure 3.11 | Cross-section view of a pH 10 PAA film under the Au heater lines. Focused ion beams (FIB) were used to etch an indentation on a heater line at the edge of sample and reference region (left panel). Polymer film, Au heater line, deposited Au layer for SEM imaging and protective Pt layers can be seen in the cross-sectional view (center panel). Zoomed in image of the sample cross-section doesn't show any embedded NaOH crystals in the film (marked by red arrows) beneath the Au heater lines (right panel).

To deconvolute the contributions to measured κ from the three ionization induced effects, we employed the minimum thermal conductivity model (MTCM)[10,20,31] which describes thermal transport in amorphous and highly disordered materials. According to this model, κ scales with atomic density (ρ_{atom}) as $\rho_{atom}^{1/6}$, which was approximated with

mass density (ρ) here, and linearly with sound velocity which further depends on elastic modulus as $E^{1/2}$. Since the film density cannot be directly calculated from the PALS data, we interpolated densities at different degrees of ionization based on the bulk densities reported in ref. 35. Assuming that film density scales linearly with bulk density, a ~20% higher bulk density at pH 12 (α = 92.5%) compared to pH 1 (α = 0%) suggests a relatively small (~3%) density-related contribution to the enhanced κ. The modulus-related contribution to the measured κ was calculated to be ~61%. Based only on density- and modulus-related contributions to κ, the thermal conductivity at pH 12 is predicted to be ~0.56 $Wm^{-1}K^{-1}$, a ~65% enhancement in κ over that of pH 1 (κ = 0.34 $Wm^{-1}K^{-1}$) that is substantially smaller than the ~250% enhancement measured. Figure 3.12a shows the various contributions to measured κ for each pH calculated by taking κ for pH 1 as the baseline. We note that the measured value (κ = 0.38±0.04 $Wm^{-1}K^{-1}$) for pH 4 sample is lower than the MTCM-calculated value (0.43 $Wm^{-1}K^{-1}$). Clearly, the MTCM, which is based on vibrational states that are neither fully localized nor propagating (diffusons), doesn't entirely capture the enhancement in κ measured in this system. We speculate that the extended and stiffened PAA chains may result in increased diffusion lengths for diffusons. Since long-range propagating modes have been previously shown to exist in disordered solids like amorphous Si,[13,48] it is also possible that a small population of "propagons" exist in the chain-extended PAA. However, further studies are necessary to understand the detailed heat transport mechanisms in these extended systems. We note that a prior work[31] has examined the thermal conductivity of ionically-crosslinked polymer salt with κ reaching 0.67 $Wm^{-1}K^{-1}$. We attribute the additional κ enhancements shown in this study to the added chain extension effect in NaOH-treated PAA, which gives rise to

a greater persistence length and larger effective rigidity of the polymer chains.[38] It is likely that the predominant vibrational transfer of heat along the covalently bonded polymer backbone afforded by the extended and stiffened chain morphology as well as enhanced interchain conductance due to stronger ionic bonds result in the substantial increment in κ. The measured increases in κ are consistent with a recent computational study that predicts large enhancements in κ with increasing persistence length in amorphous polyethylene.[49]
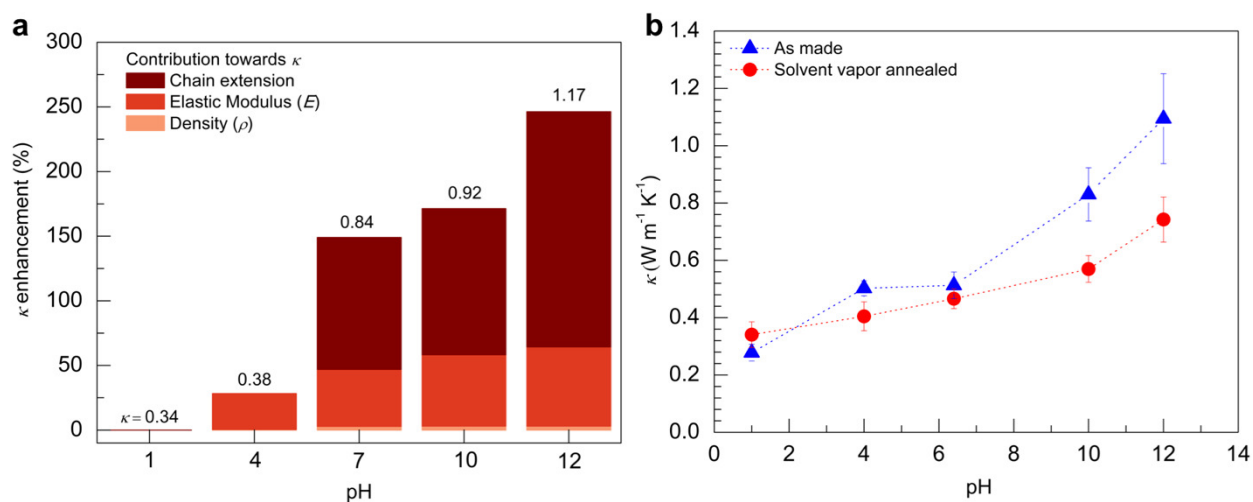
Figure 3.12 | Contributions of ionization-induced effects on PAA κ. a, Contributions from ionization effects shown in a-c towards enhancement in thermal conductivity of spin-cast PAA films. κ at different pH is noted above the bars. **b,** Thermal conductivities of solvent vapor-annealed PAA films compared to those of as-made samples. PAA films were solvent-vapor annealed at 90°C for 30 minutes followed by annealing at 100°C for 15 minutes.

To further confirm the contributions of extended chain morphology of the ionized PAA chains to measured thermal conductivity, we performed solvent vapor annealing (SVA) on spin-cast PAA films. SVA is a commonly used technique to control the morphology of polymer chains in films.[50,51] During SVA, the polymer film absorbs solvent vapor which imparts increased degree of mobility to the polymer chains causing them to

equilibrate to a thermodynamically more favorable coiled conformation. As shown in Figure 3.12b, the differences in thermal conductivity between "as-made" and "solvent-annealed" samples are within experimental uncertainties for low pH samples, indicating that any disruption of ionic and H-bond interactions due to solvent annealing doesn't change κ significantly. However, for pH 10 and 12 samples much lower thermal conductivities were measured for solvent-annealed samples, which can be explained by the coiling up (relaxation) of PAA chains during the solvent-annealing process. At pH 12 specifically, thermal conductivity dropped by as much as ~32%. This signifies that kinetically frozen extended PAA chains are partially responsible for high thermal conductivities measured in the spin-cast films.

We further compared the thermal conductivities of chain-extended PAA films with those of two types of composite films, PAA/NaCl and PVP/NaOH, composed of mutually unreactive polymer-salt mixtures. We assume that the salt added in these samples is proportionally retained in the thin film upon spin-casting from the polymer-salt solution and acts as a high-κ filler. As shown in Figure 3.13a, salt fillers have miniscule effect on composite thermal conductivities till ~20% filler volume fraction. This signifies that extended chain morphology may be more effective at transferring heat than composite strategies, where large thermal resistances may exist at filler-filler and filler-polymer interfaces.
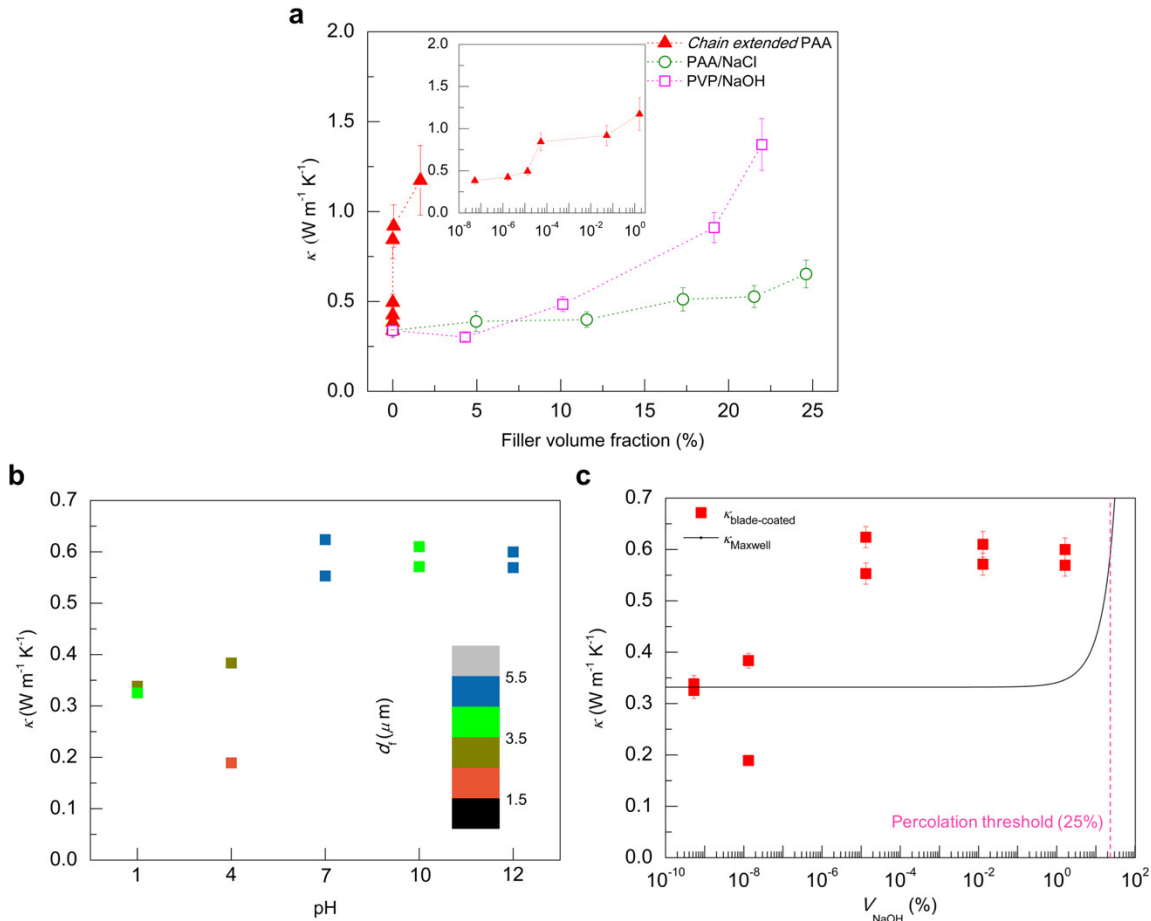
Figure 3.13 | Comparison of thermal conductivities of chain extended PAA and polymer-salt composites. a, Thermal conductivity of thin films of water soluble polymers with added inorganic salts. Chain extended PAA refers to PAA films spin-cast from solutions at different pH. Salts added in PAA/NaCl and PVP/NaOH samples do not react with respective polymers and act as high-κ fillers. The inset shows data for chain-extended PAA with abscissa on log scale. **b,** Thermal conductivity of thick PAA films blade-coated from solutions at different pH. The color map shows film thickness in micrometers. The error in κ was less than 4% for all samples and has not been shown. **c,** Measured thermal conductivities, $\kappa_{\text{blade-coated}}$, for blade-coated films greatly exceed the Maxwell-model predicted values, indicating enhancement is not primarily due to a high-κ filler effect.

As a demonstration of the applicability and potential for scale-up of chain-extended PAA, we fabricated ~1.5-5.5 μm thick PAA (MW ~450 kDa, atactic) films by blade-coating,[19] which is a method representative of large-scale roll-to-roll processing. The average κ measured for chain-extended samples (pH 7-12) was ~0.59 Wm^{-1}K^{-1}, which is

nearly 80% enhancement over the average κ (~0.33 Wm^{-1}K^{-1}) measured for the coiled-chain pH 1 samples (Figure 3.13b). The lower κ in the blade-coated samples likely results from the thermodynamic nature of the blade-coating method. While spin-casting freezes the polymer chains in a thermodynamically high energy state upon rapid solvent evaporation, slow evaporation during blade-coating allows the chains to relax into a more thermodynamically favorable coiled-up morphology, which is consistent with the decline in κ observed for the spin-cast films subjected to solvent vapor annealing. The highest κ (0.62 ± 0.02 Wm^{-1}K^{-1}) measured among the thick films is more than 50% larger than the κ (~0.4 Wm^{-1}K^{-1}) achieved in un-stretched ultra-high MW semi-crystalline (crystallinity ~15%) polyethylene (UHMWPE) films of comparable thickness.[52] The maximum value of V_{NaOH} in such films was calculated to be only 1.64% (corresponding to pH 12). The measured thermal conductivities for these films at high pH (i.e., pH > 7) significantly exceed the Maxwell-predicted values (Figure 3.13c) ruling out any contribution to κ from NaOH crystals. Although directional shear force during blade-coating can potentially lead to some short-range ordering parallel to the substrate within the polymer films as has been previously reported for atactic PAA,[53,54] any such ordering in the in-plane direction would likely cause the in-plane κ (κ_x) to be even greater than the measured cross-plane κ (κ_z). We also note that no such short-range ordering is deemed possible in the spin-cast films due to the kinetic nature of film formation.

3.4 Conclusions

In summary, we have employed electrostatic repulsive forces to stretch the polyelectrolyte backbone at the molecular level, resulting in extended conformations,

better packed chains and enhanced modulus, all of which contribute to significantly enhanced thermal conductivities. For the spin-cast thin films, it is to be noted that centrifugal forces during spin-casting may cause polymer chains to be more expanded in the in-plane direction, possibly making in-plane thermal conductivity even greater than the measured cross-plane κ (ref. 6). This unexplored route for molecular engineering of polymer thermal conductivity is also extended to making micron-thick blade-coated films, with thermal conductivity reaching over 0.6 $Wm^{-1}K^{-1}$.

3.5 Author Contributions

Apoorv Shanker*, Chen Li*, Gun-Ho Kim, David Gidley, Kevin P. Pipe, Jinsang Kim. High thermal conductivity in electrostatically engineered amorphous polymers. *Science Advances.* (*Under revision; *equal contribution)*

A.S. conceived the initial ideas and designed the experiments with the help of J.K. A.S. prepared the polymer thin film samples for thermal conductivity measurements with the help of C.L. and G.-H.K. A.S. and G.-H.K. confirmed the initial hypothesis. A.S. prepared samples for, measured and analyzed FTIR, viscosity, nano-indentation and GI-XRD data. C.L. measured and analyzed thermal conductivity with initial help from G.-H.K., and did SEM, AFM, and FIB-SEM. A.S. and C.L. prepared blade-coated films for thermal conductivity measurements. D.G. measured PALS. K.P.P. and J.K. supervised the work. A.S. wrote the manuscript with contributions from C.L., and K.P.P. and J.K. revised the manuscript. All authors provided feedback on the manuscript.

3.6 References

1. H. Chen, V.V. Ginzberg, J. Yang, Y. Yang, W. Liu, Y. Huang, L. Du, B. Chen. Thermal conductivity of polymer-based composites: fundamentals and applications. *Prog. Polym. Sci.* **59**, 41-85 (2016).

2. S. Gelin, H. Tanaka, A. Lemaitre. Anomalous phonon scattering and elastic correlations in amorphous solids. *Nature Mater.* **15**, 1177-1181 (2016).

3. A. Henry, G. Chen. High thermal conductivity of single polyethylene chains using molecular dynamics simulation. *Phys. Rev. Lett.* **101**, 235502 (2008).

4. S. Shen, A. Henry, J. Tong, R.T. Zheng, G. Chen. Polyethylene nanofibers with high thermal conductivities. *Nature Nanotech.* **5**, 251-255 (2010).

5. C.L. Choy. Thermal conductivity of polymers. *Polymer* **18**, 984-1004 (1977).

6. K. Kurabayashi, M. Asheghi, M. Touzelbaev, K.E. Goodson. Measurement of the thermal conductivity anisotropy in polyimide films. *J. Microelectromech. Sys.* **8**, 180-191, (1999).

7. V. Singh, T.L. Bougher, A. Weathers, Y. Cai, K. Bi, M.T. Pettes, S.A. McMenamin, W. Lv, D.P. Resler, T.R. Gattuso, D.H. Altman, K.H. Sandhage, L. Shi, A. Henry, B.A. Cola. High thermal conductivity of chain-oriented amorphous polythiophene. *Nature Nanotech.* **9**, 384-390 (2014).

8. A. Roy, T.L. Bougher, R. Geng, Y. Ke, J. Locklin, B.A. Cola. Thermal conductivity of poly(3-methylthiophene) brushes. *ACS Appl. Mater. Interfaces* **8**, 25578-25585 (2016).

9. M.D. Losego, L. Moh, K.A. Arpin, D.G. Cahill, P.V. Braun. Interfacial thermal conductance in spun-cast polymer films and polymer brushes. *Appl. Phys. Lett.* **97**, 011908 (2010).

10. W.P. Hsieh, M.D. Losego, P.V. Braun, S. Shenogin, P. Keblinski, D.G. Cahill. Testing the minimum thermal conductivity model for amorphous polymers using high pressure. *Phys. Rev. B* **83**, 174205 (2011).

11. P.B. Allen, J.L. Feldman, J. Fabian, F. Wooten. Diffusons, locons and propagons: character of atomic vibrations in amorphous Si. *Philos. Mag. B* **79**, 1715-1731 (1999).

12. S. Shenogin, A. Bodapati, P. Keblinski, A.J.H. McGaughey. Predicting the thermal conductivity of inorganic and polymeric glasses: The role of anharmonicity. *J. Appl. Phys.* **105,** 034906 (2009).

13. K.T. Regner, D.P. Sellan, S. Zonghui, C.H. Amon, A.J.H. McGaughey, A.J. Malen. Broadband phonon mean free path contributions to thermal conductivity measured using frequency domain thermoreflectance. *Nature Commun.* **4**, 1640 (2013).

14. A. Henry. Thermal Transport in Polymers, *Annual review of heat transfer*, Vol. 17, Chapter 13, 485-520 (2013).

15. D.G. Cahill. Thermal conductivity measurement from 30K to 750K: the 3-omega method. *Rev. Sci. Instrum.* **61**, 802-808, (1990).

16. T. Borca-Tasciuc, D. Song, J. L. Liu, G. Chen, K. L. Wang, X. Sun, M. S. Dresselhaus, T. Radetic, and R. Gronsky. Anisotropic thermal conductivity of a Si/Ge superlattice. *Mat. Res. Soc. Symp. Proc.* **545**, 473, (1998).

17. T. Borca-Tasciuc, A.R. Kumar, G. Chen. Data reduction in 3 omega method for thin-film thermal conductivity determination. *Rev. Sci. Instrum.* **72**, 2139-2147 (2001).

18. Y.K. Koh, S. L. Singer, W. Kim, J. M. O. Zide, H. Lu, D. G. Cahill, A. Majumdar, A. C. Gossard. Comparison of the 3 omega method and time-domain thermoreflectance for measurements of the cross-plane thermal conductivity of epitaxial semiconductors. *J. Appl. Phys.* **105**, 054303, (2009).

19. B. Kim, E.J. Jeong, J.W. Chung, S. Seo, B. Koo, J. Kim. A molecular design principle of lyotropic liquid-crystalline conjugated polymers with directed alignment capability for plastic electronics. *Nature Mater.* **12**, 659-664 (2013).

20. X. Xie, D. Li, T.-H. Tsai, J. Liu, P.V. Braun, D.G. Cahill. Thermal conductivity, heat capacity, and elastic constants of water soluble polymers and polymer blends. *Macromol.* **49**, 972-978 (2016).

21. A. Richter, R. Guico, J. Wang. Calibrating an ellipsometer using x-ray reflectivity. *Rev. Sci. Instrum.* **72,** 3004-3007 (2001).

22. B. Armstrong, Dektak XT: Standard operating procedure. (2014).

23. J. Liu, S. Ju, Y. Ding, R. Yang. Size effect on the thermal conductivity of ultrathin polystyrene films size effect on the thermal conductivity of ultrathin polystyrene films. *Appl. Phys. Lett.* **104**, 153110 (2014).

24. K. Zheng, F. Sun, X. Tian, J. Zhu, Y. Ma, D. Tang, F. Wang. Tuning the interfacial thermal conductance between polystyrene and sapphire by controlling the interfacial adhesion. *ACS Appl. Mater. Interfaces* **7,** 23644–23649 (2015).

25. R.J. Stevens, A.N. Smith, P.M. Norris. Measurement of thermal boundary conductance of a series of metal-dielectric interfaces by the transient thermoreflectance technique. *J. Heat Transfer* **127,** 315–322 (2016).

26. K. Zheng, F. Sun, J. Zhu, Y. Ma, X. Li, D. Tang, F. Wang, X. Wang. Enhancing the thermal conductance of polymer and sapphire interface *via* self-assembled monolayer. *ACS Nano* **10**, 7792-7798 (2016).

27. K. Zheng, J. Zhu, Y.-M. Ma, D. Tang, F. Wang. Interfacial thermal resistance between high-density polyethylene (HDPE) and sapphire. *Chin. Phys. B* **23**, 107307 (2014).

28. J. Choi, M.F. Rubner. Influence of degree of ionization on weak polyelectrolyte multilayer assembly. *Macromol.* **38**, 116-124 (2005).

29. A.F. Xie, S. Granick. Local electrostatics within a polyelectrolyte multilayer with embedded weak polyelectrolyte. *Macromol.* **35**, 1805-1813 (2002).

30. D.W. Gidley, H.-G. Peng, R.S. Vallery. Positron annihilation as a method to characterize porous materials. *Annu. Rev. Mater. Res.* **36,** 49-79 (2006).

31. X. Xie, K. Yang, D. Li, T.-H. Tsai, J. Shin, P.V. Braun, D.G. Cahill. High and low thermal conductivity of amorphous macromolecules. *Phys. Rev. B* **95**, 035406 (2017).

32. W.C. Oliver, G.M. Pharr. An improved technique for determining hardness and elastic modulus. *J. Mater. Res.* **7**, 1564-1583 (1992).

33. S.N. Magonov, V. Elings, M.H. Whangbo, Phase imaging and stiffness in tapping-mode atomic force microscopy. *Surf. Sci.* **375**, 385-391, (1997).

34. J. Pawley. Low voltage scanning electron microscopy. *J. Microscopy* **136**, 45-68 (1984).

35. K. Hiraoka, H. Shin, T. Yokoyama. Density measurements of poly(acrylic acid) sodium salts. *Polym. Bull.* **8**, 303-309 (1982).

36. S.M. Lee, D.G. Cahill. Heat transport in thin dielectric films. *J. Appl. Phys.* **81**, 2590-2595 (1997).

37. D.W. van Krevelen. Properties of polymers: their correlation with chemical structure; their numerical estimation and prediction from additive group contributions. 4th, completely rev. ed. Amsterdam: Elsevier (2009).

38. S.W. Cranford, M.J. Buehler. Variation of weak polyelectrolyte persistence length through an electrostatic contour length. *Macromol.* **45**, 8067-8082 (2012).

39. D. Stigter, K.A. Dill. Theory of radii and second virial coefficients 2. Weakly charged polyelectrolytes. *Macromol.* **28,** 5338-5346 (1995).

40. H. Lee, J.R. Boyce, A. Nese, S. S. Sheiko, K. Matyjaszewski. pH-induced conformational changes of loosely grafted molecular brushes containing poly(acrylic acid) side chains. *Polymer* **49**, 5490–5496 (2008).

41. A.B. Unni, G. Vignaud, J. P. Chapel, J. Giermanska, J. K. Bal, N. Delorme, T. Beuvier, S. Thomas, Y. Grohens, A. Gibaud. Probing the density variation of confined polymer thin films via simple model-independent nanoparticle adsorption. *Macromol.* **50**, 1027−1036 (2017).

42. A. Eisenberg. Glass transitions in ionic polymers. *Macromol.* **4**, 125-128 (1971).

43. A. Eisenberg, H. Matsura, T. Yokoyama. Glass transition in ionic polymers: the acrylates. *J. Polym. Sci.: Part A-2* **9**, 2131-2135 (1971).

44. M. Todica, T. Stefan, S. Simon, I. Balasz, L. Daraban. UV-Vis and XRD investigation of graphite-doped poly(acrylic) acid membranes. *Turk. J. Phys.* **38**, 261 – 267 *(*2014).

45. S. Komaba, N, Yabuuchi, T. Ozeki, Z.-J. Han, K. Shimomura, H. Yui, Y. Katayama, T. Miura. Comparative study of sodium polyacrylate and poly(vinylidene fluoride) as binders for high capacity Si graphite composite negative electrodes in Li-ion batteries. *J. Phys. Chem. C* **116**, 1380–1389 (2012).

46. V.R. Raghavan, H. Martin. Modelling of two-phase thermal conductivity. *Chem. Eng. Process* **34,** 439–446 (1995).

47. T. Brar, P. France, P.G. Smirniotis. Heterogeneous versus homogeneous nucleation and growth of zeolite A. *J. Phys. Chem. B* **105**, 5383-5390 (2001).

48. X. Liu, J.L. Feldman, D.G. Cahill, R.S. Crandall, N. Bernstein, D.M. Photiadis, M.J. Mehl, D.A. Papaconstantopoulos. High thermal conductivity of a hydrogenated amorphous silicon film. *Phys. Rev. Lett.* **102**, 035901 (2009).

49. T. Zhang, T. Luo. Role of chain morphology and stiffness in thermal conductivity of amorphous polymers. *J. Phys. Chem. B* **120**, 803-812 (2016).

50. J. Vogelsang, J. Brazard, T. Adachi, J.C. Bolinger, P.F. Barbara. Watching the annealing process one polymer chain at a time. *Angew. Chem.* **123**, 2305 –2309 (2011).

51. Y.S. Jung, C.A. Ross. Solvent-vapor-induced tunability of self-assembled block copolymer patterns. *Adv. Mater.* **21**, 2540-2545 (2009).

52. H. Ghasemi, T. Nagarajan, X. Huang, J. Loomis, X. Li, J. Tong, J. Wang, G. Chen. High thermal conductivity ultra-high molecular weight polyethylene (UHMWPE) films. *Thermal and Thermomechanical Phenomena in Electronic Systems (ITherm), 2014 IEEE Intersociety Conference on*, Orlando, FL, 235-239 (2014), doi: 10.1109/ITHERM.2014.6892287.

53. V.A. Kargin, S.Y. Mirlina, V.A. Kabanov, G.A. Mikheleva, A study of the structure of isotactic polyacrylic acid and its salts. *Vysokomol. soedin.* **3**, No. 1, 139-143 (1961).

54. M.L. Miller, K. O'Donnell, J. Skogman. Crystalline polyacrylic acid. *J. Colloid Sci.* **17**, 649-659 (1962).

Chapter 4

Tunable Thermal-Sensitive Polymer-Graphene Oxide Composite for Efficient Capture and Release of Viable Circulating Tumor Cells

4.1 Introduction

With over 1600 people dying of cancer in the United States every day,[1] the prevention of the second leading cause of death is a clear area of research interest in the medical community. The spread of tumor cells to distant locations in the body, or metastasis, is the cause of 90% of cancer related deaths,[2] presenting an impetus for the study of those cells most responsible for cancer mortality. Circulating tumor cells (CTCs) are those cells shed from the primary tumor into the blood circulation, potentially en route to forming a secondary tumor, and are present at the incredibly low frequency of on the order of one in one billion normal blood cells in the peripheral blood of cancer patients.[3] CTCs can not only provide biological insight into primary and metastatic tumors but also have the potential to serve as real time biomarkers for making treatment decisions and

monitoring drug efficacy.[4] Indeed, over 270 clinical trials have now been proposed using CTCs as surrogate bio-markers.[5] However, to date, CTCs have not been incorporated into clinical practice for management of patients with cancer. The main challenges to this field include: (i) reaching the sensitivity needed to isolate these extremely rare cells from the sur- rounding blood cells (1 in 1 billion), (ii) minimizing processing to preserve the viability of cells, and (iii) achieving the specificity necessary to acquire pure population to enable meaningful genomic and functional analysis.

Microfluidic technologies have emerged as a solution to isolate live CTCs from small amounts of blood collected from cancer patients. A common separation technique involves immunocapture, the tethering of an antibody against a CTC-specific marker to a surface or structure to bind CTCs but not the normal blood cells. Functionalized microposts have been used in a number of CTC isolation devices.[6-10] Antibody-functionalized silicon microposts for CTC capture were used in the first microfluidic device designed for this purpose, the CTC Chip.[6] Subsequent microfluidic CTC capture devices also featured micro-features coated with antibodies, such as the geometrically enhanced differential immunocapture (GEDI) chip,[7] chaotic micromixer HB CTC Chip,[11] high throughput micro- sampling unit (HTMSU),[12] and the HD-CTC module of an integrated system.[13] These immunocapture devices included features fabricated from polymers such as polydimethylsiloxane (PDMS), poly(methyl methacrylate) (PMMA), and cyclic olefin copolymer (COC). In order to push the field to realize the opportunities afforded by these cells, which may be captured at early stage as well as mid-metastasis, orthogonal techniques and materials would be necessary to enhance the sensitivity. Nanomaterials provide one such avenue, with advantageous properties such as a high surface area to

volume ratio and a length scale on the order of magnitude of extracellular features. Many different classes of nanomaterials have been incorporated into CTC research.[8,14] One example, graphene oxide (GO) has a number of proven biomedical applications.[15-17] A recently developed GO based device, the GO Chip, took advantage of the increased surface area afforded by graphene oxide for highly sensitive and selective cell capture.[18] CTCs were captured from peripheral blood samples from pancreatic, breast, and early stage lung cancer patients with low white blood cell contamination. However, this device shares the common draw-back across most immunoaffinity based technologies reliant on antibodies attached to a surface: the limitation of post-capture analysis because of the difficulty in releasing viable cells from the capture substrate.

Thermoresponsive polymers, a class of stimuli-responsive polymers that respond to temperature changes by undergoing conformational changes, have found wide applications in drug delivery,[19] tissue engineering,[20] controlling cell adhesion[21] and bacterial growth,[22] protein encapsulation,[23] and the release of captured CTCs from the surface of such capturing devices.[24,25] Alternative CTC release techniques take advantage of alginate hydrogel[26,27] or layer-by-layer assembled[28] degradable capture substrates. However, these approaches all feature performance limitations in throughput,[27] purity requiring additional processing,[29] ability to process blood collected by standard conditions,[26] immense fabrication facility requirements,[24,29] time-consuming chemistry,[25] and inconvenient experimental temperature conditions.[25]

Graphene- and GO-based polymer composites are a new class of materials which combine the excellent properties of graphene, such as high surface-to-volume ratio, high Young's modulus, and high thermal and electrical characteristics,[30] with the easy

123

processability of polymers. Such composites have found uses in fields ranging from energy storage[31] and electronic devices,[32,33] to biomedical applications such as drug and gene delivery,[34,35] cancer therapy,[36] cell differentiation,[37,38] coating of biomedical implants,[39,40] and bio-imaging.[35]

We hypothesized that the combined advantages of a biocompatible functionalized nanomaterial with a thermoresponsive polymer that promotes effective cell release could address the challenge of sensitive capture while simultaneously allowing viable cell release. This could lead to improvement in downstream analysis such as fluorescence in situ hybridization (FISH), molecular analysis, and single cell analysis. We present a new tunable thermal-sensitive polymer–GO Chip for highly efficient capture and subsequent release of CTCs incorporated into a microfluidic device (Figure 1a).

In the current work, the microfluidic device bottom substrate was coated with a composite film of functionalized GO dispersed in a matrix of thermoresponsive polymer with a lower critical solution temperature (LCST) of 13°C. Surface available functionalized GO (described below) provided anchors for attaching the CTC capture antibody while the polymer matrix provided temperature dependent modulation of capture or release functionality. The microfluidic assembly facilitated the processing of patient blood samples within a simple planar device (Figure 1b). Drop-casting the polymer–GO blend on a patterned and surface modified substrate made such a device cheap and easy to fabricate. Moreover, the LCST of around 13°C for the polymer matrix made it possible to use the device at room temperature as opposed to higher temperatures,[29] such that there are no concerns about inadvertently releasing the cells during the capture step. Additionally, cell release occurred under gentle conditions, maximizing the viability of

124

released cells. The consolidation of the advantageous properties of GO-based capture with superior release functionality of the chosen polymer yielded a device that enables the study of these clinically interesting cells without many of the shortcomings of past technologies, while simultaneously presenting an easy, scalable fabrication method.
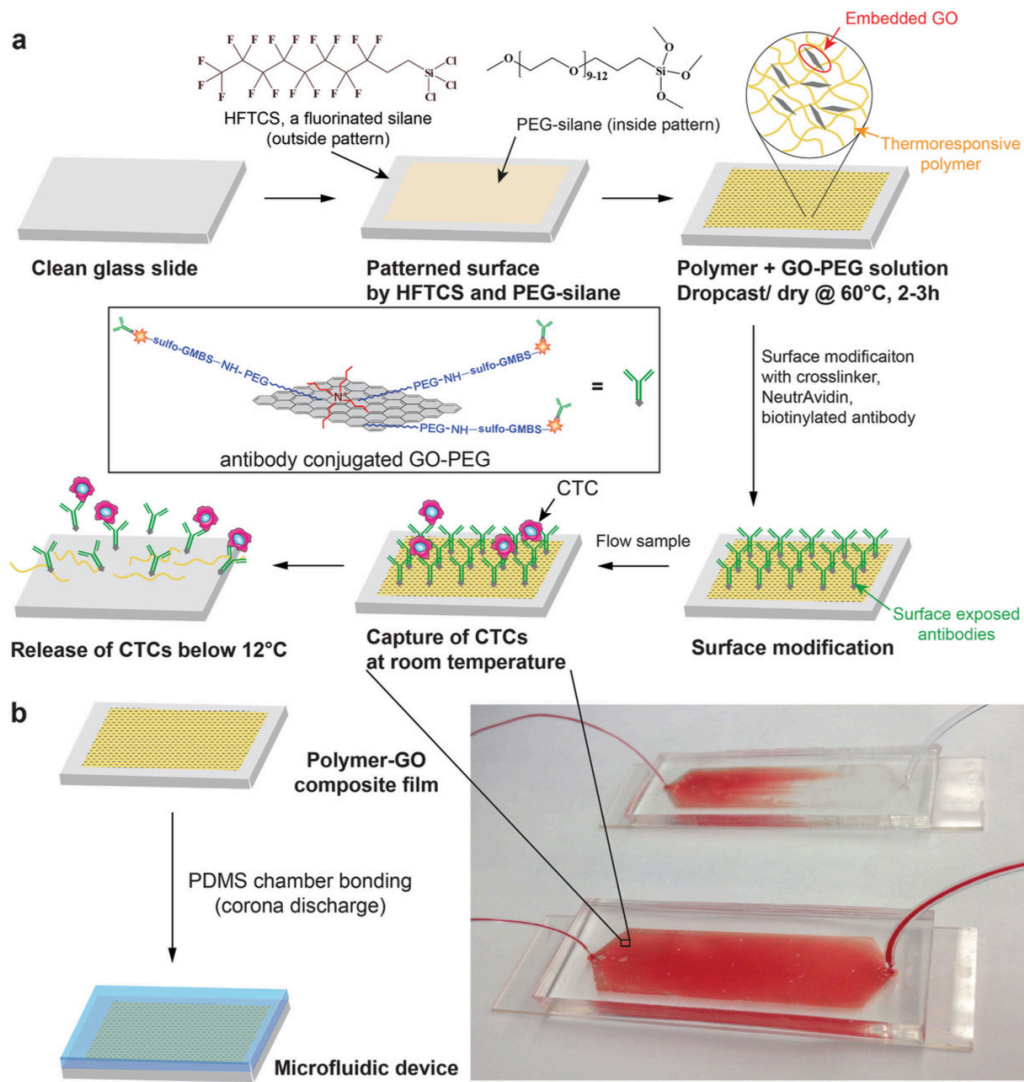
Figure 4.1 | Polymer-GO microfluidic device. a, Schematic concept of a polymer–GO microfluidic device for the capture/release of CTCs. **b,** Enclosure within polydimethylsiloxane chamber and photograph of patient blood samples being processed by the polymer–GO devices.

4.2 Experimental Section

4.2.1 Chemicals and Materials

Acryloyl chloride was procured from Fluka. Piperidine, triethylamine, and basic alumina were purchased from Aldrich used without further purification. azobisisobutyronitrile (AIBN) was purchased from Aldrich, and was recrystallized from methanol before use. Anisole (Aldrich) used was anhydrous grade (99.7%). *N,N*-diethyl acrylamide was procured from TCI America. Dichloromethane, hexanes, and ethyl acetate used were solvent grade and were used without purification.

Kapton polyimide tape was purchased from Cole Parmer. Ethanol, acetone, chloroform, and isopropanol were solvent grade and were used without further purification. Surface modifying agents – (Heptadecafluoro-1,1,2,2-tetrahydrodecyl) trichlorosilane (HFTCS) and 2-methoxy(polyethyleneoxy) propyltrimethoxysilane (PEG-silane) – were purchased from Gelest, Inc. Microscope glass slides were purchased from Fisher. An amine reactive dye, (5-(and-6)-carboxyfluorescein, succinimidyl ester (FSE, C1311) was purchased from Life Technologies.

Single layer GO powder prepared by modified Hummer's method was procured from Cheap Tubes, Inc. Tetrabutylammonium hydroxide (TBA) was purchased from Aldrich. Phospholipid-polyethylene-glyco-amine (PL-PEG-NH$_2$) was obtained from NOF Co. Biotin, 5-fluorescein conjugate was procured from Sigma Aldrich. CellTracker™ Green CMFDA Dye was purchased from Life Technologies / Thermo Fisher Scientific. Histogel for preparing cell blocks was purchased from Thermo Fisher. *N*-γ-maleimidobutyryloxysulfosuccinimide ester (sulfo-GMBS) was procured from Thermo Fisher.

4.2.2 Polymer Synthesis

N-acryloyl piperidine (AP) was synthesized via reaction between acryloyl chloride and piperidine.[41] In short, 0.11 mole of piperidine and 0.12 mole of triethylamine were dissolved in 100 mL of dichloromethane maintained at 0-5°C. A solution of acryloyl chloride (0.10 mole) in 15 mL of dichloromethane was added drop-wise to the above solution over 2 hours under constant stirring. After complete addition, the reaction mixture was stirred at room temperature for 24 hours and was extracted with water and purified by column chromatography (hexane: ethyl acetate, 1:1) to yield colorless to light yellow liquid. *N*,*N*-diethyl acrylamide (DEA) was passed through a basic alumina column prior to polymerization. AIBN was recrystallized from methanol before use. In a typical polymerization reaction, the two monomers, AP and DEA, were dissolved in anisole in 7:3 molar ratio, and 0.3 mole% (of total monomer content) of AIBN was added to the solution. The reaction flask was completely sealed and the solution was purged with Argon for 20 minutes. The reaction was carried out at 65°C for 20 hours. After the reaction, all the solvent was evaporated at high temperature under vacuum to obtain white solid residue. The residue was re-dissolved in chloroform and then twice precipitated in ethyl acetate to obtain white solid mass. The precipitate was recovered and dried at 60°C under vacuum for 2-3 days (Figure 4.2).
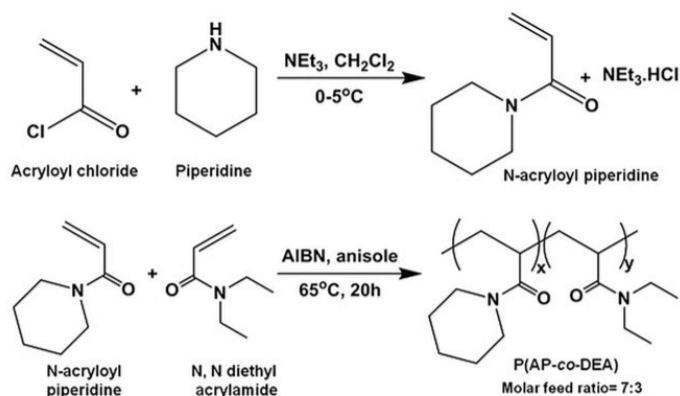
Figure 4.2 | Synthetic scheme for thermo-responsive copolymer, poly(*N*-acryloyl piperidine-*co-N,N*-diethyl acrylamide).

4.2.3 Polymer Characterization

The synthesized polymers were characterized by gel permeation chromatography (GPC, Waters Inc., 1515 Isocratic HPLC pump and 2414 RI detector) using 3 Styragel columns – HR2, HR3 and HR4 – in series maintained at 35°C with chloroform as eluent (flow rate: 1 mLmin^{-1}, total elution time: 40 minutes). The instrument was calibrated with polystyrene standards. LCST was ascertained by measuring UV-vis transmittance (Varian Cary 50 Bio) of a 0.1 wt.% aqueous solution of polymers as a function of temperature. A thermocouple was used for real-time measurement of temperature, with the metal junction dipped in the cuvette during the measurement. For effective measurement, the polymer solution was cooled down to 2-3°C along with the metal cuvette holder to slow down the heating up of sample in ambient condition. CaCl$_2$ was placed inside the UV-vis spectrophotometer chamber to ensure humidity-free environment. This was necessary to prevent atmospheric water vapor from condensing on the cold cuvette walls. UV-vis spectrum was measured from 200-800 nm at every 0.2-0.5°C step with more frequent measurements near the transition temperature.

Transmittance at 400 nm was plotted against temperature; and, the temperature for 50% transmittance was noted as the LCST.

4.2.4 Polymer-Graphene Oxide Nanocomposite: Fabrication and Characterization

GO nanosheets were functionalized with PL-PEG-NH$_2$ according to an earlier reported method to yield GO nanosheets with amine functional group (GO-PEG) (Figure 4.3).[18] The polymer-GO nanocomposite films were prepared through drop-casting a DMF solution of polymer and GO-PEG. The drop-cast films were dried at 60°C in oven for 2-3 h to yield 3–4 μm thick composite film.
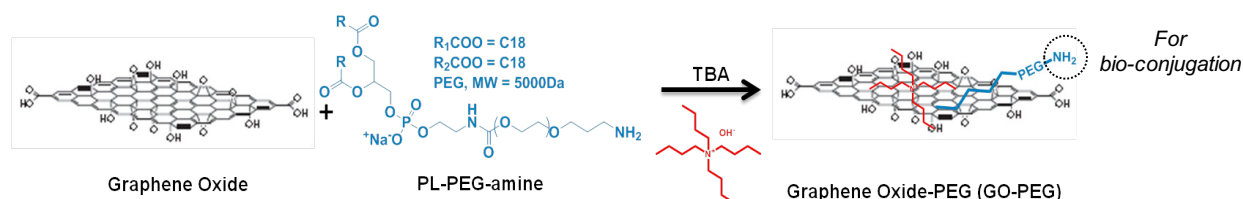
Figure 4.3 | Schematic showing functionalization of graphene oxide (GO) nanosheets to yield functionalized GO-PEG with amine groups for subsequent bio-conjugation.

To show the surface availability of the amine groups from the GO-PEG in polymer-GO composite films, the drop-cast films were incubated with 0.25×10^{-3} M aqueous solution of an amine reactive dye, FSE, for 30 minutes at 40°C and then washed with copious amount of DI water. The dye treated films were then imaged with a fluorescence microscope (Olympus BX51 coupled with Olympus DP71 camera and EXFO X-cite Series 120 light source). To determine the time dependence of dissolution of polymer-GO composite films in cold water, FSE dye-treated films were dipped in cold water for different lengths of time and the fluorescence images before and after dipping were compared.

Films were dipped in cold water (5°C) for 5, 10, 20, and 30 minutes, and in room temperature water (20°C) for 30 minutes. The beakers with the dipped films were kept on an orbital shaker to weakly simulate conditions in microfluidic devices where the films are subjected to shearing by the flowing fluids.

4.2.5 Device Fabrication

The glass slides were sequentially washed with chloroform, acetone, and isopropanol via sonication for 5 minutes each, air dried and treated in a UV-ozone generator for 30 minutes to remove any carbon contamination and to obtain a high density of surface hydroxyl groups. The cleaned substrates were patterned using Kapton tape by masking the active device area. Kapton tape was chosen for its impermeability to silane vapors and good stability at high temperatures. The patterned substrates were then cleaned with wipes dipped in ethanol to remove any adhesive residue and treated with HFTCS via vapor phase surface modification at 100°C for 30 minutes. HFTCS treatment results in hydrophobic fluoroalkyl groups on the unmasked peripheral regions of the substrates which prevent the use of any physical confining barrier to pattern the device with polymer-GO film by drop-casting method. After HFTCS treatment, the Kapton tape mask was removed and the glass slides were washed with copious amounts of ethanol to remove any physisorbed silane as well as any adhesive residue. The second surface modification was done in liquid phase by immersing the glass slides in 3.35 mM of PEG-silane in ethanol for 12-15 hours. Poly(ethylene glycol) (PEG) is well known to render surfaces non-fouling.[42] The PEG monolayer was necessitated to avoid recapturing of the released CTCs on the glass substrate. Subsequently, the glass slides were again washed

with ethanol to remove any physisorbed silane. A polymer-GO blend solution containing 10 mgmL^{-1} of polymer in 975 μL DMF and 25 μL of GO-PEG solution was then drop-cast in requisite amount on the surface modified glass substrates and allowed to dry at 60°C in an oven. The PDMS chamber was assembled on the glass substrate with polymer-GO composite film through corona discharge to produce a microfluidic device (Figure 4.4).
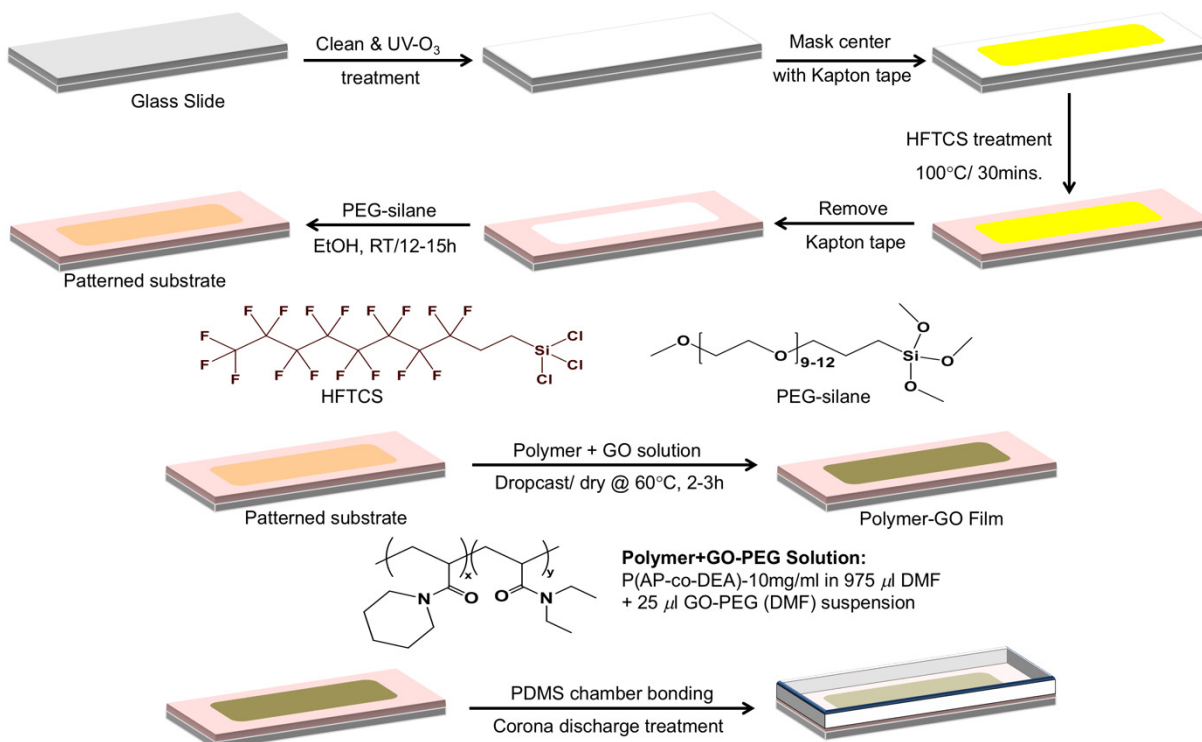
Figure 4.4 | Schematic showing the fabrication steps for the microfluidic device.

The assembled microfluidic device was functionalized by immobilizing anti-EpCAM on the surface available GO through a cross-linker GMBS and avidin–biotin mediated bio-conjugation, providing cell capture/release functionality (Figure 4.5).

4.2.6 Cell Capture/Release Experiments

Cells were stained with CellTracker[TM] Green CMFDA dye according to the manufacturer's protocol. The staining process takes approximately two hours and was performed in parallel with device preparation. Fluorescence-labeled cells of different cell lines were spiked in buffer or blood and flowed through the microfluidic device to establish the device performance parameters.
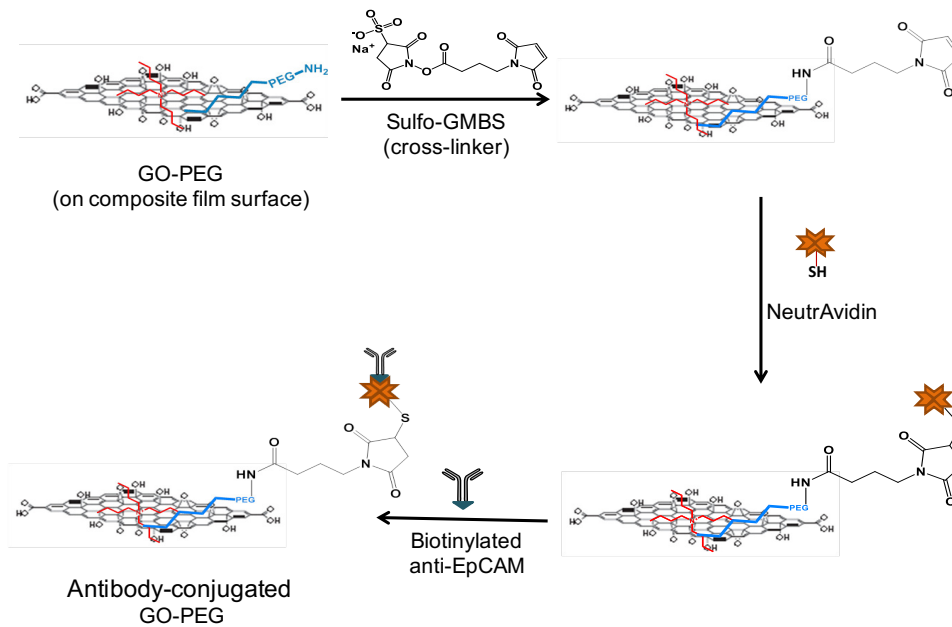
Figure 4.5 | Schematic showing the bio-conjugation chemistry for immobilizing the antibody, anti-EpCAM, on the polymer-GO composite film surface.

4.2.7 Clinical Samples

Blood samples from cancer patients were collected into EDTA tubes and were processed at a flow rate of 1 mL h^{-1}. Following a washing step, cells were released from the chip and deposited/spun onto glass slides by a cytospin centrifuge. CTCs in these samples were identified by using standard immunostaining protocols. For cytopathological studies, CTCs released from the chip were subsequently made into "cell

blocks" by first fixing them with ethanol and then embedding them in Histogel. Blocks were then formalin fixed and stored in 70% ethanol until slide preparation. Blocks were paraffin embedded and sectioned at the University of Michigan Histology Core, and used for fluorescence in-situ hybridization (FISH) studies. FISH hybridization and image capture were performed essentially as previously described.[43]

4.3 Results and Discussion

To create a tunable thermal responsive polymer, copolymer poly(*N*-acryloyl piperidine-*co-N,N*-diethyl acrylamide) was synthesized via free radical polymerization using AIBN as an initiator and was characterized for its molecular weight and LCST (Table 4.1). LCST was modulated by employing a copolymerization technique using two acrylamide monomers with different degrees of hydrophobicity: *N*-acryloyl piperidine (AP) and *N,N*-diethyl acrylamide (DEA). The homopolymers
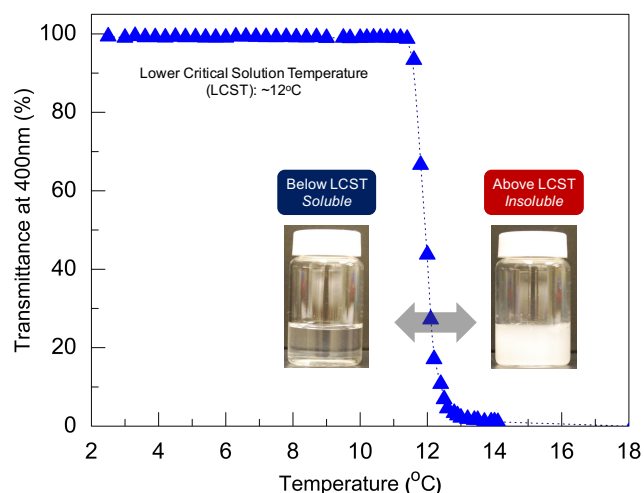
Figure 4.6 | UV–vis transmittance versus temperature plots for the copolymer showing LCST of ≈12°C.

poly(*N*-acryloyl piperidine) (PAP) and poly(*N,N*-diethyl acrylamide) (PDEA) have LCSTs of 4°C and 25°C respectively.[44]   The required capture/release modulation temperature for the CTC device can be achieved by changing the ratio of the two monomers in the copolymer. For example, a copolymer synthesized with 7:3 molar ratio of AP:DEA showed a critical temperature of around 12–13 °C, which was used in this study (Figure 4.6).

Table 4.1 Molecular weights (MW), PDI, and LCST of different batches of synthesized copolymer used in the study

Polymer	MW (M_n, kDa)	PDI	LCST (°C)
P1	209.246	1.47	13.6
P2	151.332	1.67	12.7
P3	175.085	1.46	12.0
P4	173.019	1.75	11.8

Figure 4.7a shows the SEM image of polymer-GO composite film prepared by drop-casting; graphene flakes can be seen suspended on the surface of the film. The polymer-GO composite films should fulfill two conditions for use in the microfluidic device. One, it should have high surface density of amine groups for tethering the antibody against CTC markers, and two, it should allow time-bound dissolution to assist cell release. Surface density of the amine groups was determined by measuring the fluorescence of covalently tethered amine-reactive FSE dye molecules. While polymer-GO composite films showed bright green fluorescence from the surface tethered dye, polymer-only films showed very low to no fluorescence. Though the possibility of physically adsorbed dye molecules cannot be completely ruled out, it is most likely that the dye molecules were primarily tethered to the surface through covalent bonding between the amine groups on film surface and succinimidyl ester groups on the dye, as suggested by large contrast in fluorescence intensity from polymer-GO and polymer-only films (Figure 4.7b). Figure 4.7c shows the fluorescent images of the films before and after dipping in water at 5°C for different durations of time. While the film was completely dissolved and washed off in 20-30 minutes under cold condition as evident from the gradual disappearance of green fluorescence, it remains stable and intact at room

temperature even after 30 minutes. It is to be noted that in the actual device, the

dissolution time is much shorter (~10 minutes), most likely due to the shear of the flowing

buffer.
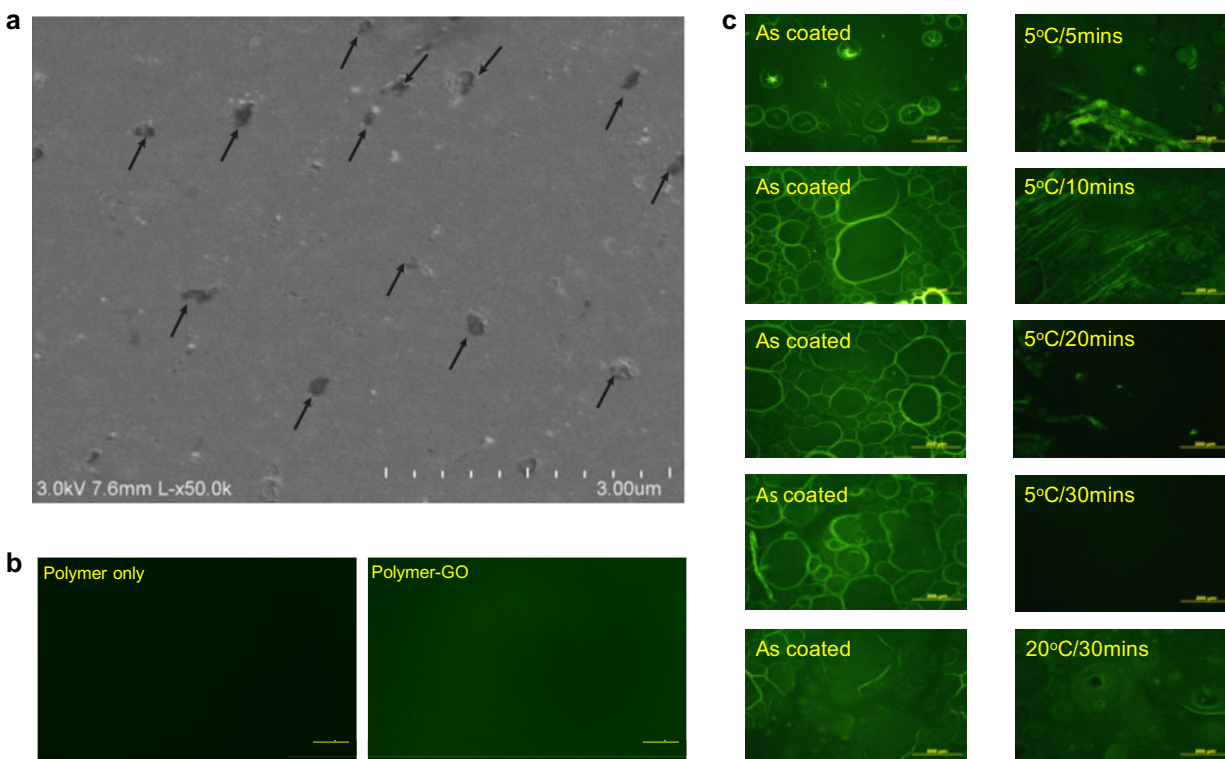
Figure 4.7 | Characterization of polymer-GO composite film. a, SEM image of polymer–GO composite surface. Arrows indicate suspended GO present on the surface of the film. **b,** Fluorescence images of polymer-only and polymer-GO films. The films were incubated with an amine-reactive dye (FSE, 0.25 x 10^{-3} M aq. solution) for 30 minutes at 40 °C. Scale bar: 20 μm. **c,** Fluorescence microscopy images of polymer-GO films incubated with FSE dye before and after being dipped in either cold (5°C) or room temperature (20°C) water for the specified time durations. Scale bar: 200 μm.

To verify the ability to immobilize biotinylated antibody to the polymer-GO film

surface, surface coverage by a fluorescently-labeled biotin was assessed (Figure 4.8a).

Three polymer-GO films underwent the entirety of the conjugation chemistry (i.e.

treatment with the GMBS cross-linker and NeutrAvidin; termed "Condition") with fluorescent biotin addition as the terminal step. To account for non-specific binding, three polymer-GO films were treated only with the fluorescent biotin to serve as a control in an analogous fashion to an isotype control (termed "Control"). ImageJ was used to quantify the fluorescence. This technique showed a statistically significant increase in fluorescence intensity relative to the control (Figure 4.8b). The results discussed above demonstrate that the fabricated polymer-GO composite film serves as an effective platform for antibody immobilization as well as provides effective release mechanism which can be employed for cell isolation.
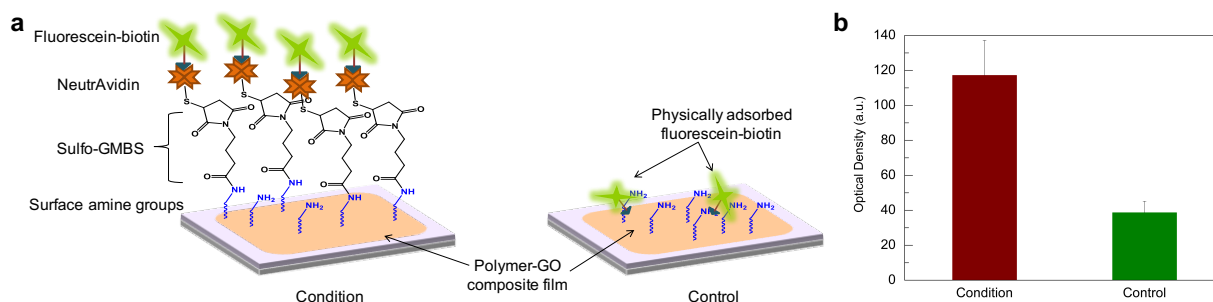
Figure 4.8 | Verification of antibody immobilization on polymer-GO composite film surface. a, Schematic represents fluorescent biotin assay and negative control. **b,** The full conjugation chemistry features statistically higher fluorescence than the negative control as assessed via optical density (p = 0.019).

To further verify the steps of the conjugation chemistry, experiments were performed to compare capture by (1) a polymer film lacking GO alone; (2) a polymer film lacking GO with the addition of anti-EpCAM; and (3) the polymer–GO film with full conjugation chemistry. The two control films showed significantly lower levels of capture with the polymer film and the polymer film with antibody capturing at 6.4% and 11.0% the level of the full chemistry, respectively (Figure 4.9a). Slightly higher capture in case of the

polymer with antibody condition is likely a result of physically adsorbed anti-EpCAM. This also suggests that very little of the capture antibody on the fully functional device is non-specifically bound.

To test the performance of the GO-polymer device for CTC capture, fluorescence-labeled human breast cancer cell lines MCF-7 cells (1000 cells mL^{-1}) were spiked into buffer and flowed through the GO-polymer device at different flow rates (1–10 mLh^{-1}). The captured cells in the device and the non-captured cells collected in the waste were then counted. As expected, the capture efficiency decreased with flow rate. We observed that the efficiency rapidly decreased at flow rates ≥ 5 mLh^{-1}. In the 1–3 mLh^{-1} range, the average capture efficiency was over 88.2% (n = 6 at each flow rate) (Figure 4.9b) with the highest capture of 95.21% at 1 mLh^{-1}. To further investigate the effect of tumor type and EpCAM expression on capture efficiency, three high EpCAM expressing cell lines for various cancer types (MCF-7 breast cancer cells, LNCaP prostate cancer cells, and H1650 lung cancer cells), one low EpCAM expressing cancer-cell line (Panc-1 pancreatic cancer cells), and one EpCAM negative cancer cell lines (Hs578T breast cancer cells) were selected for capture experiments at the flow rate of 1 mLh^{-1}. The cells were fluorescently labeled and spiked into buffer at a concentration of 1000 cells mL^{-1}. The results in Figure 4.9c indicate that the anti-EpCAM-coated GO-polymer device achieved high capture efficiency (84.93–95.21%) for EpCAM-positive cancer cells. In contrast, a relatively low number of EpCAM-negative cells (Hs578T) were captured. Furthermore, the device is comparably effective in capturing different tumor cells, indicating the robust sensitivity of the device. After capturing cells on the devices, cell release experiments were carried out by flowing 1 mL PBS through the devices in a room maintained at 5°C

at 100 μLmin^{-1} (Figure 4.9e). Quantification of the cells in the devices before and after release showed an average cell release of 95.21% and 91.56% in buffer and blood experiments, respectively (Figure 4.9d). Furthermore, we tested the viability of the released cells by live dead assay. 91.68% of cells remained viable after release.
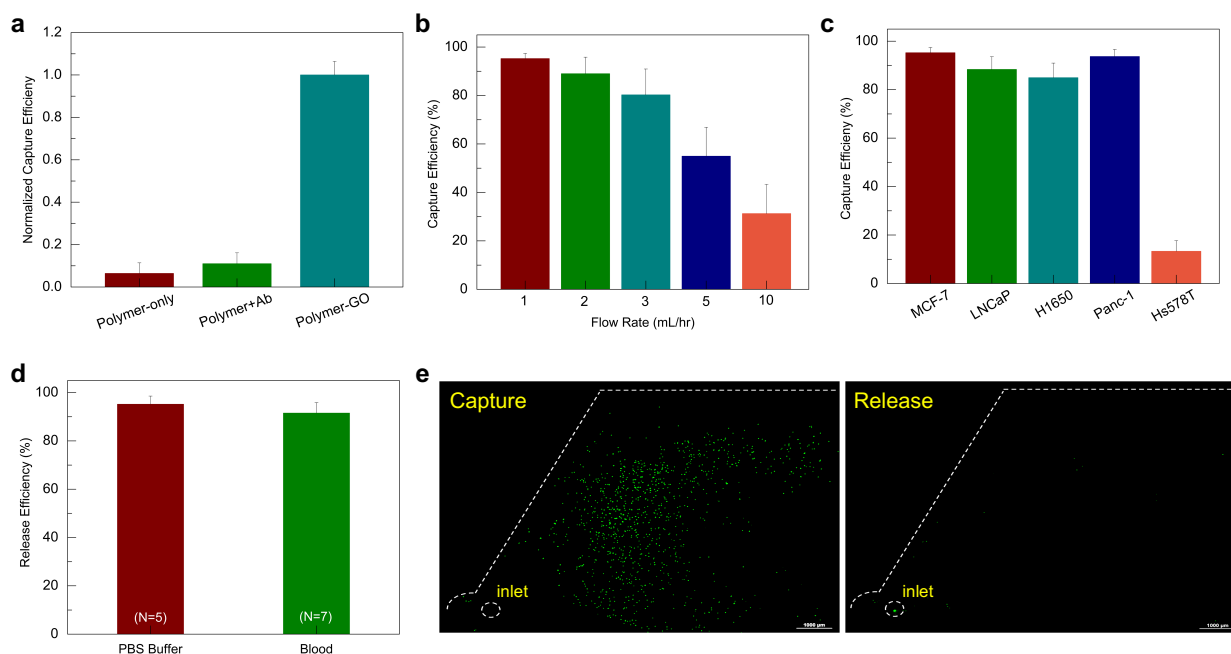
Figure 4.9 | Performance parameters of polymer-GO microfluidic device. a, Capture efficiency of microfluidic devices featuring only the thermosensitive polymer, the thermo-sensitive polymer and non-specifically bound anti-EpCAM, and the polymer-GO film with specific conjugation chemistry as normalized by this last condition. **b,** Cell capture efficiency of the microfluidic polymer-GO device at various flow rates evaluated using a breast cancer cell line (MCF-7). Error bars show standard deviations (n = 6). **c,** Capture efficiency of cell lines of varying origin and EpCAM expression levels. MCF-7 (n = 8), PANC1, H1650, LNCaP, Hs578T (n = 6). **d,** Release efficiency of the microfluidic polymer–GO device (MCF-7 cells were spiked into 1 mL of buffer or blood). **e,** Fluorescence microscope images of devices after capture and release of fluorescently labeled MCF-7 cells. Scale bar: 1000 μm.

To demonstrate the CTC capture and release in clinical samples using the tunable polymer-GO composite film based device, we processed blood samples obtained from

10 metastatic breast cancer patients and 3 pancreatic cancer patients. Post-release, CTCs in these samples were identified as DAPI-positive (shown in blue) nucleated cells staining positive for tumor markers (cytokeratin 7/8, visualized with a secondary antibody tagged with Alexa Fluor 546, shown in red) and negative for leukocyte markers (CD45, visualized with a secondary antibody tagged with Alexa Fluor 488, shown in green) (Figure 4.10a). CTCs were successfully recovered from 8 breast cancer patient samples and 2 pancreatic cancer patients (ranging from 2 to 20 CTCs mL^{-1}) (Figure 4.10b). The average number of CTCs recovered from breast samples was 5.6 CTCs mL^{-1} and from pancreatic samples was 8.3 CTCs mL^{-1}.
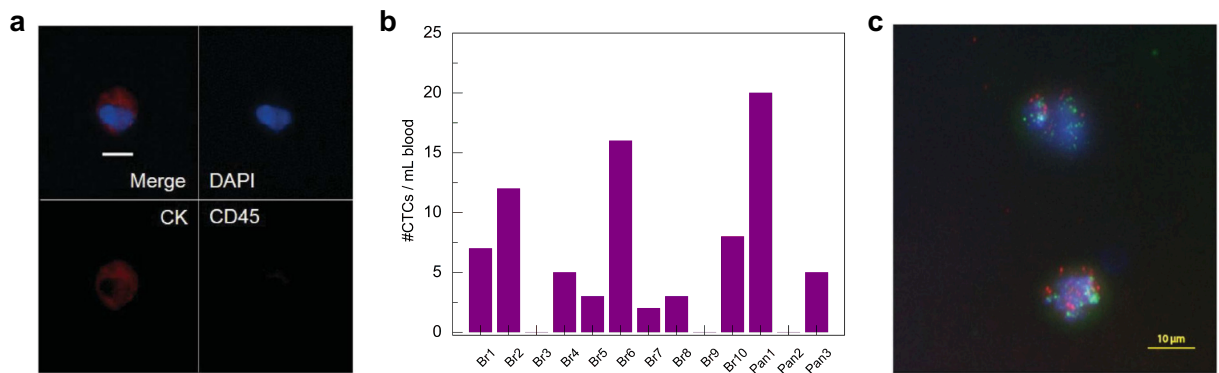
Figure 4.10 | Clinical samples: enumeration and cytopathological study. a, Fluorescence images of CTCs from breast cancer patient sample. Nucleated cells (blue) staining positive for cytokeratin 7/8 (CK, red) and negative for the white blood cell marker CD45 (green) were enumerated as CTCs. Scale bar = 10 μm. **b,** CTC enumeration results from 10 breast cancer patients and 3 pancreatic cancer patients. **c,** FISH image of CTCs of breast cancer patient sample Br10. HER2(green)/centromere 17 probe(red).

Released CTCs were viable and structurally intact, and hence could be readily investigated via standard clinical cytopathological and genetic testing. Here we examined the feasibility of detecting HER2 amplification by FISH. FISH was conducted using probes

for HER2 (BAC clone RP11-94L15) and chromosome 17 control probe (BAC clone RP11-100E5), revealing HER2 amplification in one breast cancer patient (Figure 4.10c). One green signal indicates the presence of one copy of HER2, while one red signal indicates one copy of centromere 17 probe; the multiple green signals in the figure imply HER2 amplification.

4.4 Conclusions

To summarize, a microfluidic device with planar architecture was successfully fabricated. Through the incorporation of a composite that combines the advantages of a temperature-sensitive modality and sensitive nanomaterial-enabled capture, the polymer-GO film that serves as the basis of this technology overcomes some of the key shortcomings of previous CTC capture technologies. As evidenced by data obtained from physiologic solutions containing spiked labelled cancer cells from multiple cancers and the processing of primary breast and pancreatic cancer patient blood samples, isolation of these rare cells with this device is highly feasible, completing the first step to unlocking the research opportunities presented by CTCs. The downstream analysis facilitated by the efficient release of captured cells highlights the potential for this device's use in basic and clinical cancer investigation.

4.5 Author Contributions

Hyeun Joong Yoon*, Apoorv Shanker*, Yang Wang, Molly Kozminsky, Qu Jin, Nallasivam Palanisamy, Monika L. Burness, Ebrahim Azizi, Diane M. Simeone, Max S. Wicha, Jinsang Kim, Sunitha Nagrath. Tunable Thermal-Sensitive Polymer-Graphene

Oxide Composite for Efficient Capture and Release of Viable Circulating Tumor Cells. *Advanced Materials* **28**, 4891-4897 (2016) *(*equal contribution)*

A.S. conceived the initial ideas of developing thermo-responsive nanocomposites with the help of J.K., and designed, developed and characterized the polymer and polymer-GO nanocomposite films. A.S. developed the fabrication procedure for the microfluidic devices and assisted H.J.Y. in cell line experiments for device optimization. H.J.Y. prepared the functionalized graphene oxide, PDMS chambers and carried out most of the cell experiments as well as clinical sample processing with help from Y.W. and M.K. Q.J. assisted H.J.Y. in cell experiments and enumeration. N.P., M.L.B., E.A., D.M.S. and M.S.W. either carried out, assisted or supervised cytopathological tests. J.K. and S.N. supervised the project. H.J.Y. and S.N. wrote the manuscript with contributions from A.S.

4.6 References

1. U.S. Cancer Statistics Working Group. United States Cancer Statistics: 1999–2013 Incidence and Mortality Web-based Report. Atlanta: U.S. Department of Health and Human Services, Centers for Disease Control and Prevention and National Cancer Institute; 2016. Available at: www.cdc.gov/uscs (Accessed: 7th April 2017)

2. G. P. Gupta, J. Massagué. Cancer metastasis: building a framework. *Cell* **127**, 679-695 (2006).

3. S. Maheswaran, D. A. Haber. Circulating tumor cells: a window into cancer biology and metastasis. *Curr. Opinion Genet. Dev.* **20,** 96-99 (2010).

4. P. Paterlini-Brechot, N. L. Benali. Circulating tumor cells (CTC) detection: clinical impact and future directions. *Cancer Lett.* **253**, 180-204 (2007).

5. C. Alix-Panabieres, K. Pantel. Challenges in circulating tumour cell research. *Nature Rev. Cancer* 14, 623-631 (2014).

6. S. Nagrath, L. V. Sequist, S. Maheswaran, D. W. Bell, D. Irimia, L. Ulkus, M. R. Smith, E. L. Kwak, S. Digumarthy, A. Muzikansky, P. Ryan, U. J. Balis, R. G. Tompkins, D. A. Haber, M. Toner. Isolation of rare circulating tumour cells in cancer patients by microchip technology. *Nature* **450**, 1235-1239 (2007).

7. J. P. Gleghorn, E. D. Pratt, D. Denning, H. Liu, N. H. Bander, S. T. Tagawa, D. M. Nanus, P. A. Giannakakou, B. J. Kirby. Capture of circulating tumor cells from whole blood of prostate cancer patients using geometrically enhanced differential immunocapture (GEDI) and a prostate-specific antibody. *Lab Chip* **10**, 27-29 (2010).

8. H. J. Yoon, M. Kozminsky, S. Nagrath. Emerging role of nanomaterials in circulating tumor cell isolation and analysis. *ACS Nano* **8**, 1995-2017 (2014).

9. Z. Zhang, S. Nagrath. Microfluidics and cancer: are we there yet? *Biomed. Microdev.* **15**, 595-609 (2013).

10. Z. Zhang, H. Shiratsuchi, J. Lin, G. Chen, R. M. Reddy, E. Azizi, S. Fouladdel, A. C. Chang, L. Lin, H. Jiang, M. Waghray, G. Luker, D. M. Simeone, M. S. Wicha, D. G. Beer, N. Ramnath, S. Nagrath. Expansion of CTCs from early stage lung cancer patients using a microfluidic co-culture model. *Oncotarget* **5**, 12383-12397 (2014).

11. S. L. Stott, C. Hsu, D. I. Tsukrov, M. Yu, D. T. Miyamoto, B. A. Waltman, S. M. Rothenberg, A. M. Shah, M. E. Smas, G. K. Korir, F. P. Floyd, A. J. Gilman, J. B. W. D. Lord, S. Springer, D. Irimia, S. Nagrath, L. V. Sequist, R. J. Lee, K. J. Isselbacher, S. Maheswaran, D. A. Haber, M. Toner. Isolation of circulating tumor cells using a microvortex-generating herringbone-chip. *Proc. Natl. Acad. Sci. USA* **107**, 18392-18397 (2010).

12. A. A. Adams, P. I. Okagbare, J. Feng, M. L. Hupert, D. Patterson, J. Göttert, R. L. McCarley, D. Nikitopoulos, M. C. Murphy, S. A. Soper. Highly efficient circulating tumor cell isolation from whole blood and label-free enumeration using polymer-based microfluidics with an integrated conductivity sensor. *J. Am. Chem. Soc.* **130**, 8633-8641 (2008).

13. J. W. Kamande, M. L. Hupert, M. A. Witek, H. Wang, R. J. Torphy, U. Dharmasiri, S. K. Njoroge, J. M. Jackson, R. D. Aufforth, A. Snavely, J. J. Yeh, S. A. Soper. Modular microsystem for the isolation, enumeration, and phenotyping of circulating tumor cells in patients with pancreatic cancer. *Anal. Chem.* **85**, 9092-9100 (2013).

14. L. Wang, W. Asghar, U. Demirci, Y. Wan. Nanostructured substrates for isolation of circulating tumor cells. *Nano Today* **8**, 374-387 (2013).

15. X. Sun, Z. Liu, K. Welsher, J. T. Robinson, A. Goodwin, S. Zaric, H. Dai. Nano-graphene oxide for cellular imaging and drug delivery. *Nano Res.* **1**, 203-212 (2008)

16. J. H. Jung, D. S. Cheon, F. Liu, K. B. Lee, T. S. Seo. A graphene oxide based immuno-biosensor for pathogen detection. *Angew. Chem. Int. Ed.* **49**, 5708-5711 (2010).

17. L. Feng, Y. Chen, J. Ren, X. Qu. A graphene functionalized electrochemical aptasensor for selective label-free detection of cancer cells. *Biomaterials* **32**, 2930-2937 (2011).

18. H. J. Yoon, T. H. Kim, Z. Zhang, E. Azizi, T. M. Pham, C. Paoletti, J. Lin, N. Ramnath, M. S. Wicha, D. F. Hayes, D. M. Simeone, S. Nagrath. Sensitive capture of circulating tumour cells by functionalized graphene oxide nanosheets. *Nature Nanotech.* **8**, 735-741 (2013).

19. K. Nakamura, Y. Maitani, A. M. Lowman, K. Takayama, N. A. Peppas, T. Naga. Uptake and release of budesonide from mucoadhesive, pH-sensitive copolymers and their application to nasal delivery. *J. Controlled Release* **61**, 329-335 (1999).

20. M. Nitschke, S. Gramm, T. Götze, M. Valtink, J. Drichel, B. Voit, K. Engelmann, C. Werner. Thermo-responsive poly(NIPAAM-*co*-DEGMA) substrates for gentle harvest of human corneal endothelial cell sheets. *J. Biomed. Mater. Res. Part A* **80A**, 1003-1010 (2007).

21. R. A. Stile, K. E. Healy. Thermo-responsive peptide-modified hydrogels for tissue regeneration. *Biomacromol.* **2**, 185-194 (2001).

22. D. Cunliffe, C. A. Smart, J. Tsibouklis, S. Young, C. Alexander, E. N. Vulfson. Bacterial adsorption to thermoresponsive polymer surfaces. *Biotechnol. Lett.* **22,** 141-145 (2000).

23. D. L. Huber, R. P. Manginell, M. A. Samara, B.-I. Kim, B. C. Bunker. Programmed adsorption and release of proteins in a microfluidic device. *Science* **301**, 352-354 (2003).

24. S. Hou, H. Zhao, L. Zhao, Q. Shen, K. S. Wei, D. Y. Suh, A. Nakao, M. A. Garcia, M. Song, T. Lee, B. Xiong, S. C. Luo, H. R. Tseng, H. H. Yu. Capture and stimulated release of circulating tumor cells on polymer-grafted silicon nanostructures. *Adv. Mater.* **25**, 1547-1551 (2013).

25. H. Liu, X. Liu, J. Meng, P. Zhang, G. Yang, B. Su, K. Sun, L. Chen, D. Han, S. Wang, L. Jiang. Hydrophobic interaction-mediated capture and release of cancer cells on thermoresponsive nanostructured surfaces. *Adv. Mater.* **25,** 922-927 (2013).

26. A. Hatch, G. Hansmann, S. K. Murthy. Engineered alginate hydrogels for effective microfluidic capture and release of endothelial progenitor cells from whole blood. *Langmuir* **27**, 4257-4264 (2011).

27. A. M. Shah, M. Yu, Z. Nakamura, J. Ciciliano, M. Ulman, K. Kotz, S. L. Stott, S. Maheswaran, D. A. Haber, M. Toner. Biopolymer system for cell recovery from microfluidic cell capture devices. *Anal. Chem.* **84**, 3682−3688 (2012).

28. E. Reategui, N. Aceto, E. J. Lim, J. P. Sullivan, A. E. Jensen, M. Zeinali, J. M. Martel, A. J. Aranyosi, W. Li, S. Castleberry, A. Bardia, L. V. Sequist, D. A. Haber, S. Maheswaran, P. T. Hammond, M. Toner, S. L. Stott. Tunable nanostructured coating for the capture and selective release of viable circulating tumor cells. *Adv. Mater*. **27**, 1593–1599 (2015).

29. Z. Ke, M. Lin, J. F. Chen, J. S. Choi, Y. Zhang, A. Fong, A. J. Liang, S. F. Chen, Q. Li, W. Fang, P. Zhang, M. A. Garcia, T. Lee, M. Song, H. A. Lin, H. Zhao, S. C. Luo, S. Hou, H. H. Yu, H. R. Tseng. Programming thermoresponsiveness of NanoVelcro substrates enables effective purification of circulating tumor cells in lung cancer patients. *ACS Nano* **9**, 62-70 (2015).

30. T. K. Das, S. Prusty. Graphene-based polymer composites and their applications. *Polymer-Plastics Technol. Eng.* **52**, 319-331 (2013).

31. Q. Wu, Y. Xu, Z. Yao, A. Liu, G. Shi. Supercapacitors based on flexible graphene/polyaniline nanofiber composite films. *ACS Nano* **4**, 1963-1970 (2010).

32. X. D. Zhuang, Y. Chen, G. Liu, P. P. Li, C. X. Zhu, E. T. Kang, K. G. Noeh, B. Zhang, J. H. Zhu, Y. X. Li. Conjugated-polymer-functionalized graphene oxide: synthesis and nonvolatile rewritable memory effect. *Adv. Mater.* **22**, 1731-1735 (2010).

33. G. L. Li, G. Liu, M. Li, D. Wan, K. G. Neoh, E. T. Kang. Organo-and water-dispersible graphene oxide-polymer nanosheets for organic electronic memory and gold nanocomposites. *J. Phys. Chem. C* **114**, 12742-12748 (2010).

34. N. G. Sahoo, H. Bao, Y. Pan, M. Pal, M. Kakran, H. K. F. Cheng, L. Li, L. P. Tan. Functionalized carbon nanomaterials as nanocarriers for loading and delivery of a poorly water-soluble anticancer drug: a comparative study. *Chem. Commun.* **47**, 5235-5237 (2011).

35. H. Kim, R. Namgung, K. Singha, I.-K. Oh, W. J. Kim. Graphene oxide-polyethylenimine nanoconstruction as a gene delivery vector and bioimaging tool. *Bioconjug. Chem.* **22**, 2558-2567 (2011).

36. S.-H. Hu, Y.-W. Chen, W.-T. Hung, I. W. Chen, S.-Y. Chen. Quantum-dot-tagged reduced graphene oxide nanocomposites for bright fluorescence bioimaging and photothermal therapy monitored in situ *Adv. Mater.* **24**, 1748-1754 (2012).

37. S. Kumar, S. Raj, E. Kolanthai, A. K. Sood, S. Sampath, K. Chatterjee. Chemical functionalization of graphene to augment stem cell osteogenesis and inhibit biofilm formation on polymer composites for orthopedic applications. *ACS Appl. Mater. Interfaces* **7**, 3237-3252 (2015).

38. B. Chaudhuri, D. Bhadra, L. Moroni, K. Pramanik. Myoblast differentiation of human mesenchymal stem cells on graphene oxide and electrospun graphene oxide-polymer composite fibrous meshes: importance of graphene oxide conductivity and dielectric constant on their biocompatibility. *Biofabrication* **7**, 015009 (2015).

39. S. Thampi, V. Muthuvijayan, R. Parameswaran. Mechanical characterization of high-performance graphene oxide incorporated aligned fibroporous poly(carbonate urethane) membrane for potential biomedical applications. *J. Appl. Polymer Sci.* **132**, 41809 (2015).

40. H. R. Pant, P. Pokharel, M. K. Joshi, S. Adhikari, H. J. Kim, C. H. Park, C. S. Kim. Processing and characterization of electrospun graphene oxide/polyurethane composite nanofibers for stent coating *Chem. Eng. J.* **270**, 336-342 (2015).

41. Y. S. Jo, A. J. van der Vlies, J. Gantz, S. Antonijevic, D. Demurtas, D. Velluto, J. A. Hubbell. RAFT homo- and copolymerization of *N*-acryloyl-morpholine, piperidine, and azocane and their self-assembled structures. *Macromol.* **41**, 1140-1150 (2008).

42. F. Cecchet, B. De Meersman, S. Demoustier-Champagne, B. Nysten, A. M. Jonas. One step growth of protein antifouling surfaces: monolayers of poly(ethylene oxide) (PEO) derivatives on oxidized and hydrogen-passivated silicon surfaces. *Langmuir* **22**, 1173-1181 (2006).

43. S. Ithimakin, K. C. Day, F. Malik, Q. Zen, S. J. Dawsey, T. F. Bersano- Begey, A. A. Quraishi, K. W. Ignatoski, S. Daignault, A. Davis, C. L. Hall, N. Palanisamy, A. N. Heath, N. Tawakkol, T. K. Luther, S. G. Clouthier, W. A. Chadwick, M. L. Day, C. G. Kleer, D. G. Thomas, D. F. Hayes, H. Korkaya, M. S. Wicha. HER2 drives luminal breast cancer stem cells in the absence of HER2 amplification: implications for efficacy of adjuvant trastuzumab. *Cancer Res.* **73**, 1635-1646 (2013).

44. K. Hoshino, M. Taniguchi, T. Kitao, S. Morohashi, T. Sasakura. Preparation of a new thermo-responsive adsorbent with maltose as a ligand and its application to affinity precipitation. *Biotechnol. Bioeng.* **60**, 568-579 (1998).

Chapter 5
Conclusions and Future Outlook

5.1 Research Summary

Rational molecular designing is a powerful tool for development of polymeric materials which enables precise control of their intrinsic properties as well as their interaction with and response to the environment. This dissertation presents molecular design strategies to design and develop polymeric materials for two distinct applications. In Chapters 2 and 3, strategies to modulate polymer chain morphology, inter-chain interactions, and chain packing have been explored to realize enhanced thermal transport properties in amorphous polymers. Chapter 4 presents the application of a unique polymer composite system with tailored response to temperature towards isolation of rare cells from biological fluids.

Contrary to the mechanical, optical and electronic or charge transport properties of polymers, thermal transport properties remain mostly unexplored in terms of chemical structure-property relationship. The most common methods, viz., blending with high-κ fillers[1] and chain orientation,[2,3] to enhance thermal conductivity of polymers usually

involve difficult manufacturing processes, high cost and loss of the advantageous attributes of polymers. Despite their low thermal conductivities, low cost and easy machinability of polymers make them the material of choice even for applications that require rather good heat dissipation. Realizing high thermal conductivities in amorphous polymers is crucially important for many existing applications like LED housings and thermal interface materials in electronic chips as well as for the upcoming field of flexible electronics. Chapter 2 details the design strategies for polymer blends to realize high thermal conductivity in an amorphous system. Through a rationally designed pair of H-bonding polymers, which included one polymer with long flexible chains mixed with another polymer with short and rigid chains, a high concentration of strong and homogeneously distributed H-bonds was achieved. Such a system of H-bonded polymers with closely connected chains created an efficient percolating network of thermal connections resulting in thermal conductivities reaching up to 1.72 $Wm^{-1}K^{-1}$ which is nearly an order of magnitude higher than that of typical amorphous polymers. On the other hand, H-bonded polymer systems with either weak H-bonds or moderately strong H-bonds formed through large linker moieties didn't show any appreciable enhancement in thermal conductivity. We further explored the thermal transport properties of a weak polyelectrolyte in Chapter 3. For a weak polyelectrolyte, controlled ionization was found to engender positive attributes in polymer chains vis-à-vis thermal transport. When ionized, polyelectrolyte chains attained extended morphology due to coulombic repulsion between adjacent like charges making intra-chain heat transfer more feasible. This is similar to high thermal conductivities measured along the direction of chain orientation in mechanically stretched fibers.[2] Better chain packing afforded by the extended chains as

well as stiffening of ionized chains due to the presence of counter-ions further promoted enhanced thermal transport. In a system with predominantly ionized (~90%) chains, thermal conductivity up to 1.17 $Wm^{-1}K^{-1}$ was achieved, which is nearly 3.5 times higher than that of completely unionized polymer. The polyelectrolyte system was found amenable for fabricating micrometer thick amorphous films. Thermal conductivity up to 0.6 $Wm^{-1}K^{-1}$ achieved in such films was 1.5 times higher than that of unstretched semi-crystalline PE films of comparable thickness.[4] Overall, the two strategies presented in this dissertation present a significant breakthrough in molecular engineering of polymers to realize high thermal conductivities in amorphous systems.

The concept of molecular engineering was also extended to designing polymer composites with tailored stimulus-responsive behavior and applied for isolation of circulating tumor cells from blood. In chapter 4, we describe the fabrication of a microfluidic device with a thermo-responsive polymer-graphene oxide (GO) nanocomposite film platform. The consolidation of the advantageous properties of a biocompatible functionalized nanomaterial (GO) with the superior release functionality of the designed thermo-responsive polymer yielded a device that enabled the study of CTCs without many of the shortcomings such as performance limitations in throughput,[5] purity requiring additional processing,[6] ability to process blood collected by standard conditions,[7] immense fabrication facility requirements,[8] time-consuming chemistry,[9] and inconvenient experimental temperature conditions[9] associated with some of the past technologies, while simultaneously presenting an easy, scalable fabrication method. The designed bifunctional polymer-GO film acted as a substrate for tethering antibodies against the cell marker and also provided the release mechanism for flushing out the

captured CTCs from the microfluidic device. At temperatures higher than the lower critical solution temperature (LCST) of the polymer, the polymer-GO nanocomposite film remained intact resulting in capture of CTCs from blood flowing through the device. Post-capture, lowering the temperature below the LCST resulted in deconstruction of the composite film thereby releasing the captured cells. The devices were successfully employed to isolate viable and structurally intact CTCs from clinical samples, thereby underlining their utility in research and clinical settings.

5.2 Future Outlook

The two amorphous polymeric systems with high thermal conductivities presented in this dissertation demonstrate the feasibility of modulating their thermal transport properties through molecular engineering strategies. To aid the development of thermally conductive, a complete understanding of the chemical structure-property relationship will be indispensable. As shown in chapters 2 and 3, thermal transport in polymers is predominantly affected by the chain morphology, which is consistent with the observed extraordinarily high κ in mechanically stretched[2] and aligned polymer nanofibers[3]. While both H-bonding and electrostatically induced chain extension result in enhanced κ, the latter provides a more straightforward mechanism to systematically vary the degree of chain extension and investigate its effects on thermal conductivity. Assisted with a new thermoreflectance-based measurement technique,[10] the effect of three important design parameters that together determine the polymer architecture, viz., tacticity, density of ionizable groups, and connectivity of these groups to the polymer backbone, on thermal conduction can be investigated. Explicitly controlling the ionization of polyelectrolytes can

provide better resolution of the minute differences in measured thermal conductivity. Similarly, developing a comprehensive understanding of thermal transport in cross-linked systems is critically important as these materials find widespread applications. Cross-linking polymer chains using covalent bonds is a compelling strategy to accomplish this coupling as it is widely used in polymer product manufacturing. Therefore, another critical goal of a future study will be to fill the gap in understanding of the effects of bonding nature on thermal transport properties in such cross-linked or H-bonded systems.

The microfluidic device presented in chapter 4 overcame many of the shortcomings of previous technologies. Efficient isolation of viable and structurally intact CTCs afforded by the polymer-GO device allows for the advanced downstream analysis of CTCs which could become a "real-time" indicator for monitoring tumor progression or efficacy of drugs leading to development of personalized therapy. Low cost and ease of fabrication makes it scalable for commercialization. Future study will need to optimize it for large-scale clinical study and investigate its clinical utility for therapeutic marker discovery, treatment selection, and management.

5.3 References

1. H. Chen, V.V. Ginzburg, J. Yang, Y. Yang, W. Liu, Y. Huang, L. Du, B. Chen. Thermal conductivity of polymer-based composites: fundamentals and applications. *Prog. Polym. Sci.* **59**, 41–85 (2016).

2. S. Shen, A. Henry, J. Tong, R.T. Zheng, G. Chen. Polyethylene nanofibres with very high thermal conductivities. *Nature Nanotech.* **5,** 251–255 (2010).

3. V. Singh *et al.* High thermal conductivity of chain-oriented amorphous polythiophene. *Nature Nanotech.* **9,** 384–390 (2014).

4. H. Ghasemi, T. Nagarajan, X. Huang, J. Loomis, X. Li, J. Tong, J. Wang, G. Chen. High thermal conductivity ultra-high molecular weight polyethylene (UHMWPE) films. *Thermal and Thermomechanical Phenomena in Electronic Systems (ITherm), 2014 IEEE Intersociety Conference on*, Orlando, FL, 235-239 (2014), doi: 10.1109/ITHERM.2014.6892287.

5. A. M. Shah, M. Yu, Z. Nakamura, J. Ciciliano, M. Ulman, K. Kotz, S. L. Stott, S. Maheswaran, D. A. Haber, M. Toner. Biopolymer system for cell recovery from microfluidic cell capture devices. *Anal. Chem.* **84**, 3682–3688 (2012).

6. Z. Ke, M. Lin, J. F. Chen, J. S. Choi, Y. Zhang, A. Fong, A. J. Liang, S. F. Chen, Q. Li, W. Fang, P. Zhang, M. A. Garcia, T. Lee, M. Song, H. A. Lin, H. Zhao, S. C. Luo, S. Hou, H. H. Yu, H. R. Tseng. Programming thermoresponsiveness of NanoVelcro substrates enables effective purification of circulating tumor cells in lung cancer patients. *ACS Nano* **9**, 62–70 (2015).

7. A. Hatch, G. Hansmann, S. K. Murthy. Engineered alginate hydrogels for effective microfluidic capture and release of endothelial progenitor cells from whole blood. *Langmuir* **27**, 4257-4264 (2011).

8. S. Hou, H. Zhao, L. Zhao, Q. Shen, K. S. Wei, D. Y. Suh, A. Nakao, M. A. Garcia, M. Song, T. Lee, B. Xiong, S. C. Luo, H. R. Tseng, H. H. Yu. Capture and stimulated release of circulating tumor cells on polymer-grafted silicon nanostructures. *Adv. Mater.* **25**, 1547–1551 (2013).

9. H. Liu, X. Liu, J. Meng, P. Zhang, G. Yang, B. Su, K. Sun, L. Chen, D. Han, S. Wang. Hydrophobic interaction-mediated capture and release of cancer cells on thermoresponsive nanostructured surfaces. *Adv. Mater.* **25**, 922–927 (2013).

10. D. A. Young, C. Thomsen, H. T. Grahn, H. J. Maris, and J. Tauc, in *Phonon scattering in condensed matter*, edited by A. C. Anderson and J. P. Wolfe (Springer, Berlin, 1986), p. 49.